5-1992

An Embedded Ring Approach to the Vibrational Dynamics of Disordered Two-Dimensional Materials

Timothy Edwin Doyle
Utah State University

Recommended Citation

Doyle, Timothy Edwin, "An Embedded Ring Approach to the Vibrational Dynamics of Disordered Two-Dimensional Materials" (1992). *All Graduate Theses and Dissertations*. 2097.
https://digitalcommons.usu.edu/etd/2097

AN EMBEDDED RING APPROACH TO THE VIBRATIONAL DYNAMICS OF DISORDERED TWO-DIMENSIONAL MATERIALS

by

Timothy Edwin Doyle

A thesis submitted in partial fulfillment
of the requirements for the degree

of

MASTER OF SCIENCE

in

Physics

Approved:

Major Professor	Committee Member
Committee Member	Dean of Graduate Studies

UTAH STATE UNIVERSITY
Logan, Utah

1992

ACKNOWLEDGMENTS

I wish to thank Dr. John Robert Dennison for his wisdom and guidance throughout the course of my graduate work. The many helpful suggestions, discussions, and encouragement freely offered by him are deeply appreciated. Dr. Akeley Miller and Dr. Wilford Hansen are gratefully acknowledged for their invaluable help and support, and their role in my thesis work cannot be overstated. Dr. Ed McCullough assisted me in resolving ambiguities encountered in the calculation of the g-matrix elements, and Dr. James Wheeler helped me in working out the relationship between ring geometry and network dimensionality; their efforts are sincerely appreciated. I would also like to thank Bill Helms and Teresa Burns, whose humor and friendship helped me to maintain a healthy perspective throughout graduate school. Finally, I would like to express my deepest gratitude to my wife, Christine, whose love and support have, as always, crystallized dreams and impossibilities into reality.

Timothy Edwin Doyle

TABLE OF CONTENTS

Page

TABLE OF CONTENTS (Continued)

LIST OF TABLES

LIST OF TABLES (Continued)

LIST OF FIGURES

LIST OF FIGURES (Continued)

ABSTRACT

AN EMBEDDED RING APPROACH TO THE VIBRATIONAL DYNAMICS OF DISORDERED TWO-DIMENSIONAL MATERIALS

by

Timothy Edwin Doyle, Master of Science
Utah State University, 1992

Major Professor: Dr. John Robert Dennison
Department: Physics

A theoretical approach was developed to model the vibrational dynamics of amorphous, two-dimensional materials. The materials were modeled as continuous random networks (CRN's) comprising an assemblage of planar rings of diverse size. In-plane vibrational modes for symmetric 4-, 5-, 6-, 7-, and 8-membered rings were examined. Vibrational states of isolated rings were modified by coupling the rings to a continuous network to represent rings embedded in a CRN. An effective force constant was used to couple the ring vibrations to the network's collective motions. Potentials were approximated with the use of a central force model (bond-stretching force constant) and a valence force model (bond-stretching and bond-angle-bending force constants). Valence force model calculations employed group theory. Mode frequencies were calculated using the method of small oscillations and the normal coordinate treatment.

Amorphous carbon was used as a test case for the embedded ring approach. A physically consistent set of force constants for the valence force model was determined by comparing the 6-membered ring E_{2g} mode to the E_{2g} mode in graphite. Frequencies for selected ring modes were calculated, resulting in a discrete line spectrum.

Calculated frequencies were fitted with gaussian peaks and convoluted into theoretical spectra for comparison with the experimental Raman spectrum of amorphous carbon. Integrated gaussian lineshape intensities were assumed to be directly proportional to the CRN ring statistics. The peaks were convoluted with the peak widths, ring statistics, and number of modes as the adjustable parameters.

Parameters consistent with previous research on the structure and dynamics of amorphous carbon provided satisfactory fits to the data. The best fit to the Raman data includes the E_{2g} and A_{1g} modes of 6-membered rings (present in Raman spectra of nanocrystalline graphite), and the Raman active E_2' modes of 5- and 7-membered rings. The corresponding ring statistics agree with previous results, supporting the presence of a sizable percentage of 5- and 7-membered rings, but with no 4- or 8-membered rings. This positive result provides verification for the embedded ring approach, and supports a CRN model for amorphous carbon.

(156 pages)

CHAPTER I

INTRODUCTION

Modeling the vibrational dynamics of amorphous materials presents a more difficult problem than that posed by crystalline materials. Analysis of the vibrational dynamics of crystalline materials is well established. The presence of long-range translational order (periodicity) in crystals allows analytical solution of the equations of motion by introduction of the Born-von Karman periodic boundary condition.[1] In contrast, structurally disordered--or amorphous--materials by definition lack long-range order, and are not amenable to the analytical treatments used for crystalline materials. As a consequence, other theoretical approaches have been developed to model the vibrational dynamics of disordered materials. These approaches, however, are far from definitive and yield only approximate results.

A majority of the theoretical approaches used to study the vibrational dynamics of amorphous materials are numerical approaches. The analytic approaches developed to date can be applied only to a few specific materials, and yield only qualitative results. Note that no generalized analytic approach has yet been found to model the dynamics of two-dimensional (2D) and three-dimensional (3D) amorphous materials.[2] Therefore, in contrast to the lattice dynamics of crystalline materials, the vibrational dynamics of amorphous materials offers a field of research still in its vigorous youth, and remains an open and fertile frontier for new ideas.

Limiting the scope of an analytic approach to only 2D materials reduces the complexity introduced by 3D materials. Structurally disordered 2D materials present a simpler problem theoretically by the mere fact that one dimension is eliminated. Such an analytic approach would still provide meaningful results for real materials, however. In comparison, theoretical techniques which confine themselves to even simpler systems, such as one-dimensional disordered chains, are severely restricted in applicability (for example, to polymeric compounds or chalcogenide glasses with one-dimensional networks).

This thesis addresses the problem of the vibrational dynamics of 2D disordered materials by developing a new method--the embedded ring approach. The embedded ring approach is a generalized, analytical method based upon a common structural unit present in covalent 2D materials--the planar ring. The approach examines localized vibrations in disordered 2D networks with the use of planar ring modes of oscillation. A disordered 2D network is simulated by embedding various sized rings in the network. Vibrational frequencies and modes of oscillation for the various sized rings are obtained for isolated rings and modified by coupling the rings to the network. The results comprise a spectrum of frequencies which can be compared to the vibrational density of states (VDOS) of real materials, or which can be used to generate theoretical vibrational spectra.

The embedded ring approach is limited in application to materials having planar rings. It is therefore particularly suited for modeling the dynamical behavior of 2D materials. Examples of 2D materials include physisorbed and chemisorbed monolayer films on surfaces, monolayer epitaxial films (via vapor deposition or molecular beam epitaxy), and layered materials. These materials are currently the subjects of active research areas, proving to be rich resources for both basic scientific knowledge and technological applications.

Layered materials are formed by stacking 2D planes or layers of atoms to form bulk 3D materials. In many layered materials the atoms within an individual plane or layer are strongly bonded by either covalent or ionic forces, whereas the layers themselves are only weakly bonded by forces such as the van der Waals interaction. Such intralayer forces may be an order of magnitude or more greater in strength than the interlayer forces. Layered materials with these characteristics display anisotropic properties arising from their nearly 2D nature, and can often be regarded essentially as 2D materials. Examples of such materials are the compositionally simple crystals formed by graphite, boron nitride, and several of the metal halides and metal dichalcogenides.[3,4] Many of these materials also form the basis (the intercalate) for intercalation compounds. Others are of interest because they are semiconductors, superionic conductors, or used as high technology ceramics with a variety of applications.

Other compounds with more complex compositions form materials with definite planes or layers, but with stronger interlayer bonding, usually of ionic or covalent forces. Such materials display less anisotropy, and are more intermediate in nature between 2D and 3D materials. Several silicate minerals are representative of this class of layered materials, and include biotite (mica), serpentine (asbestos), and montmorillonite (clay).[5] In the past five years, a group of complex oxide materials has risen to prominence because of the superconducting properties endowed by their layered structure. The copper oxide superconductors owe their high temperature superconductivity to a layered perovskite crystal structure, which consists of 2D copper oxide planes separated by (depending upon composition and crystal structure) alkaline earth cations, rare earth cations, thallium oxide layers, bismuth oxide layers, or lead oxide layers. The lattice dynamics of the copper oxide planes are of special importance to theorists struggling to explain high temperature superconductivity in terms of BCS theory.[6,7]

Examples of amorphous 2D materials are fewer, and yet still important as 2D analogues for amorphous 3D materials.

Physisorbed and chemisorbed monolayer films can occur as disordered phases, as can intercalants in intercalation compounds, due to a random ordering of atoms. Chalcogenide glasses go a step further, forming disordered 2D networks. (Networks differ from random packings of atoms in that the atoms in a network exhibit greater covalency in bonding and therefore a higher degree of coordination with adjacent atoms.) Amorphous As_2Se_3 and As_2S_3 are typical examples of chalcogenide glasses where the covalently bonded 2D network can be considered as one very large molecular unit (As_2Se_3 and As_2S_3 are said to form 2D-network molecular glasses).[8]

By far the most well known example of a 2D, layered material is graphite, a crystalline polymorph of carbon. Some forms of amorphous carbon also retain a 2D character, and can be modeled as 2D random networks. It is these forms of amorphous carbon which will be used as a prototypical case for the embedded ring approach in this work.

The use of amorphous carbon as a test case has several advantages. The elemental composition of amorphous carbon, consisting of only carbon atoms, simplifies calculation of the ring mode oscillations. The calculations become more complicated with materials of binary or ternary composition (comprised of two or more elements), such as with the chalcogenide glasses. Additionally, carbon is a well-studied and exhaustively characterized element in science because of its astrophysical and biological significance. Finally, vibrational spectra of various forms of amorphous carbon have been extensively published and are widely available in the literature. These spectra will permit direct comparisons of the results of the embedded ring approach to experimental data. Such comparisons will determine the validity and degree of usefulness of the embedded ring approach.

CHAPTER II

DYNAMICS AND MODELS OF AMORPHOUS MATERIALS

Vibrational Dynamics of Amorphous Materials

To understand the difficulty involved in modeling the vibrational dynamics of amorphous materials, one must start with the lattice dynamics of crystalline materials. The inapplicability of the lattice dynamical approach to amorphous materials can then be examined, and provides a stepping stone to dynamical approaches developed expressly for amorphous materials.

Loss of periodicity in amorphous materials prevents facile solution of their vibrational dynamics. In contrast, periodicity in crystalline materials facilitates determination of the dynamics. Solution of the dynamical equations for crystals yields plane waves.[1] The Born-von Karman periodic boundary condition allows simplification of the equations of motion for crystalline materials by:

1. restricting the wave vectors in the plane wave solutions to a linear combination of the reciprocal lattice vectors;
2. decreasing the number of equations to be solved.

The use of the Born-von Karman periodic boundary condition, however, is prohibited for amorphous materials due to a lack of long-range order. As a consequence, a good set of wave vectors to expand the wave functions for an amorphous material cannot be readily defined, and the number of equations to be solved remains unmanageably large. Additionally, propagating vibrations will not be in the form of plane waves, except approximately at very low frequencies. On a large enough scale, an amorphous material appears homogeneous and isotropic. At intermediate and high frequencies, vibrations in amorphous solids are localized and do not propagate as far as in crystalline materials. In some sense, the localized vibrational states in amorphous materials resemble local phonon modes created by defects in crystals.[9]

The inability to define a set of wave vectors for amorphous materials precludes the use of phonon dispersion curves to characterize their vibrational properties. Indeed, the term phonon is not even applicable to amorphous materials since the vibrational modes cannot be separated by wave vector. The vibrational density of states (VDOS), however, remains a good measure to describe the vibrational dynamics of both crystalline and amorphous materials by eschewing a frequency-wave vector relationship for a frequency-number of states per frequency interval relationship.

Figure 1(a) provides an example of a phonon dispersion curve for graphite, a crystalline polymorph of carbon.[10] Figure 1(b) displays the corresponding vibrational density of states for graphite. Note that Figure 1(b)--the VDOS--provides a means to adequately describe the vibrational

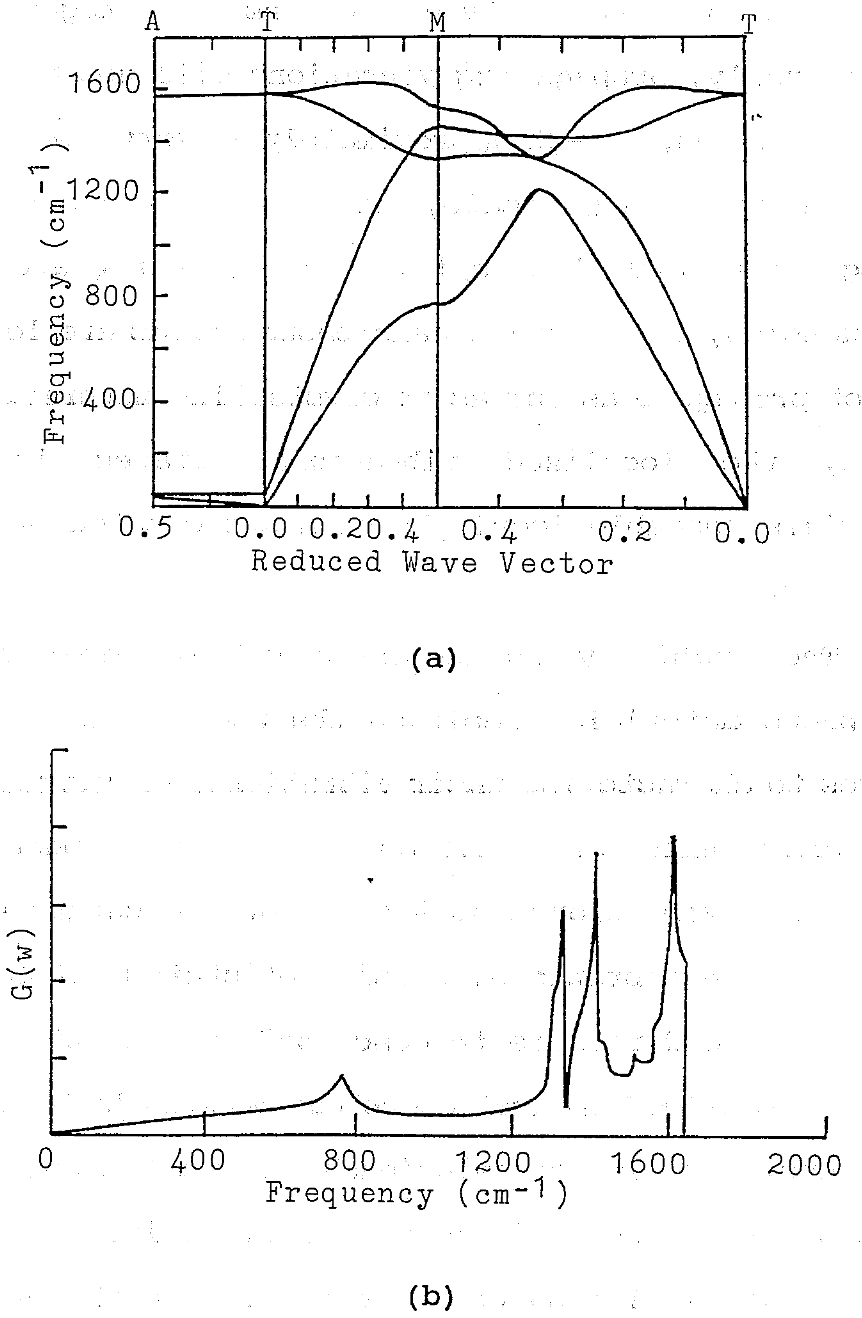

FIG. 1. Phonon dispersion curve (a) and vibrational density of states (b) for graphite. After Nemanich and Solin.[10]

states of an amorphous material as well as a crystalline material, whereas a description such as presented by Figure 1(a)--the phonon dispersion curve--would be inadequate (could not even be presented!) for an amorphous material.

The vibrational dynamics of amorphous materials can be approached either analytically or numerically. Analytical approaches examine the local dynamics of atoms in a disordered network.[2] For bonds in such networks showing a high degree of covalency, the bond-stretching force constants typically exceed the bond-angle-bending force constants by a factor of five.[2] The bonding can therefore be adequately approximated with only a central force model (i.e., only the bond-stretching forces are considered). Vibrational frequencies are calculated for a local arrangement of atoms in the network, such as a tetrahedrally coordinated or an octahedrally coordinated cluster of atoms. The calculations derive from simple expressions (solutions to either Lagrange's equations--the eigenvalue problem--or Newtonian equations of motion), and relate frequency to the atomic masses, bond-stretching force constants, and bond angles. The expressions yield bands of frequencies, with band limits determined by simple criteria and band peaks centered on non-zero vibrational modes. A number of zero-frequency modes appear due to exclusion of bond-angle-bending forces. To date, analytical approaches have been limited in usefulness, providing models which are more informative and instructive than they are quantitative.

Numerical approaches attempt to predict the VDOS for amorphous materials by considering fairly large clusters of atoms (50-500 atoms). Again, these approaches solve the eigenvalue problem as formulated with the use of quantum mechanics.[1,2] Several numerical methods are available.[2] In the cluster-Bethe-lattice method, a cluster is extracted from a disordered network, and the influence of the removed network is accounted for by attaching a branching structure (the Bethe lattice) onto each dangling bond at the edge of the cluster. The Bethe lattice models the influence of the missing embracive network by eliminating the edge or surface effects which arise from plucking a finite cluster out of an infinite network. Additionally, the Bethe lattice produces no anomalous artifacts in the VDOS. Other numerical methods employed include the negative eigenvalue method, the equation-of-motion method, and the recursion method.

The embedded ring approach is a generalized, analytical method which extends both previous analytical methods and previous numerical methods to predict vibrational modes for disordered 2D materials. The concept embodies both the use of local dynamics (analytical approaches) and the use of mathematical techniques to account for the influence of an embracive disordered network (as in the cluster-Bethe-lattice method). The embedded ring approach can also be considered a close cousin to numerical approaches since the vibrational mode intensities in the VDOS are directly computed from the ring statistics of a representative raft model (network cluster).

Because it builds upon previous methods, a literature search was conducted to assess the originality of the embedded ring approach. No references were cited from either INSPEC or Chemical Abstracts databases regarding an embedded ring approach or any similar approach for determining the vibrational properties of disordered 2D materials. References were cited, however, for articles on the vibrational dynamics of crystalline layered materials; one of these papers details calculation of the dynamics of a 2D lattice with the use of graphite as an example.[11] As with other crystalline materials, the theory for the lattice dynamics of crystalline layered materials is firmly rooted, making extensive use of periodicity in the form of point group symmetries.[3,4]

Several articles were found in the literature which examine ring vibrational modes in SiO_2 and B_2O_3-based glasses (see page 18 and Chapter IV).[12-18] Vibrational bands which appear in the Raman spectra of these glasses are attributed to ring modes of oscillation, and some analysis of the mechanism of ring mode-network decoupling is presented.

The embedded ring approach builds upon these results in an original manner. Instead of limiting itself to the specific case of ring mode-network decoupling in some materials, the embedded ring approach considers the general case of ring modes coupled to a continuous random network (CRN). Ring modes are calculated from basic principles using techniques developed for study of molecular dynamics. A method is then introduced to couple the rings to the CRN. The modified vibrational modes are then used to construct a material's vibrational spectrum. It is this approach which gives rise to the originality of the embedded ring approach.

Models of Two-Dimensional Amorphous Materials

Any successful dynamical model or approach is built upon the foundations of an accurate structural model for the material. For a crystalline material, knowledge of the crystal structure is required for determining the phonon dispersion curve. Likewise, without a good structural model, any VDOS or vibrational modes derived for an amorphous material are meaningless. A prerequisite to the development of the embedded ring approach, therefore, was to review and select structural models for 2D amorphous materials.

Amorphous materials are classified into three types of structure categories.[8] First, random close packing (RCP) models structures where nondirectional forces--metallic, ionic, or Van der Waals bonding--occur between the atoms in the material. Prototypical examples of amorphous materials exhibiting RCP structures are metallic glasses. Second, organic polymer glasses are most successfully represented by a random coil model (RCM), where interpenetrating random coils constitute the amorphous structure. The third (but definitely not the least interesting) structure category is the continuous random network (CRN). Continuous random networks arise from the disordered arrangement of atoms or molecules with covalent bonding. Covalent bonds are highly directional, resulting in low coordination number (less than or equal to four) for atoms exhibiting this type of bonding. Consequently, inorganic amorphous structures comprised of covalently-bonded atoms differ markedly from RCP and RCM structures.

Continuous random networks have been most successfully applied to covalent inorganic glasses with binary compositions. In addition to As_2Se_3 and As_2S_3, which were previously discussed in Chapter I, typical glass-forming binary compounds include B_2O_3, SiO_2, GeO_2, P_2O_3, As_2O_5, and As_2O_3.[19] Construction of CRN models for these materials requires adherence to three basic rules:

1. The coordination of each atom is fixed, limiting the degree of connectivity in the network;
2. No dangling bonds are allowed within the network;
3. A specified procedure is followed in constructing the network to ensure randomness of the structure.

Criteria (1) and (2) arise from the physical constraints imposed by the constituents of the material. The third criterion precludes subjective biasing of the structure:

human consciousness displays an inherent preference for order and regularity.

Atomic structures are typically illustrated with "ball and stick" models, which can be readily transferred to the printed page or computer screen. Three-dimensional CRN's are difficult to illustrate with two-dimensional media, however. Zachariasen schematics accomplish a 2D representation of CRN's by simply limiting the structure of the network to two dimensions. Because of this limitation, Zachariasen schematics are most amenable to compounds with an A_2B_3 stoichiometry. In fact, Zachariasen's first diagrams illustrated a CRN for an A_2B_3-type compound.[19] Figure 2(a) presents a Zachariasen schematic of a CRN for an A_2B_3-type compound. The schematic is constructed of AB_3 building blocks: The A atoms (open circles) have three-fold coordination, while the B atoms (filled circles) are only bonded to two other A atoms. Each AB_3 building block (or cluster) displays overall three-fold coordination with other AB_3 building blocks. The Zachariasen schematic is particularly useful for amorphous structures consisting of the compounds As_2Se_3, As_2S_3, B_2O_3, and As_2O_3.

Amorphous structures can also be modeled with the use of "triangle rafts" based on Zachariasen schematics.[20] As with Zachariasen schematics, triangle rafts are graphical representations of 2D structures. Figure 2(b) presents a triangle raft model of the structure shown in Figure 2(a).

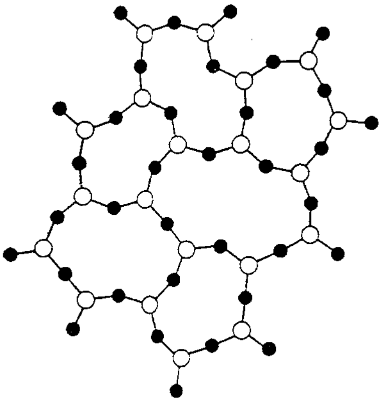

(a)

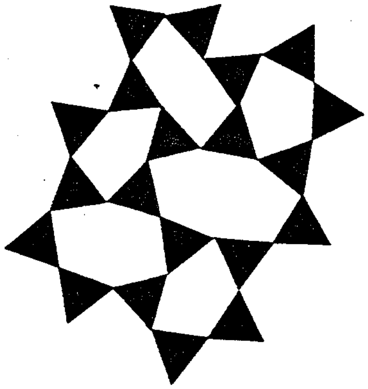

(b)

FIG. 2. Zachariasen schematic (a) and triangle raft model (b) of a two-dimensional continuous random network. After Shackelford.[20]

In Figure 2(b), triangular building blocks replace the AB_3 clusters in the Zachariasen schematic. The triangular shape of the building blocks reflects the overall three-fold coordination of the AB_3 cluster. Note that the use of triangle rafts generalizes and extends the Zachariasen schematic. The building blocks can now represent not only AB_3-type clusters, but also single atoms with planar three-fold coordination and, to some extent, the facets of tetrahedra for four-fold, tetrahedrally coordinated clusters that occur in compounds such as SiO_2 or amorphous silicon.

Continuous random networks are constructed from triangle rafts by a specified procedure.[20] The triangular building blocks form rings of various sizes. A CRN is built by first starting with an initial ring. Subsequent rings are then added to the initial ring in a clockwise spiral fashion, with the size of each ring selected randomly. The final structure is a CRN comprising an assemblage of rings of diverse size. The distribution of n-membered rings (n=3 to about 10) provides a measure for the randomness of the 2D network. Therefore, triangle raft models provide a means to theoretically determine the ring statistics for amorphous materials.

Ring statistics for real glasses are difficult to determine experimentally. However, ring statistics for vitreous SiO_2, B_2O_3, and various SiO_2-B_2O_3 glasses have been determined with the use of infrared and Raman spectra.[12] The determinations were accomplished by looking for B_3O_6 boroxol ring vibrational modes in the spectra, and with the use of numerical methods to compute the VDOS. Raman spectra may also be used to determine the ring statistics for vitreous silica and various silicate glasses.[13]

Chapter IV discusses ring mode decoupling in silica-based materials, and details the embedded ring approach, a theoretical method which may bridge the gap between experimentally determined and theoretically predicted ring statistics for amorphous materials other than amorphous silica, silicate, and borate glasses. Triangle rafts present model CRN structures from which the ring statistics are readily obtained. The embedded ring approach uses these ring statistics to construct theoretical spectra for comparison with real vibrational spectra of materials. Such comparisons permit the correlation between a material's atomic structure and the model structure.

Note that triangle raft models can be extended to crystalline and quasicrystalline structures as well. Amorphous structures display a distribution of three or more different ring sizes. Crystalline structures, by contrast, would display either a single, bimodal, or multimodal distribution of 3-, 4-, 5-, 6-, or 8-membered rings. Such rings have the necessary symmetries for a periodic structure. Figure 3 shows a triangle raft model (a) and ring statistics (b) for a 2D crystal structure comprised of 4- and 8-membered

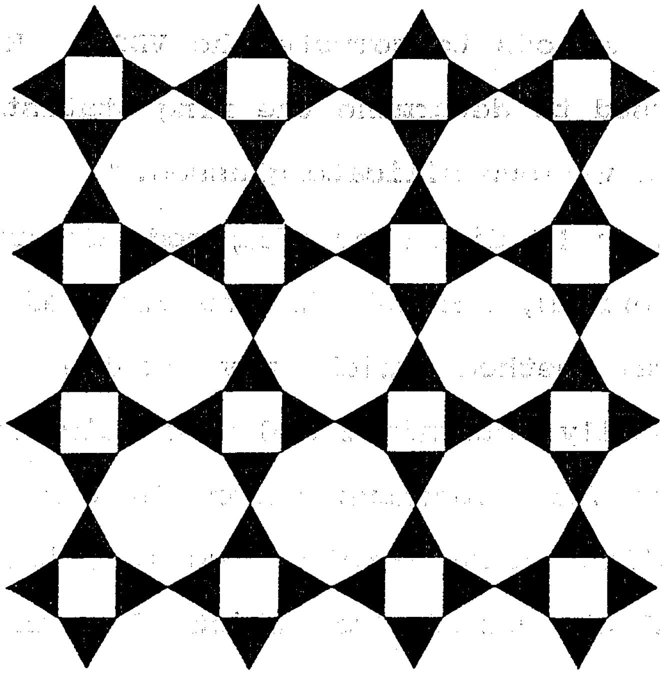

(a)

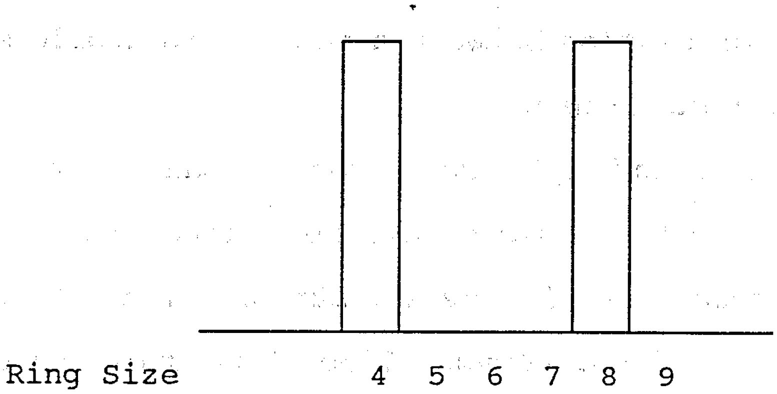

(b)

FIG. 3. Triangle raft model (a) and ring statistics (b) for a (4,8) crystalline two-dimensional material.

rings. Figure 4 displays the unit cell (a) and ring statistics (b) for another crystal structure, this time consisting of 5- and 8-membered rings. Surprisingly, the crystal structures in Figures 3 and 4 are not just theoretical models, but represent actual crystal structures for some silicate minerals.[21] The triangular building blocks in Figures 3 and 4 represent the faces of SiO_4 tetrahedral clusters for the silicate minerals apophyllite and okenite, respectively. As mentioned in Chapter I, many silicate compositions form quasi-2D materials.

Two-dimensional quasicrystalline structures may be characterized by a bimodal or multimodal distribution of rings. Five or ten-membered rings provide five-fold symmetry for aperiodicity, and at least one other structural unit (ring size) is necessary to eliminate lattice frustration. Such a quasicrystalline structure is analogous to a 2D Penrose tiling where at least two structural units are required.[22,23] Figure 5 shows a 2D network displaying local five-fold symmetry. Note, however, that the network in Figure 5 is not truly quasicrystalline since lattice frustration is not fully alleviated. The structure in Figure 5 would more likely curl up into a sphere, much like the carbon network does in Buckminsterfullerene due to the presence of five-membered rings.[24-26]

Triangle rafts model continuous random networks with a variety of compositions (elemental to ternary), and also

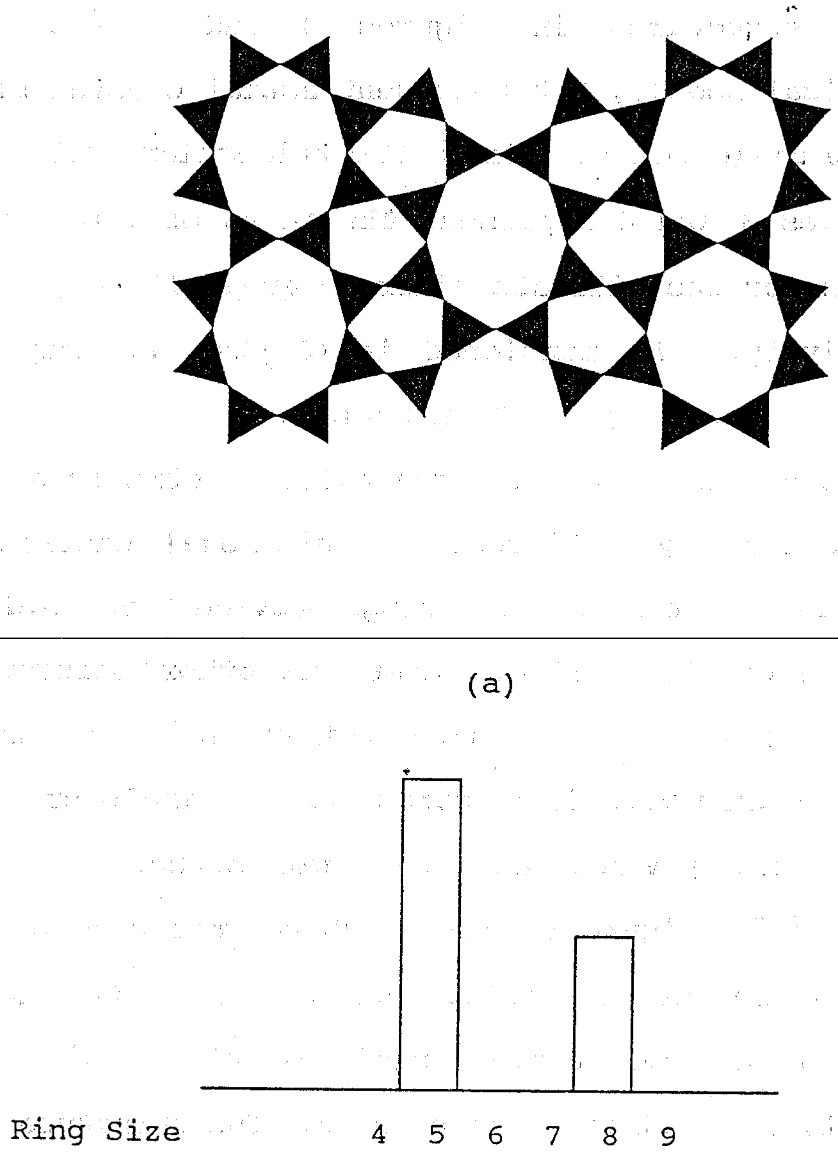

(a)

(b)

FIG. 4. Triangle raft model (a) and ring statistics (b) for the unit cell of a (5,8) crystalline two-dimensional material.

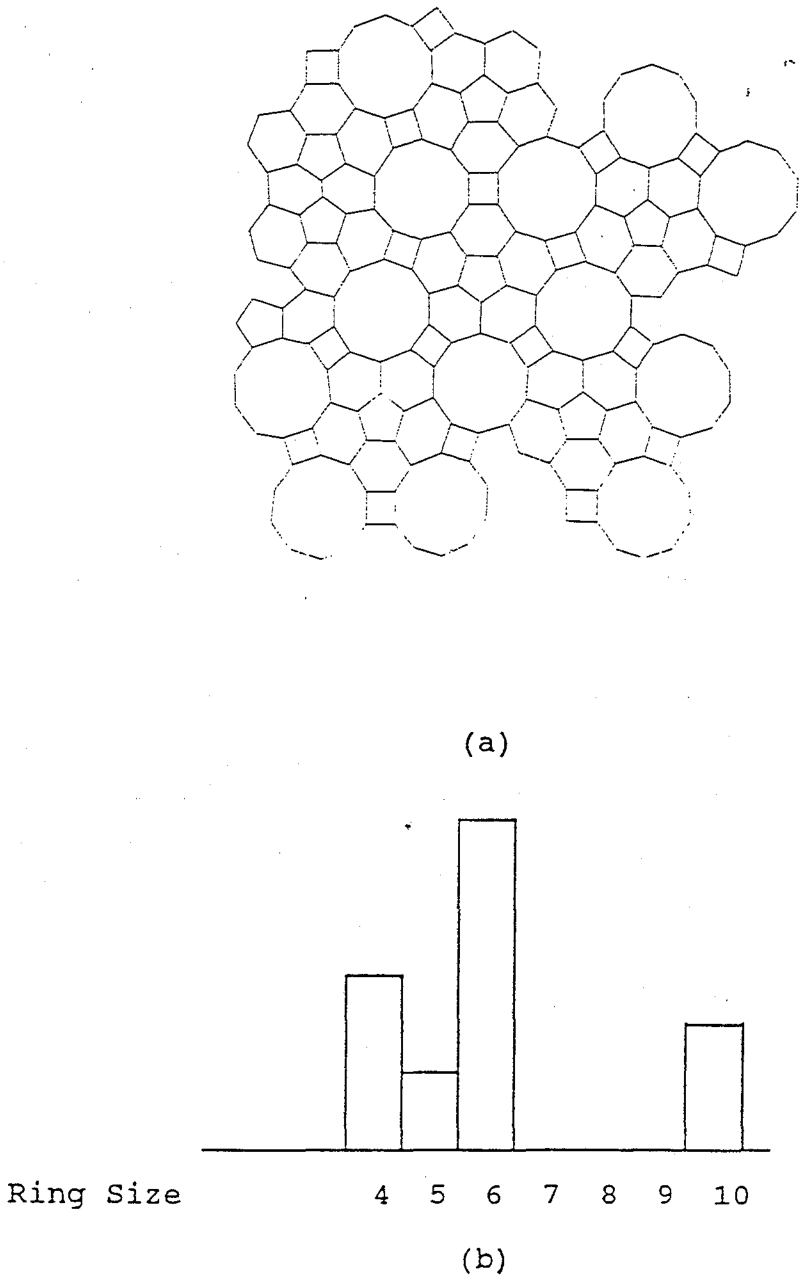

FIG. 5. Two-dimensional network displaying local five-fold symmetry (a) and corresponding ring statistics (b).

model other structures within the hierarchy of order-disorder (crystalline--quasicrystalline--amorphous). These abilities, along with their emphasis on ring size and ring statistics, make the use of triangle rafts amenable to a theoretical approach of the vibrational dynamics of amorphous materials based upon ring modes of oscillation.

Geometry and Dimensionality of Networks

As previously discussed in this chapter, the structural randomness of a 2D network is intimately tied to the shape/size of the rings constituting the network (pentagonal 5-membered rings, hexagonal 6-membered rings, etc.), and their relative population in the network (i.e., the ring statistics). Also influenced by ring geometry and statistics is the dimensionality of the network. Certain ring geometries and abundances can introduce curvature into a normally flat, 2D network. The network is still two-dimensional, but now curved or warped into a third dimension. Such network warpage or curvature can have material property effects, and is an important structural factor to characterize. Again, the ring statistics for a network can provide a measure for the amount of warpage/curvature in a normally 2D amorphous material.

We can examine this relationship by considering a periodic, hexagonal lattice comprised of only 6-membered rings. A 5-membered ring is introduced into the lattice by modifying a 6-membered ring (for example, by creating a vacancy defect). The atoms at the vertices of the 5-membered ring still exhibit three-fold coordination, but the bond angles have changed. Two of the bond angles at the vertex atoms are shared by 6-membered rings, and are therefore 120° each. The third bond angle is an interior angle within the pentagonal 5-membered ring, and is therefore only 108°. The sum of the three bond angles is 348°. To maintain a flat 2D geometry, all three bonds must lie in the same plane, and the bond-angle sum should equal 360°. Therefore, a 12° angular deficiency exists at each vertex atom of the introduced 5-membered ring. Since there are five vertex atoms, the total angular deficiency for the introduced 5-membered ring is 60°.

The effect of this 60° angular deficiency is to pucker the lattice at the 5-membered ring site. The normally flat 2D lattice can no longer maintain its flatness, but must curve to accommodate the 5-membered ring "defect." Adding more 5-membered rings to the lattice increases the curvature. Finally, with only twelve 5-membered rings equally spaced in the 2D lattice, sufficient curvature is created to curl the lattice into a sphere.

Note that the required number of 5-membered rings to curl the lattice into a sphere remains twelve, independent of the size of the lattice or the spacing between the 5-membered rings. This phenomenon was discovered in the 18th century by Leonhard Euler, and remains a topological intrigue and curiosity.[27] The total angular deficiency for twelve 5-membered rings is

$$12\times 60^\circ = 720^\circ$$

the angular deficiency necessary to completely curve a two-dimensional space in upon itself.

The effect of introducing a 7-membered ring into a hexagonal lattice is equally interesting. The 7-membered ring creates a total angular excess of 60°. Again, the lattice puckers at the 7-membered ring site. The curvature is different, however, from that induced by a 5-membered ring. Whereas an angular deficiency creates spherical curvature, an angular excess creates hyperbolic curvature.

We can now begin to see how a 2D-CRN can accommodate both 5- and 7-membered rings, and yet retain its flatness. The angular deficiencies created by a number of 5-membered rings can be canceled by the angular excesses of an equal number of 7-membered rings. The occurrence of 4-membered rings also creates angular deficiencies, 120° total for each ring, with corresponding angular excesses occurring for 8-membered rings. Note, for example, Figure 3 where equal numbers of 4- and 8-membered rings create a flat, 2D lattice. The angular deficiencies of two 5-membered rings can also cancel the angular excess of an 8-membered ring, again leading to a flat 2D lattice, as in Figure 4.

The ring statistics for an amorphous material provide the relative proportions of 4-, 5-, 6-, 7-, and 8-membered rings in the CRN. From the ring statistics one can determine the relative flatness of the 2D-CRN. A simple equation to do this is the following:

$$-N_3\times180^\circ-N_4\times120^\circ-N_5\times60^\circ+N_7\times60^\circ \\ +N_8\times120^\circ+N_9\times180^\circ=\delta$$

where N_n = equals the number of n-membered rings (3- and 9-membered rings were included for completeness), and δ is the curvature of the 2D-CRN. (Note that the above equation is only valid for a 2D-CRN where the atoms or atomic clusters exhibit three-fold coordination.) If $\delta \approx 0$, the 2D-CRN is relatively flat. If $\delta < 0$ or $\delta > 0$, the 2D-CRN has spherical curvature or hyperbolic curvature associated with it, respectively. The curvature or flatness should be considered a large scale parameter, taken over several atom-atom bond distances (10-100 Å). Local puckering of the network may occur due to local ring geometry or inhomogeneous ring distributions.

The preceding discourse has many uses. For instance, the inability to tile a flat 2D surface with only pentagons or septagons is given further depth beyond that of symmetry arguments.[28] In the context of the embedded ring approach, the ability to determine an amorphous material's ring statistics, and subsequently the structure of the CRN in terms of randomness and curvature (dimensionality), lends further value to the approach. Finally, an understanding of ring geometry and network dimensionality is essential in constructing accurate structural models for amorphous materials.

Buckminsterfullerenes

The curling of a hexagonal lattice into a sphere by the addition of twelve 5-membered rings is more than just a theoretical curiosity. The recent discovery of Buckminsterfullerenes [29] (named after the inventor of the geodesic dome, Buckminster Fuller) provides an actual physical system where such an event occurs on the atomic scale.

Buckminsterfullerene is a molecular form of carbon produced and discovered so far only in the laboratory. The existence of this exotic molecule in naturally occurring samples or, as predicted, in interstellar dust clouds has yet to be confirmed.[30] The chemical formula for the prototypical Buckminsterfullerene molecule is C_{60}, although a whole series of Buckminsterfullerenes (also called fullerenes) has been predicted (C_{24}, C_{28}, C_{32}, C_{36}, C_{50}, C_{60}, C_{70}, and so on).[24] C_{60} was the first fullerene discovered, with other members of the series subsequently found.[31]

C_{60} is clearly comprised of 60 carbon atoms which form a molecular cage or spherical network. This cage or network itself is comprised of twenty 6-membered rings and twelve 5-

membered rings. Figure 6 presents a triangle raft model (a) and the ring statistics (b) for C_{60}. The carbon network can be considered as a 2D hexagonal lattice, as in graphite, within which twelve 5-membered rings have been introduced. The 5-membered rings completely curl the network into a self-contained sphere. All of the molecules in the fullerene series have exactly the same number of 5-membered rings--twelve; only the number of 6-membered rings varies.

This new form of carbon has captured the interests of the physics community. Its material properties are as exotic as the molecular structure itself. Doped with potassium or rubidium, solid C_{60} is a respectable superconductor with critical temperatures of 18 and 28 K, respectively.[32,33] Because of its completely enclosed, self-contained structure and the strength of the covalent carbon-carbon bonds, some researchers suggest that C_{60} might be harder than diamond.[34] Most recently, the discovery that carbon lattices can roll into tubular structures with closed, fullerene-like ends opens a new avenue for the development of novel carbon fibers.[27,35] Additionally, new forms of carbon with hyperbolic curvature (comprised of 6- and 7-membered rings) have also been proposed and theoretically examined.[36]

This thesis has a dual interest in fullerene molecules. First, fullerene molecules are an example of a 2D hexagonal lattice which is profoundly altered by the presence of 5-membered rings. The effects of ring size and statistics on

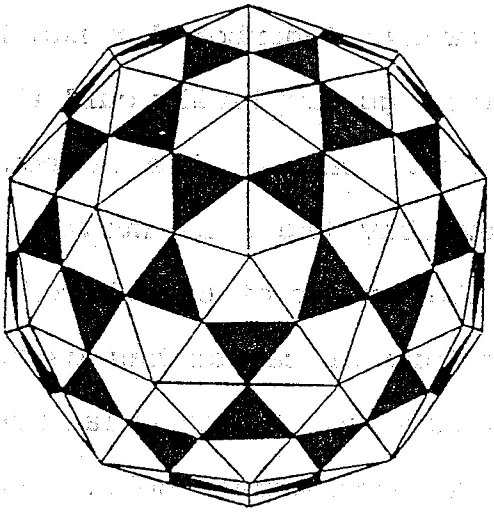

(a)

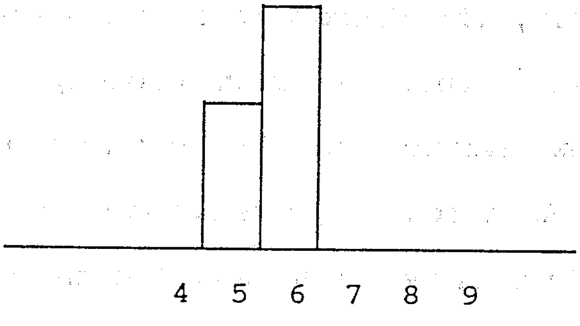

(b)

FIG. 6. Triangle raft model (a) and ring statistics (b) for the fullerene molecule C_{60}.

a material's atomic structure are clearly demonstrated with fullerene molecules. Second, fullerene molecules are a close kin to a specific structural model for amorphous carbon. The network in this structural model contains not only 5- and 6-membered rings, but 7-membered rings as well. The 7-membered rings counteract the sphericity induced by the 5-membered rings, but also introduce a random structure into the network. The ring statistics for such a network should have approximately equal numbers of 5- and 7-membered rings to prevent the formation of large, spherical molecules. The following chapter details this structural model for a-C.

CHAPTER III

CARBON AND CARBON MODELS

Crystalline and Amorphous Carbon

Naturally occurring elemental carbon most commonly exists as two allotropic forms in the crystalline state--graphite and diamond. Graphite is a layered material, with strong intraplanar covalent forces bonding the atoms into 2D layers. Relatively weak interplanar forces hold the 2D layers together to form a 3D solid. The covalent bonds of the carbon atoms in graphite, designated sp_2 bonds, exhibit planar three-fold coordination and give rise to the familiar graphite hexagonal structure. Figure 7 is a triangle raft model of graphite, displaying the regular six-membered rings which comprise the hexagonal structure. Note that because of the planar three-fold coordination, triangle raft models are ideal representations for carbon structures bonded primarily by sp_2 bonds. Each triangle in the raft model represents a single carbon atom, with the apexes representing the three bonds.

The second allotropic form of crystalline carbon, diamond, is a 3D solid forming crystals with cubic symmetry. In contrast to graphite, the carbon atoms in diamond have covalent bonds which exhibit tetrahedral, four-fold coordination. The tetrahedrally coordinated forces, designated sp_3 bonds, allow the carbon atoms to bond in a 3D

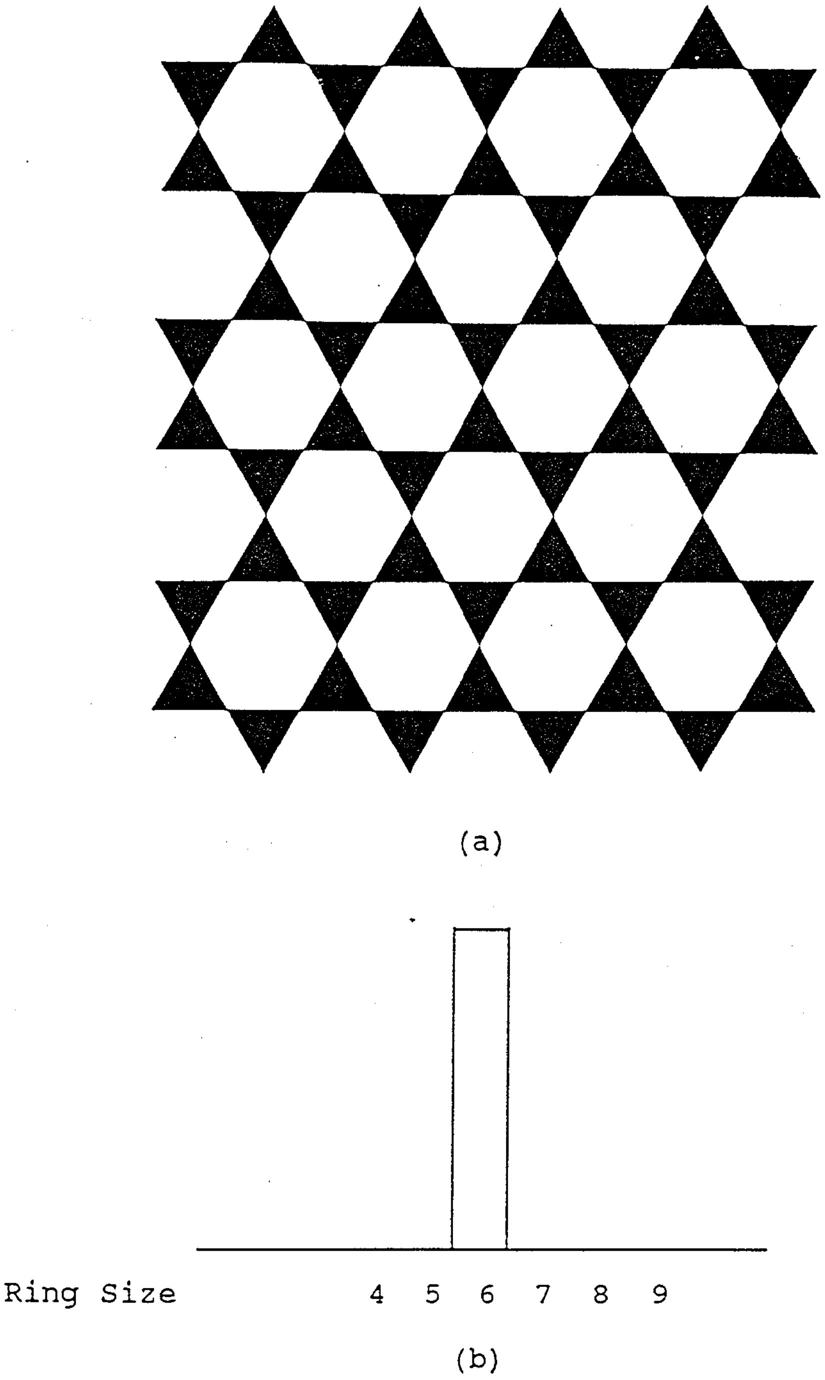

FIG. 7. Triangle raft model (a) and ring statistics (b) for graphite displaying hexagonal structure.

framework, and give diamond crystals their cubic crystal structure.

Crystalline carbon may occur in other forms as well, usually as microstructural alterations of pristine graphite or diamond. The designation "glassy carbon" is a common misnomer, since it is not a true glass or amorphous material; rather it consists of strained graphite layers stacked randomly to form carbon fibrils.[37] Carbon fibrils are ribbon-like microstructures of graphite and are typically less than 120 Å in width and 40 Å in thickness. Oriented carbon fibrils greater than 1000 Å in length comprise the structure of carbon fibers. In glassy carbon, however, the carbon fibrils are not oriented, and intertwine into an extensive tangled, knotted structure. Because of their structural similarities to graphite at the atomic level, the bonds in glassy carbon and carbon fibers are almost entirely of the sp_2 type.

Nanocrystalline graphite (also called turbostatic carbon or carbon black) is also derivative of the graphite structure, with local ordering of carbon atoms giving rise to a 2D hexagonal structure. The spatial extent of the hexagonal ordering, or domain size, in nanocrystalline graphite differentiates it from other forms of carbon. The ordered domains can be likened to the grains in a polycrystalline material; each grain is a single, ordered crystal structure randomly oriented crystallographically with respect to neighboring grains. Domains in nanocrystalline graphite range in size from 16 Å to 38 Å.[38] Although sp_2 bonds characterize the graphitelike domains in nanocrystalline graphite, sp_3 bonds are likely present at domain boundaries.[37] Again, as with glassy carbon, nanocrystalline graphite is not truly amorphous, but rather exhibits crystallinity on a very fine scale.

Microcrystalline diamond is analogous to nanocrystalline graphite, and is typically observed in thin diamond films.[39] In contrast to graphite and its crystalline derivatives (glassy carbon, carbon fibers, and nanocrystalline graphite), sp_3 bonding predominates in microcrystalline diamond, resulting in the diamondlike crystal structure on a very fine, local scale. The domains in microcrystalline diamond, however, are much larger (up to 1 μm) than those found in nanocrystalline graphite.

The previous discussion highlights the difficulty in ascertaining an amorphous state for carbon. Aside from the many modifications in crystallinity carbon may assume, amorphous carbon does exist. Two principal criteria define an amorphous state for carbon:

1. A mixture of sp_2 and sp_3 bonds exists, with the proportion of sp_2 to sp_3 bonds denoting a gradual shift in the nature of the amorphous carbon from graphitic to diamondlike;

2. Short-range order is limited to less than 5 Å, precluding the presence of nanocrystalline domains.

These criteria can be determined experimentally with the use of Raman spectroscopy, electron and neutron diffraction, electron energy loss spectrometry, and (e,2e) spectroscopy. Further comparison with theoretical models narrows the criteria down to a specific structural model for amorphous carbon.

The coexistence of both sp_2 and sp_3 bonds profoundly affects the structure of amorphous carbon. The 3D nature of the sp_3 bonds warps and distorts the 2D atomic configurations arising from sp_2 bonds. Consequently, a low sp_2/sp_3 bond ratio implies an amorphous structure with a high degree of 3D connectivity, and is therefore diamondlike in quality. Conversely, a high sp_2/sp_3 bond ratio indicates a quasi-2D amorphous structure with sp_3 bonds introducing distortions in the 2D planes. Amorphous carbon with a high sp_2/sp_3 bond ratio therefore displays graphitic qualities.

Structural Models of Amorphous Carbon

Beeman *et al.*[40] constructed three structural models for amorphous carbon (a-C) with various sp_2/sp_3 bond ratios. Radial distribution functions (RDF's), VDOS spectra, and Raman spectra were then numerically computed for each of their models. (Beeman *et al.* calculated the VDOS and Raman spectra with the use of the equation-of-motion method.)

Comparisons of model RDF's with RDF's obtained for a-C with the use of neutron diffraction were inconclusive in selecting a preferred model for a-C. Comparisons with VDOS and Raman spectra, however, revealed that the most probable model for a-C has a sp_2/sp_3 ratio greater than 9 (less than 10% sp_3 bonds). They concluded that the structure of a-C was therefore primarily 2D, with occasional sp_3 bonds interspersed in the network.

Electronic band structures were determined for an a-C film with the use of (e,2e) spectroscopy,[41] and the results support the conclusions of Beeman et al. The electronic band structures for the a-C film were more consistent with a graphitic type of carbon structure than with a diamondlike carbon structure. Further studies with (e,2e) spectroscopy revealed that both evaporated a-C and ion-sputtered a-C contained primarily sp_2 bonds, but that a dependence of electronic structure on preparation method also existed.[42]

Electronic properties computed with the use of model structures by Galli et al.[43] are also supportive of a distorted, 2D network model for a-C. Their results agree reasonably well with experimental data, and indicate an sp_2/sp_3 ratio of 4 to 9 (10-20% sp_3 bonds) and clustering of the sp_3 bond sites. The structural models used by Galli et al. consisted of random, highly distorted 2D layers with 5-, 6-, and 7-membered rings.

Li and Lannin [44] measured radial distribution functions of a-C films with the use of neutron diffraction, and concluded that although the bonding was predominantly sp_2, no third nearest neighbor peak was observed which would correspond to a hexagonal structure. The absence of hexagonal ordering in a-C provides further evidence for a 2D continuous random network with 5- and 7-membered rings in addition to 6-membered rings.

To summarize, substantial evidence exists for a structural model of a-C which consists of a locally 2D-CRN with mostly sp_2 bonding and with regions of 3D connectivity at sp_3 bond sites. The 2D network will be comprised of rings of various size (mostly 5-, 6-, and 7-membered rings, but possibly also including some 4- and 8-membered rings), and will be warped and/or wrinkled near sp_3 sites. Such a structural model is agreeable to the type of analysis used by the embedded ring approach, and this model is used as a test case for the embedded ring approach in this work.

Note that other forms of a-C exist for which this model is inapplicable. The types of a-C obtained in the laboratory are highly dependent on how the a-C is prepared; choice of deposition method and conditions during deposition (temperature, pressure, starting materials, etc.) determine the atomic structure and therefore the material properties of the resulting a-C. Hydrogenated a-C exhibits a larger proportion of sp_3 bonds due to hydrogen stabilization, and is therefore more diamondlike in properties and atomic structure. Similarly, diamondlike a-C also has a large proportion of sp_3 bonds and exhibits diamondlike characteristics (e.g., hard and transparent). This thesis, however, will not be concerned with hydrogenated or diamondlike a-C due to complications which may arise in the vibrational dynamics due to hydrogen bonding and greater 3D connectivity.

Figure 8(a) represents the structural model for a-C, displaying a 2D-CRN, but with the distorted sp_3 regions omitted. Each triangle in this triangle raft model represents a three-fold coordinated (sp_2 bonded) carbon atom. Also note the randomness of the structure and diverse size of the rings which comprise the network.

Figure 8(b) presents the ring statistics for the CRN in Figure 8(a). The ring statistics indicate that the majority of rings are 5-, 6-, and 7-membered. Additional 4-, 8-, and 9-membered rings complete the structure. Note that such a CRN for a-C provides a truly random structure, with short-range order not exceeding second nearest neighbors (agreeing with the results of Li and Lannin [44]) and with a relatively low population of six-membered rings (showing substantial deviation from the hexagonal structure of graphite).

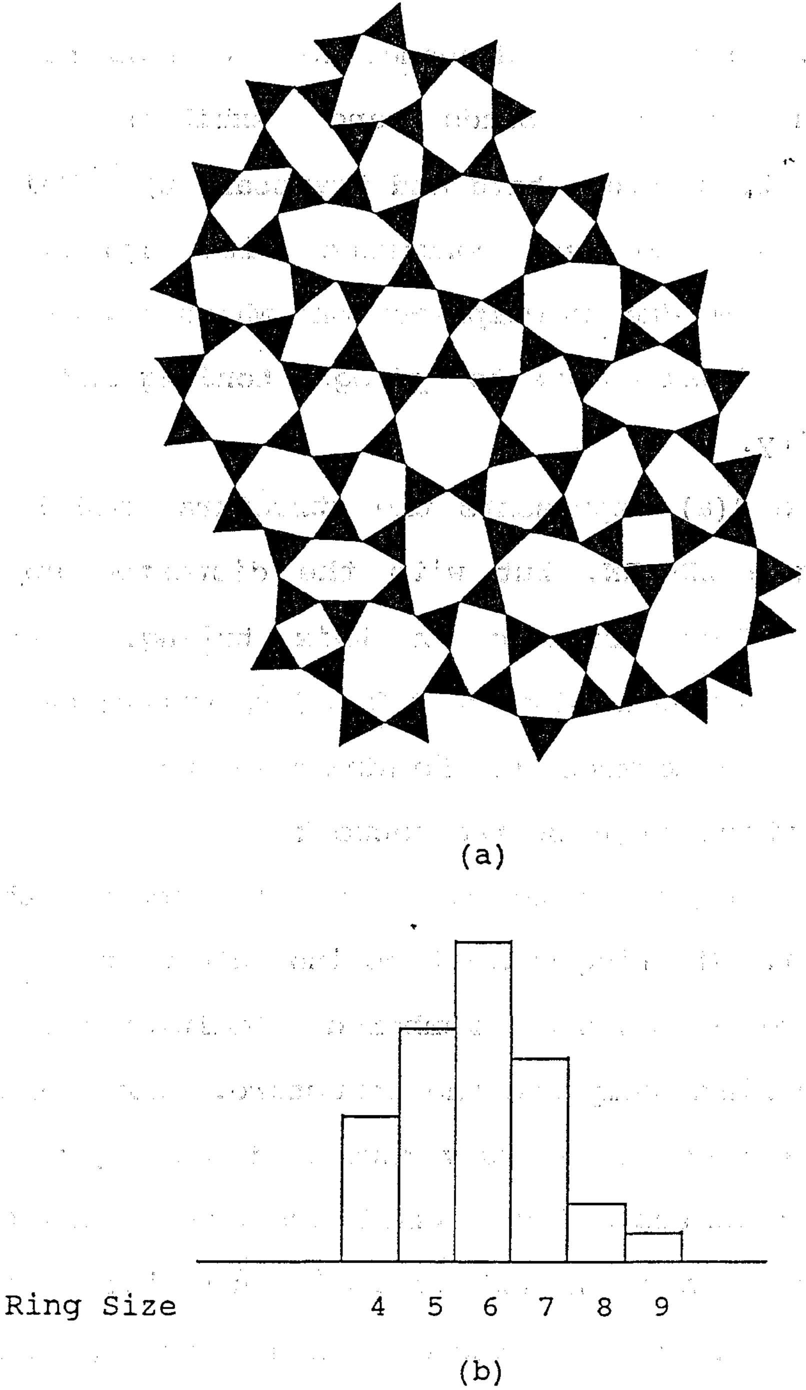

FIG. 8. Triangle raft model (a) and ring statistics (b) for amorphous carbon with continuous random network structure.

Vibrational Spectra of Amorphous Carbon

As mentioned previously, several characterization methods exist (for example, diffraction techniques and (e,2e) spectroscopy) to ascertain the atomic and electronic structure of various forms of crystalline and amorphous carbon. Raman spectroscopy is particularly useful for discerning the structure of carbon since Raman spectra are sensitive to both long-range order (for crystalline materials) and short-range order (for amorphous materials). The Raman effect was discovered in 1925 by C. V. Raman, who, coincidentally, obtained the first Raman spectrum from diamond, a crystalline form of carbon.[45] The Raman effect relies upon the inelastic scattering of light quanta (photons) from molecules and solids. The scattered photons gain or lose energy from vibrational modes in the molecules or solid. The change in frequency of the scattered photon corresponds to the frequency of the vibrational mode. Since the vibrational frequencies are structurally dependent, the Raman effect provides an experimental technique spanning the bridge between atomic structure and vibrational dynamics.

Structural symmetry in crystals gives rise to Raman selection rules for the vibrational modes, and the Raman spectra are indicative not only of molecular vibrations (internal modes), but of crystal structure (external or phonon modes) as well. Relaxation of the Raman selection rules for crystals may arise from two conditions:

1. Transformation or distortion of the crystal structure to a crystal structure with lower symmetry;
2. A decrease in long-range order due to crystalline domain boundaries in microcrystalline or nanocrystalline materials.

Nominally inactive Raman modes appear in the Raman spectrum when the Raman selection rules are relaxed, and the inactive modes are diagnostic of microstructural alterations in the crystalline material. Breakdown of the Raman selection rules occurs in truly amorphous materials due to a complete lack of long-range order and structural symmetry. Raman selection rule breakdown allows all vibrational modes to appear in the Raman spectrum, and the Raman spectrum approximates the VDOS.[46-48]

The Raman spectrum of graphite, Figure 9(a), exhibits a single, sharp peak at 1580 cm^{-1} and a low-frequency peak at 50 cm^{-1} arising from the Raman active E_{2g} modes.[49] The E_{2g} modes are the only Raman active fundamentals for graphite, which has the D^4_{6h} space group (homomorphic to the D_{6h} point group). The Raman spectrum of diamond displays a single Raman active mode at 1332 cm^{-1}.[37]

In addition to the 1580 cm^{-1} E_{2g} mode, a strong peak at 1360 cm^{-1} and a smaller peak at 1620 cm^{-1} appear in Raman spectra of nanocrystalline graphite, Figure 9(b).[49,50] The

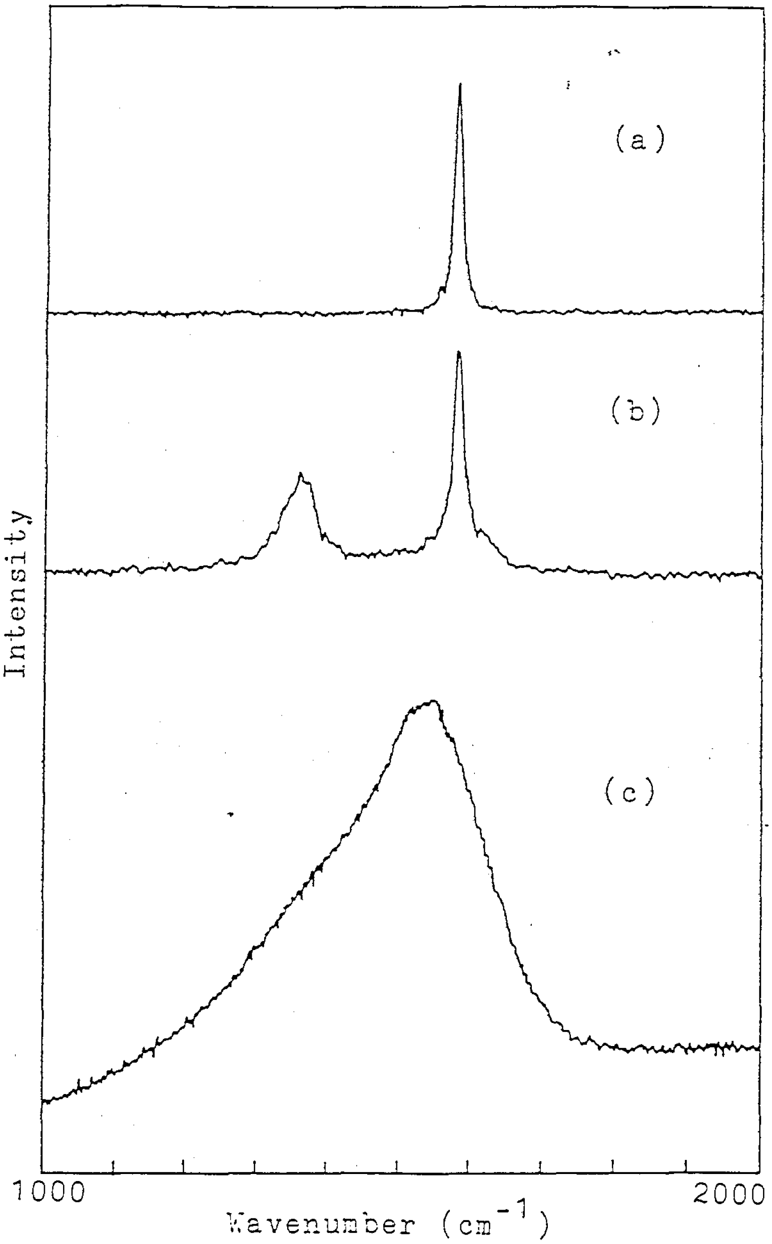

FIG. 9. Raman spectra of graphite (a), nanocrystalline graphite (b), and amorphous carbon (c). After References 49 and 50.

intensity of the 1360 cm^{-1} band is inversely proportional to the crystallite size, and can be attributed to relaxation of the Raman selection rules for graphite.[10,38,51-54] The loss of long-range translational order in the hexagonal lattice due to finite crystallite size allows the normally Raman-inactive A_{1g} mode to become Raman active. Note that although the A_{1g} mode is Raman inactive for an infinite hexagonal lattice, it is Raman active (along with the E_{2g} mode) for a single, 6-membered carbon ring with D_{6h} point group symmetry, and for larger yet finite assemblages of 6-membered rings as well (i.e., polycyclic aromatic hydrocarbon molecules).

The 1620 cm^{-1} line in the spectra of nanocrystalline graphite is too close to the 1580 cm^{-1} line to be distinct. Rather, it merges with the 1580 cm^{-1} line to form a shoulder on the 1580 cm^{-1} peak, and shifts the 1580 cm^{-1} peak to a slightly higher frequency. The origin of the 1620 cm^{-1} line is still unresolved, but most likely results from the appearance of a feature in the graphite VDOS, again due to relaxation of the Raman selection rules.[53]

In contrast to the Raman spectra of graphite and nanocrystalline graphite, the Raman spectrum of amorphous carbon, Figure 9(c), presents a broad, asymmetrical band centered at 1550 cm^{-1}.[50] It is unclear whether the band in amorphous carbon represents a true vibrational density of states, with contributions from vibrational modes of larger and smaller rings in a continuous random network (the CRN-

VDOS interpretation), or whether the band results from disorder-induced broadening and frequency-shifting of the E_{2g} graphite mode at 1580 cm^{-1}.

Resonant Raman spectra of diamondlike a-C films provided evidence that the broad band in diamondlike a-C is comprised of two components at 1400 cm^{-1} and 1530 cm^{-1}.[55] The 1400 cm^{-1} and 1530 cm^{-1} components can be associated with aromatic, sp_2-bonded carbon rings of large and small sizes, respectively. The structural models and numerical calculations of Raman spectra by Beeman _et_ _al_. also support a CRN-VDOS interpretation for the Raman spectrum of amorphous carbon.[40]

The embedded ring approach will attempt to determine if the broad band in Raman spectra of a-C could arise from contributions from the vibrational modes of diverse-sized rings. The diverse-sized rings would constitute a CRN, with each n-membered ring contributing a distinct set of vibrational mode frequencies to the VDOS. Thus, the application of the embedded ring approach to the vibrational spectra of a-C provides an analytical approach to verify the CRN-VDOS interpretation.

Polycyclic Aromatic Hydrocarbons

An important step in developing the embedded ring approach is to determine the effect of the surrounding network on the vibrational modes of the embedded ring. A single, isolated ring will have a set of vibrational modes with one or two frequencies for each singly-degenerate or doubly- degenerate vibrational species. Embedding the ring modifies these mode frequencies. The extent and nature of the frequency modification can be studied in a regular, stepwise progression by first examining the vibrational modes of an isolated ring. The surrounding network is then constructed in stages by adding additional rings to the isolated ring. Frequency changes are noted for each ring added. Finally, the effect of a surrounding network on the embedded ring can be inferred by examining the relationship between the frequency of a specific mode and the number of rings coupled together.

The above analysis is made easier by the existence of polycyclic aromatic hydrocarbons (PAH's). PAH molecules consist of carbon rings coupled together in a variety of configurations and sizes (Figure 10). The carbon ring bonds are sp_2 in nature, and the dangling bonds are typically taken up by hydrogen. The hydrogen atoms vibrate at higher frequencies than the carbon atom ring motions because their mass is much less than that of the carbon atoms. Additionally, the motions of the hydrogen atoms have only a small effect on the carbon atom ring motions and therefore, to a first approximation, can be ignored for the above analysis. Although most PAH's are comprised of 6-membered rings, some contain 4-, 5-, and 7-membered rings. The vibrational dynamics of several PAH molecules are dispersed

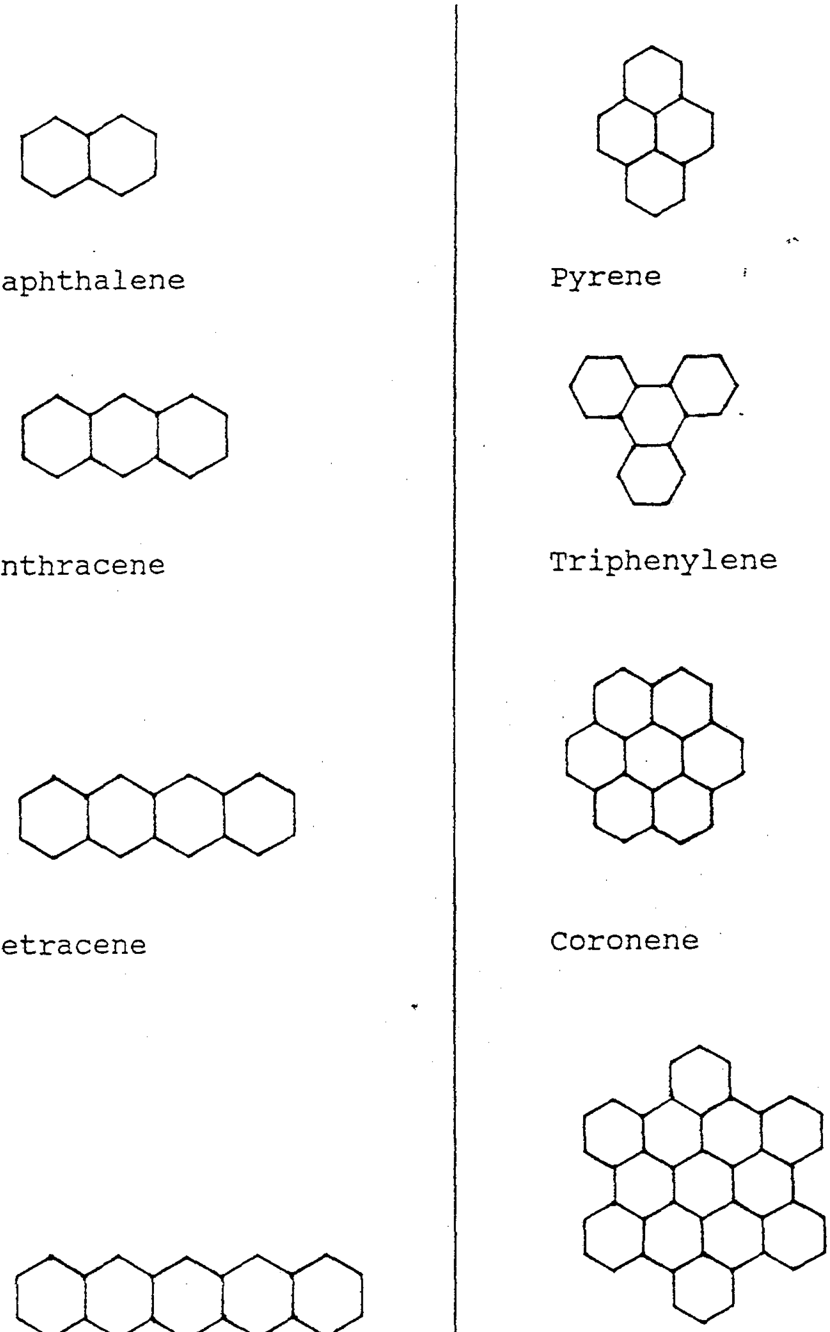

Naphthalene

Anthracene

Tetracene

Pentacene

Pyrene

Triphenylene

Coronene

Hexabenzocoronene

FIG. 10. Molecular structures of selected polycyclic aromatic hydrocarbons.

throughout the literature.

Benzene is the simplest aromatic hydrocarbon, and is the archetype for an isolated, 6-membered carbon ring. Adding 6-membered rings in a linear, chain-wise fashion to benzene creates the PAH molecules of naphthalene (2 rings), anthracene (3 rings), tetracene (4 rings), and pentacene (5 rings). Analysis of a specific mode frequency for these 6-membered ring structures would provide clues to the nature of ring mode-network coupling in graphite and a-C. The E_{2g} mode is selected because of its Raman activity in spectra of graphite and PAH molecules, and because it is an in-plane vibrational mode. The E_{2g} mode for benzene has a measured frequency of 606 cm^{-1}.[56] An E_{2g}-like mode for naphthalene, where the atomic motions in each ring approximate the motions for the E_{2g} mode in benzene, displays a frequency of 1162 cm^{-1}. E_{2g}-like modes for anthracene, tetracene, and pentacene have frequencies of 1557 cm^{-1}, 1554 cm^{-1}, and 1552 cm^{-1}, respectively.[57]

A trend is observed for the E_{2g}-like mode frequencies for the linear PAH molecules when they are plotted as a function of the number of rings for each molecule (Figure 11). The E_{2g} mode frequency for the isolated ring (benzene) increases with the number of rings added until anthracene (3 rings). After anthracene the frequency changes little, and will probably not change significantly for molecules larger than pentacene. Note that the final frequency limit for the E_{2g}-like modes--

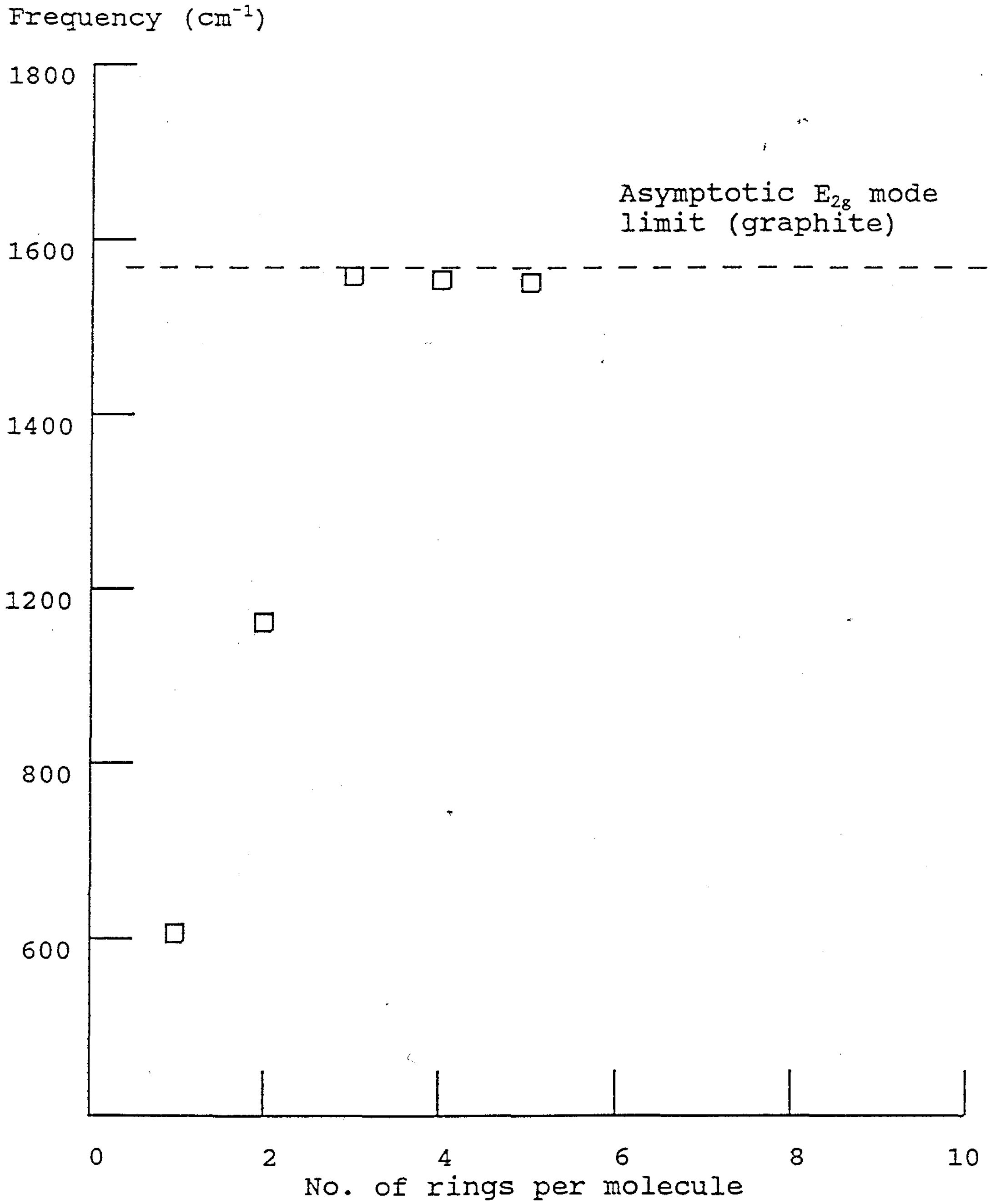

FIG. 11. Relationship of E_{2g}-like mode frequencies with number of rings per molecule for benzene, naphthalene, anthracene, tetracene, and pentacene.

about 1550 cm^{-1}--is close to 1580 cm^{-1}, the E_{2g} mode frequency of graphite.

The E_{2g} mode frequency for graphite would be an asymptotic limit for E_{2g}-like mode frequencies of very large PAH molecules. The E_{2g}-like mode frequencies for linear PAH molecules approach but fall a little short of this limit, probably because of their linear, highly elongated structure. Analysis of the E_{2g}-like modes for more symmetrical, less elongated PAH molecules such as triphenylene (4 rings), coronene (7 rings), and hexabenzocoronene (13 rings) would most likely place an asymptotic limit (as the number of rings increases to infinity) at 1580 cm^{-1}.

We can conclude from Figure 11 that the isolated ring E_{2g} mode increases in frequency with added rings, and that a limit is reached with only about three rings. Therefore, complete ring mode-network coupling is achieved rapidly with relatively small ring assemblages. This result lends credence to the embedded ring approach, which attempts to account for the ring mode-network coupling analytically and without the use of numerical methods and large network simulations. Further analyses of this type are possible with the use of other vibrational modes (for example, the A_{1g} mode), other 6-membered carbon ring PAH molecules (for example, coronene), and with the use of PAH molecules containing 4-, 5-, and 7-membered rings.

CHAPTER IV

THE EMBEDDED RING APPROACH

Background

The vibrational properties of materials are determined to a large extent by the local arrangement of atoms.[2,14] This is especially significant for amorphous materials, which lack long-range order but display limited short-range order. As an example, the lattice vibrations of crystalline silicon, which exhibits a diamond-like cubic structure, rely primarily on the local four-fold coordinated tetrahedral structure of the silicon atoms. Many aspects of the dynamics of crystalline silicon can be derived from this local structure, in particular the general characteristics of the VDOS.[2] The local tetrahedral structure persists in amorphous silicon, with disorder appearing in the form of distributions of bond lengths and bond angles. By incorporating the effects of bond-length and bond-angle disorder in the VDOS, the dynamics of amorphous silicon have been extrapolated. The results agree fairly well qualitatively with the experimentally-determined VDOS of amorphous silicon.[2]

The use of short-range order (local atomic arrangement) provides an analytical approach for determining the vibrational dynamics of 3D amorphous solids. The technique can be applied to 2D amorphous materials as well once a basic, local structural unit is chosen. An immediate and obvious choice for a material such as amorphous carbon would be the three-coordinated, planar arrangement of four carbon atoms, forming a triangular cluster. However, such a basic unit could be arranged in groups to form rings of diverse sizes. The contribution of the ring modes of vibration to the VDOS would be significant, and yet such contributions would be neglected with the use of the triangular cluster as the basic unit.

The work of Galeener,[15-17] supports the use of rings as basic structural units for the analysis of amorphous solid dynamics, and indeed was the original inspiration for the research thrust of this thesis. Galeener examined Raman spectra of amorphous silica, and directed his attention to sharp features in the spectra. The sharp peaks are anomalies since vibrational spectra of amorphous materials generally yield broad features which usually blend into a continuum. The broadening of features is a consequence of disorder and relaxation or breakdown of Raman selection rules. The sharp peaks therefore present a contradiction to this general prescription.

Galeener's analysis revealed that the sharp features arise from the vibrational modes of SiO_2 rings of various sizes. The sharpness of the features can be attributed to vibrational decoupling of the rings from the surrounding atoms, effectively isolating the ring modes from the medium-range and long-range disorder. Galeener showed that vibrational decoupling of the rings is achieved by a cancellation of central forces with noncentral forces at the silicon atoms. With the motions of the silicon atoms canceled, the oxygen breathing modes of the SiO_2 rings are decoupled from the random network and result in the distinct features in the Raman spectra. Other silicate glass compositions display ring-mode decoupling as well, and Galeener's model remains as the best approach for these materials.[13,18]

Although nearly complete ring-mode decoupling will occur only for materials of certain compositions, the use of ring vibrational modes presents a fruitful approach for analytically determining the vibrational characteristics of amorphous materials. In particular, the use of various sized rings as basic structural units for amorphous 2D materials is especially promising. As mentioned previously, a 2D-CRN can be modeled as a collection of variously-sized rings, with ring statistics providing a method for characterizing the random network. In contrast to amorphous silica, the ring motions in an amorphous CRN material will, in general, be coupled to the collective motions of the network. The following sections will describe the analytical method I have developed for determining the ring vibrational modes and for incorporating ring-network coupling into the ring motions.

Structural Model for Embedded Ring Approach

A ring of atoms embedded in a 2D network can be regarded as a separate molecular entity, and methods used for determining molecular vibrations are directly amenable for determining the ring motions. The coupling of the ring to the network introduces the only modification required. For example, a 6-membered carbon ring in amorphous carbon can be described as a benzene ring embedded in a random network. The hydrogen bonds of the benzene molecule are then modified to represent the ring-network coupling, which results in a modification of the ring motions. The analogy has a good physical basis, since benzene, graphite, and amorphous carbon modeled as a 2D-CRN comprise the same type of carbon bonding (sp_2) and carbon-carbon bond lengths (1.39 Å for benzene,[58] 1.42 Å for graphite,[37] and 1.46 Å for amorphous carbon[44]). For the dynamics of our amorphous carbon model, the vibrational frequencies for 4-, 5-, 7-, and 8-membered carbon rings would be derived as well to account for the diverse ring sizes in the network.

The structural model for the embedded ring approach is constructed by cutting a circular hole into the random network. The edge of the hole is assumed to be rigid. An n-membered ring (n=4, 5, 6, 7, or 8) is then embedded in the hole (Figure 12). The bonds joining the atoms in the ring retain the normal force constants expected for carbon-carbon

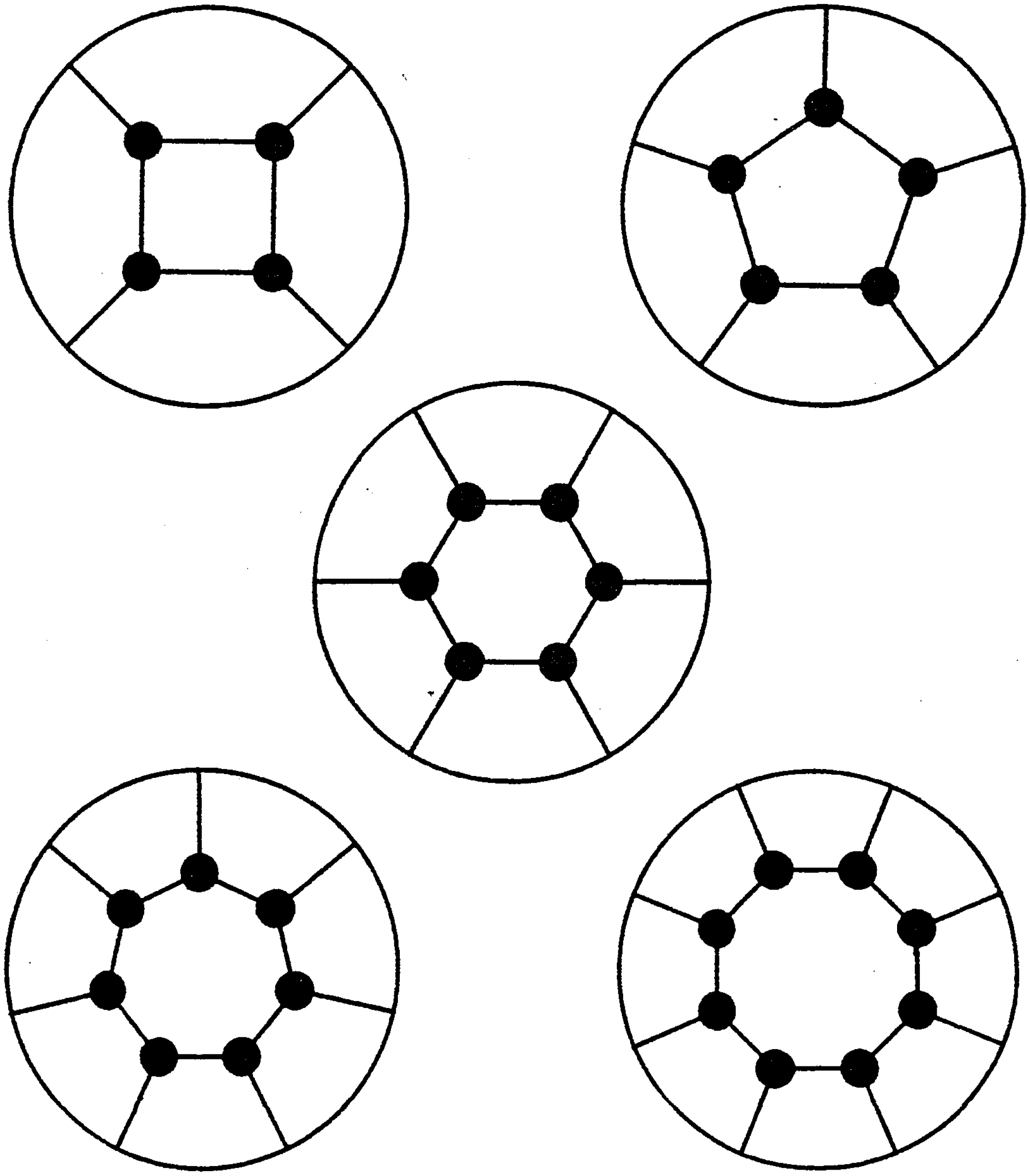

FIG. 12. Structural model for embedded ring approach with weighted coupling force constant.

bonding in the material. The bonds joining the ring atoms to the rigid wall, however, represent the coupling between the ring and the network. By constraining the edge of the hole to be rigid, the embedded ring approach attempts to account for the effects of the network's collective motions on the ring by weighing an effective coupling force constant. The effective coupling force constant then is not the normal atom-atom bond-stretching force constant, but a weighted force constant modified to reflect the random network's influence on the ring. The motions of the rings are then solved with the use of conventional techniques from classical mechanics described in following sections. Frequencies for the modes of oscillation for each n-membered ring are then extracted.

Note that a different approach is possible to account for the random network-ring coupling effects. By replacing the rigid wall of the hole with n peripheral atoms, the collective motions of the network can then be condensed into the n peripheral atoms by modifying their effective masses (Figure 13). The ring atoms retain their normal masses, and all of the force constants, including the coupling force constant, are now just the normal carbon-carbon force constants. The effective mass of the peripheral atoms would account for the entire random network, and reflect the network's effect on the ring motions. Solving the motions for an embedded 6-membered ring, for example, should be the

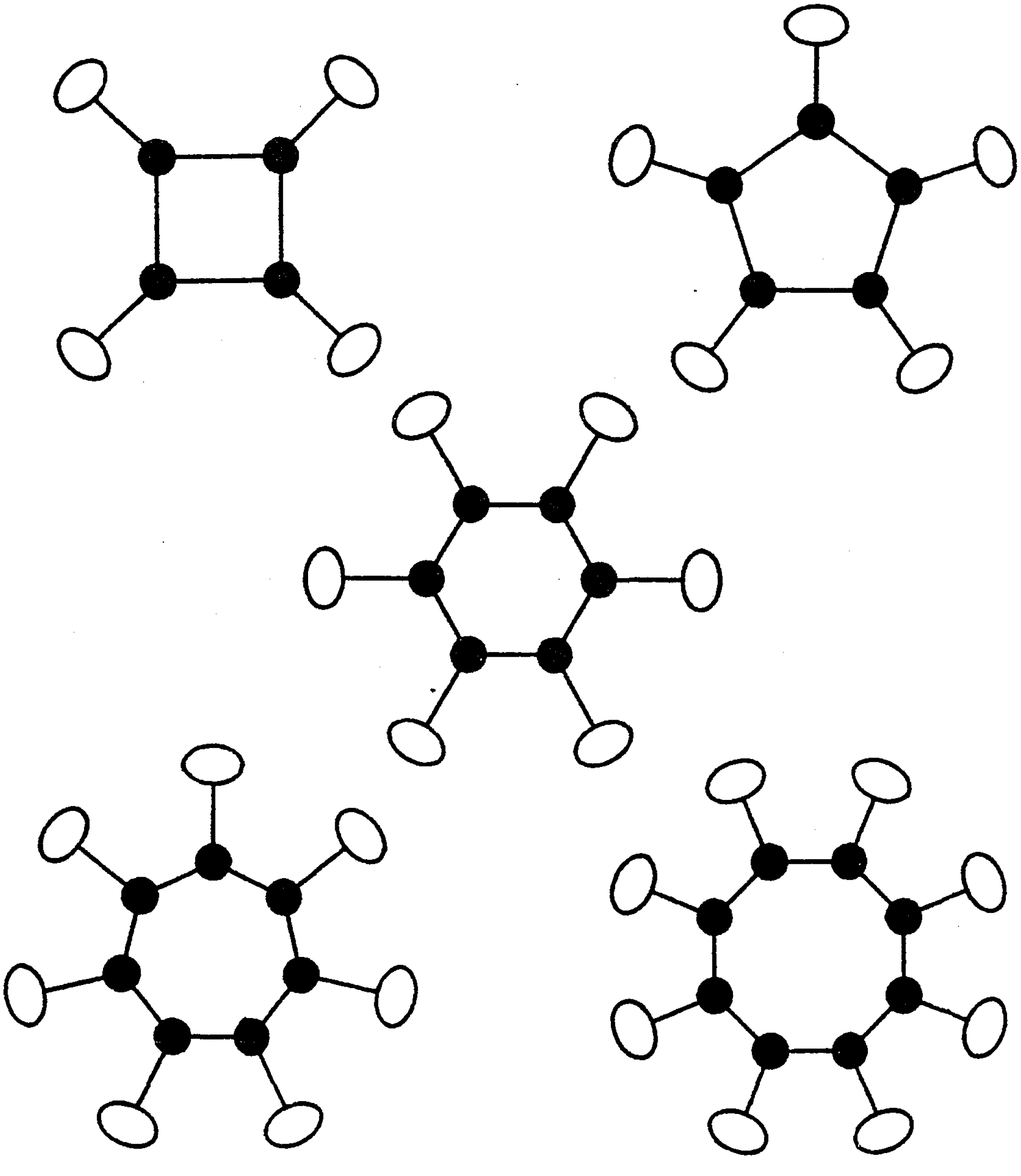

FIG. 13. Effective mass coupling embedded ring approach.

same as solving the motions for a benzene molecule, with only the hydrogen masses changed to effective masses and the hydrogen-carbon bonds changed to carbon-carbon bonds. Although a promising avenue of investigation, the mass-weighted, or effective mass coupling, embedded ring approach is beyond the scope of this thesis, which will confine itself to the force-constant weighted approach.

The methods used to determine the ring modes of vibration reflect the degree of approximation for the atomic potentials. My research makes use of two potential models: the central force model and the valence force model. For a first-order approximation, a central force model is employed, with only bond-stretching force constants and appropriate kinetic energy terms used in the calculations. The calculations are simple and straight-forward, requiring only the application of the method of small oscillations as presented by Goldstein.[59] The valence force model provides a second-order approximation, incorporating not only bond-stretching force constants, but also bond-angle-bending force constants. Angular kinetic energy terms are also included, and the number of internal coordinates required also increases. The complexity of the valence force model calculations necessitates the application of group theory. The utility of group theory goes beyond that of managing the calculations. It provides insights into the most probable modes of oscillation for the rings and shows the dependence of vibrational frequency on variations in bond length and force constants.

The valence force model in this work employs only nearest-neighbor interactions. Further refinements in the method of molecular vibrations are possible with the use of second and third nearest-neighbor interaction terms included into the potential function. The embedded ring approach, however, precludes the use of second and third nearest-neighbor interaction terms by imposing a rigid "wall" between the ring atoms and the random network. The wall isolates the ring atoms from many of their second and third nearest neighbors in the network. Many of the other methods employed by researchers studying vibrational dynamics of amorphous materials do not approach this level of refinement; several methods employ only a central force approximation.[2] Therefore, limiting the embedded ring approach to a simple valence force model with only nearest-neighbor interactions presents a justifiable approximation for amorphous materials.

Central Force Model

Calculations for the central force model employed the method of small oscillations as outlined by Goldstein.[59] The potential energy function incorporated only two bond stretching force constants, the atom-atom bond stretching force constant and the atom-rigid wall coupling force constant. Generalized coordinates for the atoms in the embedded ring assume the form

$$q_i = q_{0i} + \eta_i$$

where q_{oi} are the equilibrium atomic positions and η_i are deviations of the generalized coordinates from equilibrium. Expansion of the potential energy in a Taylor series about the equilibrium positions (q_{oi}) yields successive terms which are functions of the deviations (η_i). The small oscillation approximation retains only the terms in the series which are quadratic ($\eta_i \eta_j$), and the η_i's become new generalized coordinates. The kinetic energy terms are already quadratic functions of the velocities ($\dot{\eta}_i \dot{\eta}_j$).

The vibrational modes for the embedded ring are solved by assuming the ring is a system of coupled, linear harmonic oscillators. With our new generalized coordinates, the Lagrangian of the system is

$$\mathcal{L} = \frac{1}{2}(T_{ij}\dot{\eta}_i\dot{\eta}_j - V_{ij}\eta_i\eta_j)$$

Solution of Lagrange's equation yields a set of linear, homogeneous differential equations which are the equations of motion:

$$T_{ij}\ddot{\eta}_j + V_{ij}\eta_j = 0$$

The set of differential equations constitute an eigenvalue equation with oscillatory solutions of the form

$$\eta_i = Ca_i e^{-i\tilde{\omega} t}$$

where C is a scaling factor and a_i is the complex amplitude of oscillation for each coordinate η_i. The frequencies ($\tilde{\omega}$) for the vibrational modes can be solved by imposing the condition that the determinant comprised of the elements

$$V_{ij} - \tilde{\omega}^2 T_{ij}$$

must vanish. This determinant is the secular equation, and solution of the determinant yields a polynomial equation, the roots of which provide solutions for $\tilde{\omega}$ in terms of the constant coefficients for the potential energy (V_{ij}) and the kinetic energy (T_{ij}).

Cartesian coordinates were selected for the central force model approach, and are shown in Figure 14(a). Only in-plane vibrational modes were sought. Therefore, each atom was limited to only two degrees of freedom and only the x and y coordinates were necessary to describe the atom displacements. Each atom was given a set of coordinates (x_1,y_1 for the first atom; x_2,y_2 for the second atom; and so on) since only the displacements from equilibrium needed to be prescribed.

Determinants from the eigenvalue condition were constructed for 4-, 5-, 6-, 7-, and 8-membered embedded rings. The constant coefficients for the kinetic energy included only diagonal elements and were of the form

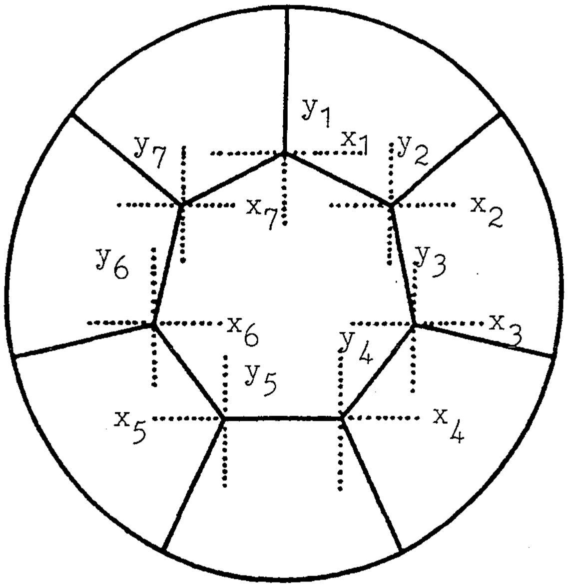

(a)

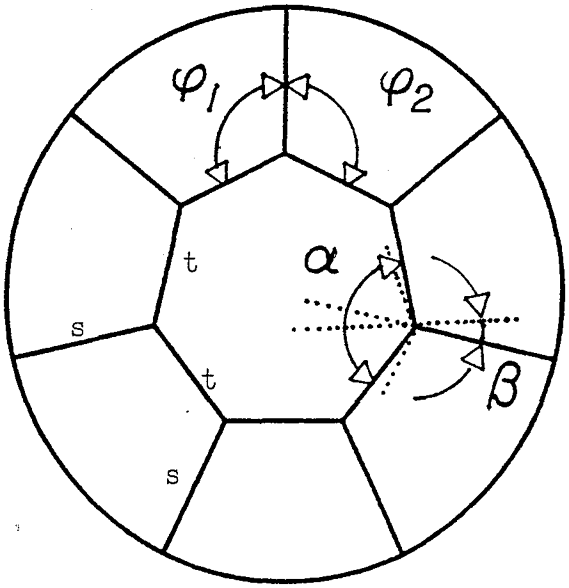

(b)

FIG. 14. Coordinate systems for central force model (a) and valence force model (b).

$$T_{ij}=m\delta_{ij}$$

where m is the mass of a carbon atom. The potential energy coefficients included both k_1, the bond stretching force constant, and k_2, the coupling force constant. The potential energy coefficients include nondiagonal elements since bond stretching between two atoms involves displacements of both atoms.

Because of the two degrees of freedom for each atom, the secular equation for an n-membered ring is a 2n x 2n determinant. The x_ix_j and y_iy_j elements in the secular equations separated into two identical blocks. All x_iy_j elements were zero, indicating the absence of cross-products between the x and y displacements. This separation of x and y coordinates allows the secular equation to be factored into two smaller n x n determinantal blocks.[60] Each n x n determinant can then be solved separately. Since the x-determinant and the y-determinant are identical, the secular equation for an n-membered ring becomes an n x n determinant.

Reduction of the 2n x 2n determinant to an n x n determinant introduces degeneracy into the eigenfrequency solutions. The 2n independent motions for the system (the embedded ring) arising from the two degrees of freedom for each atom will be necessarily degenerate due to the availability of only n eigenfrequencies. Further degeneracies occur in the solution of the n x n determinants, reducing the number of eigenfrequencies for each n-membered ring to less than n. The degeneracies exhibited by the vibrational modes of the embedded ring can be attributed to both the planar nature and the cyclical nature of the ring configuration.

Table 1 displays the n x n determinants for the 4-, 5-, 6-, 7-, and 8-membered embedded rings. The elements for all of the determinants are the same form($2k_1 + k_2 - \omega^2 m$, $-k_1$, and 0), and each determinant assumes a similar tri-diagonal form. Only the size (n) and placement of the elements varies between each determinant. The determinants were solved analytically using Derive©, a mathematical analysis program using symbolic algebra.[61] Solutions were in the form of n^{th}-order polynomials, with the polynomial roots providing expressions for the frequencies ω in terms of k_1, k_2, and m.

The ring motions for each eigenfrequency define the mode of oscillation, or vibrational species, associated with ω. Vibrational species were assigned to each eigenfrequency by substituting ω back into the eigenvalue equation. The amplitude coefficients were then determined for each atom in the embedded ring. The amplitude coefficients supply the relative displacement of each atom with respect to other atoms in the ring. The ring motions are easily obtained from the amplitudes of the relative displacements, and vibrational species are assigned to each mode of oscillation by examining the symmetry operations denoted by the displacements.

TABLE 1. Central force model matrices. The matrices are the factored secular determinants from the eigenvalue equation in cartesian coordinates.

$$\begin{vmatrix} a & b & 0 & b \\ b & a & b & 0 \\ 0 & b & a & b \\ b & 0 & b & a \end{vmatrix}$$

4-membered ring

$$\begin{vmatrix} a & b & 0 & 0 & b \\ b & a & b & 0 & 0 \\ 0 & b & a & b & 0 \\ 0 & 0 & b & a & b \\ b & 0 & 0 & b & a \end{vmatrix}$$

5-membered ring

$$\begin{vmatrix} a & b & 0 & 0 & 0 & b \\ b & a & b & 0 & 0 & 0 \\ 0 & b & a & b & 0 & 0 \\ 0 & 0 & b & a & b & 0 \\ 0 & 0 & 0 & b & a & b \\ b & 0 & 0 & 0 & b & a \end{vmatrix}$$

6-membered ring

$$\begin{vmatrix} a & b & 0 & 0 & 0 & 0 & b \\ b & a & b & 0 & 0 & 0 & 0 \\ 0 & b & a & b & 0 & 0 & 0 \\ 0 & 0 & b & a & b & 0 & 0 \\ 0 & 0 & 0 & b & a & b & 0 \\ 0 & 0 & 0 & 0 & b & a & b \\ b & 0 & 0 & 0 & 0 & b & a \end{vmatrix}$$

7-membered ring

$$\begin{vmatrix} a & b & 0 & 0 & 0 & 0 & 0 & b \\ b & a & 0 & 0 & 0 & 0 & 0 & 0 \\ 0 & b & a & b & 0 & 0 & 0 & 0 \\ 0 & 0 & b & a & b & 0 & 0 & 0 \\ 0 & 0 & 0 & b & a & b & 0 & 0 \\ 0 & 0 & 0 & 0 & b & a & b & 0 \\ 0 & 0 & 0 & 0 & 0 & b & a & b \\ b & 0 & 0 & 0 & 0 & 0 & b & a \end{vmatrix}$$

8-membered ring

$$a = 2k_1 + k_2 - \omega^2 m$$

$$b = -k_1$$

Valence Force Model

Inclusion of bond-angle-bending forces into the embedded ring approach introduces a higher level of approximation than presented by the central force model, but at the expense of quadrupling the complexity of the calculations. In addition to the two translational coordinates which account for translational displacements, two angular coordinates are now also required for each atom in the embedded ring to account for the bond angle bending. This increases the total number of coordinates for the n-membered embedded ring system from 2n to 4n. Additionally, coordinate cross-product terms which vanished in the central force model approach do not vanish in the valence force model approach. Consequently, the secular equation for an n-membered ring is now a 4n x 4n determinant, and not the n x n determinant resulting from the central force model. Finally, the kinetic energy matrix coefficients will be different for each n-membered ring since the bond angles differ for 4-, 5-, 6-, 7-, and 8-membered rings.

The application of group theory and the normal coordinate treatment to the embedded ring approach becomes essential when a valence force model is adopted. By approximating the configurations of the embedded rings with regular polygonal shapes, full advantage can be taken of symmetry elements and their corresponding symmetry operations. The symmetry elements of a ring allows classification of the ring to a molecular symmetry point group. Use of the point group's character table permits determination of vibrational species, fundamental modes, Raman active modes, and infrared active modes for the embedded ring.

The normal coordinate method utilizes the character table further by transforming the 4n internal coordinates to a set of symmetry, or normal, coordinates for each vibrational species. The symmetry coordinates are then used to establish a secular equation for each vibrational species. Each secular equation is either a 2 x 2 or 4 x 4 determinant, depending on the type of vibrational species (one, two, or three-dimensional representations). Note that the normal coordinate treatment factors the initial 4n x 4n secular equation into smaller (2 x 2 or 4 x 4) secular equations which are more readily solved.

The 4-, 5-, 6-, 7-, and 8-membered embedded rings were configured by placing the atoms at the vertices of a square, pentagon, hexagon, septagon, and octagon, respectively. The respective point groups for the rings are D_{4h}, D_{5h}, D_{6h}, D_{7h}, and D_{8h}, and were assigned by noting the number and type of symmetry axes and symmetry planes for each ring. For example, the 5-membered ring has one five-fold symmetry axis (C_5), five two-fold symmetry axes (C_2) perpendicular to C_5, and a symmetry plane (σ_h) also perpendicular to C_5. The C_2 symmetry axes with the C_5 symmetry axis define an additional set of five symmetry planes (σ_v) perpendicular to σ_h. The symmetry elements are completed with a rotation-reflection axis (S_5), and constitute the D_{5h} point group.

Each of the symmetry elements of a point group have corresponding symmetry operations. Each point group also has a set of vibrational species (also called representations) which are possible for the given point group. A specific atomic or molecular displacement occurs for a given vibrational species under a given symmetry operation. The character table of a point group tabulates these displacements for each vibrational species and each symmetry operation in the point group. By classifying the atomic displacements for a given vibrational species with respect to the symmetry operations, the character table facilitates calculation of fundamental, Raman active, and infrared active modes, and can be used to transform internal coordinates to symmetry coordinates.

Vibrational species for the embedded rings were obtained from the character tables of their corresponding point groups.[62,63] In-plane species were determined by noting the character of the species under the σ_h symmetry operation. A positive character denotes in-plane displacements while a negative character denotes out-of-plane displacements. Fundamental vibrations and Raman active fundamentals were acquired with the use of selection rules applied to each ring's character table. Ferraro and Ziomek [64] present the use of selection rules with clarity, and is highly recommended to the reader with a desire to pursue group theory. Table 2 lists the in-plane vibrational species, fundamentals, and Raman active fundamentals for the embedded rings.

Note that each atom has two degrees of freedom, and each embedded ring has 2n-3 in-plane vibrational degrees of freedom. Two degrees of freedom are subtracted for translation of the ring's center of mass, and one degree of freedom is subtracted for rigid rotation of the ring. This leaves 2n-3 in-plane vibrational degrees of freedom, or 2n-3 in-plane fundamentals for each ring. Table 2 displays this result, with five in-plane fundamentals for the 4-membered ring, seven in-plane fundamentals for the 5-membered ring, nine in-plane fundamentals for the 6-membered ring, eleven in- plane fundamentals for the 7-membered ring, and thirteen in-plane fundamentals for the 8-membered ring.

The Raman active modes include the A_{1g} or A_1' modes for all of the rings. These are the symmetrical breathing modes, and the displacements are similar for all five rings. The E_{2g} and E_2' Raman active modes also represent similar motions for all five rings. The ring motions for these modes stretch or elongate the ring along an in-plane symmetry axis (C_2), and these modes will most likely be present in networks experiencing longitudinal (compressional) oscillations with planar wavefronts.

The E_{2g} mode of the 6-membered ring was used as a basis for determining a consistent set of force constants since it

TABLE 2. Embedded ring vibrational species: In-plane, fundamental, and Raman active modes.

4-Membered Ring

In-Plane Modes: A_{1g}, A_{2g}, B_{1g}, B_{2g}, E_{1u}

Fundamentals: $\Gamma_{\text{in-plane}} = A_{1g} + B_{1g} + B_{2g} + E_{1u}$

Raman Active Modes: A_{1g}, B_{1g}, and B_{2g}

5-Membered Ring

In-Plane Modes: A_1' , A_2' , E_1' , E_2'

Fundamentals: $\Gamma_{\text{in-plane}} = A_1' + E_1' + 2E_2'$

Raman Active Modes: A_1' and E_2'

6-Membered Ring

In-Plane Modes: A_{1g}, A_{2g}, B_{1u}, B_{2u}, E_{1u}, E_{2g}

Fundamentals: $\Gamma_{\text{in-plane}} = A_{1g} + B_{1u} + B_{2u}$
$+ E_{1u} + 2E_{2g}$

Raman Active Modes: A_{1g} and E_{2g}

7-Membered Ring

In-Plane Modes: A_1' , A_2' , E_1' , E_2' , E_3'

Fundamentals: $\Gamma_{\text{in-plane}} = A_1' + E_1' + 2E_2' + 2E_3'$

Raman Active Modes: A_1' and E_2'

8-Membered Ring

In-Plane Modes: A_{1g}, A_{2g}, B_{1g}, B_{2g}, E_{1u}, E_{3u}, E_{2g}

Fundamentals: $\Gamma_{\text{in-plane}} = A_{1g} + B_{1g} + B_{2g}$
$+ E_{1u} + 2E_{3u} + 2E_{2g}$

Raman Active Modes: A_{1g} and E_{2g}

---

can be compared to the 1580 cm^{-1} line in the Raman spectrum of graphite. The coupling force constant is expected to be mode-dependent, assuming different values for different types of modes. A coupling force constant determined with the E_{2g} 6-membered ring mode should only be applicable to E-type modes. Therefore, only E-type modes for the 5- and 7-membered rings were analyzed further. The A_{1g}, B_{1g}, and B_{2g} modes for the 4-membered ring were also analyzed in addition to the E_{1u} mode because of the similarity of the ring motions to the E_{2g} 6-membered ring mode. Similarly, the B_{1g} and B_{2g} modes for the 8-membered ring were additionally examined along with the E_{1u}, E_{3u}, and E_{2g} modes. Because of breakdown of the Raman selection rules in amorphous materials, ring modes analyzed were not limited to only Raman active modes.

Establishment of a coordinate system for the various rings was the first step in calculating the frequencies for the selected modes. The internal coordinates selected for the valence force model were those used by Wilson et al.[60,65] in their vibrational analysis of the benzene molecule, and are displayed in Figure 14(b). The coordinates t and s are the atom-atom bond distance displacement and the atom-rigid wall bond distance displacement, respectively. The coordinates α and β are not the standard bond angle displacements $\Delta\phi_1$ and $\Delta\phi_2$, but are rather the change in the internal ring angle (α) and the angle between the internal ring angle bisector and the atom-rigid wall bond (β).

The potential energy matrix (f matrix) terms included only three force constants: the bond-stretching force constant (corresponding to the coordinate t), the coupling force constant (corresponding to the coordinate s), and the bond-angle-bending force constant (corresponding to the coordinates α and β). No interaction terms are included, and the resulting f matrix is diagonal in form, even after the transformation to symmetry coordinates.

Advanced methods of studying molecular vibrations replace the kinetic energy matrix with the g matrix.[60,64,66] The g matrix is more amenable to solution of the secular equation, and is related to the kinetic energy matrix by

$$2T=\sum_{i,j} g_{ij}p_i p_j$$

where p_i is the momentum conjugate to q_i, the i^th^ internal coordinate; p_j is the momentum conjugate to q_j, the j^th^ internal coordinate; the g_{ij}'s are the g matrix elements; and the summation is over both i and j. The g matrix elements for the embedded rings were determined with the use of the vector method described by Wilson et al.[60] Atomic masses, bond angles, and bond distances are used to construct the g matrix elements. To use the vector method, each bond was required to terminate at an atom with a given mass. A hypothetical atom was therefore placed at the outer end of the coupling bond since no atom existed there in the structural model for the embedded ring. Since the coupling bond terminates at a rigid wall, the mass of the hypothetical atom was taken to be infinite. (The infinite mass fixes the end of the coupling bond to a stationary point.) This presented no difficulty in the g matrix elements because only the reciprocal of the masses appear. Some of the terms in the g matrix elements consequently vanished.

Because of the nonstandard nature of the α and ß coordinates, the g matrix element tables given by Wilson et al. could not be used to construct g matrix elements for the embedded rings. Use of the tables yielded erroneous results. The g matrix elements constructed for the 6-membered embedded ring were compared with those calculated for benzene by Wilson et al. to ensure proper implementation of the vector method.

Symmetry coordinates for each vibrational species were prepared by first transforming the internal coordinates under the symmetry operations of each of the five point groups. The characters in the character tables for each vibrational species were then used to determine the correct combination of transformed internal coordinates for each symmetry coordinate. Finally, the symmetry coordinates were normalized.

The value of the symmetry coordinates lies in their ability to transform the f and g matrices into factored potential energy and kinetic energy matrices (the F and G matrices). These factored matrices allow partitioning of the original 4n x 4n secular equation or determinant into smaller 2 x 2 and 4 x 4 secular determinants, each corresponding to a particular vibrational species.

The symmetry coordinates are related to the internal coordinates by the transformation

$$Q_j=\sum_k U_{jk}q_k$$

where Q_j is the j^{th} symmetry coordinate, q_k is the k^{th} internal coordinate, and the summation is over k. The U matrix can be used to transform not only the internal coordinates, but also the f and g matrices as well. The F and G matrices are obtained from the following transformations, given in matrix notation:

$$F=UfU^t$$

$$G=UgU^t$$

U^t is the transpose of U. Final solution for the vibrational mode frequencies follows from solving the secular equation

$$|GF-I\omega^2|=0$$

where I is the identity matrix.

The procedure outlined in the previous paragraphs was performed for each of the selected vibrational species for the five embedded rings. Transformation of the f matrix yielded diagonal F matrices with the force constants as the diagonal elements. Transformation of the g matrix yielded G matrices with elements comprised of linear combinations of g matrix elements. Since the bond angles were already calculated into the g matrix elements, only the atom mass m and the bond lengths t and s remained as explicit variables in the G matrix. Since amorphous carbon was used as the test case for the embedded ring approach, m was given a value of 12 amu (1.992 x 10^{-23} g), the mass of the carbon atom. The bond lengths s and t were just the nearest neighbor atom-atom distance in amorphous carbon, which has been reported with values of 1.46 Å,[44] 1.48 Å,[67] 1.49 Å,[43] and 1.43 Å.[40] A value of 1.46 Å was selected for s and t, and is intermediate in the range of values reported.

The 2 x 2 and 4 x 4 secular determinants were solved with the use of Derive©, a symbolic algebra program.[61] The roots of the resulting polynomials were also obtained using Derive©, and provided frequencies for the vibrational modes of the embedded rings. The polynomials had very large coefficients which hampered solution even with a computer. Since the units of measure for the coefficients were even powers of Hz (Hz^2, Hz^4, etc.), scaling the coefficients to terahertz frequencies resolved this difficulty in solving for the roots.

CHAPTER V

RESULTS

Force Constant Models for Carbon

Solution of both the central force model and valence force model required selection of a set of force constants which would approximate the sp_2 bonding forces in graphite and a-C. Only the bond-stretching force constant was necessary for the central force model. The valence force model required an additional bond-angle-bending force constant. Only nearest neighbor force constants were considered since interaction terms were neglected for both models. Force constant fitting with the 1580 cm^{-1} E_{2g} mode in graphite and analysis of network motions adjacent to the embedded ring determined the coupling force constant for each model.

The literature on the vibrational dynamics of a-C and graphite present a wide range of values for the bond-stretching and bond-angle-bending force constants. Table 3 lists the values reported by researchers in the field. Values given by Beeman et al.[40], Al-Jishi and Dresselhaus,[68] Tuinstra and Koenig,[51] Young and Koppel,[69] and Nicklow et al.[70] were determined by fitting dynamical models to spectral features of graphite. Kesavasamy and Krishnamurthy[11] cite an empirical relationship between interatomic distances and bonding forces for their value for the bond-stretching force

TABLE 3. Force constant models for carbon. Values are the nearest neighbor force constants in N/m for graphite and sp_2-bonded amorphous carbon.

Source	Bond-Stretching Force Constant (f_b)	Bond-Angle-Bending Force Constant (f_a)
Beeman et al.[26]	363	36
Nicklow et al.[57]	362	199
Al-Jishi and Dresselhaus [55]	313	267
Young and Koppel [56]	436	36
Tuinstra and Koenig [34]	432	25
Kesavasamy and Krishnamurthy [11]	459	*
Average	394	113
Standard Deviation	51.6	101

* No bond-angle-bending force constant given.

constant: their method did not employ a bond-angle bending force constant. Note that the values reported for the bond-stretching force constant vary by more than 20% from the average value of 394 N/m, and the values of the bond-angle-bending force constant span more than an order of magnitude.

A bond-stretching force constant of 363 N/m was initially selected for both the central force model and valence force model. The success of Beeman _et_ _al_. in modeling spectral features of a-C was the primary reason for the selection. Additionally, the value of 363 N/m lies close to the value of 362 N/m given by Nicklow _et_ _al_., and is also intermediate in the range of high and low values reported (313 N/m to 459 N/m).

With 363 N/m as the bond-stretching force constant, calculation of the 1580 cm^{-1} E_{2g} mode in graphite with the central force model produced a coupling force constant of 315 N/m. Use of these force constants with the central force model constitutes central force model one (CFM1), and mode frequencies for all five rings were calculated with this model.

The coupling force constant was assumed, on the basis of physical intuition, to be positive and within an order of magnitude of the bond-stretching force constant. Although close in value to the bond-stretching force constant and therefore an apparently realistic result, a coupling force constant of 315 N/m may be too low to accurately represent the ring-network coupling for an E_{2g} mode. In the 6-membered ring E_{2g} mode, the network atoms adjacent to the embedded ring move in direct opposition to the ring atoms. Each network atom moves with the same displacement but in opposite direction to the embedded ring atom it is coupled with. By replacing the network atom with a rigid wall, the effect of the opposing motions of the network atoms can be accommodated by doubling the force constant of the coupling bond.

The above scenario is analogous to the problem of two masses joined by a spring. The two mass-spring system, Figure 15(a), oscillates with a frequency of

$$\omega=\sqrt{\frac{2k}{m}}$$

and the two masses move in opposite directions. Replacement of one of the masses with a rigid wall, Figure 15(b), results in a system which oscillates at a frequency of

$$\omega=\sqrt{\frac{k'}{m}}$$

where k' is the force constant of the spring in the new system. To oscillate at the same frequency as the two mass-spring system, the force constant k' must be equal to $2k$. In the embedded ring system, k corresponds to k_1, the bond-stretching force constant, and k' corresponds to k_2, the coupling force constant. Therefore, to accurately accommodate the effect of the network motions on the embedded

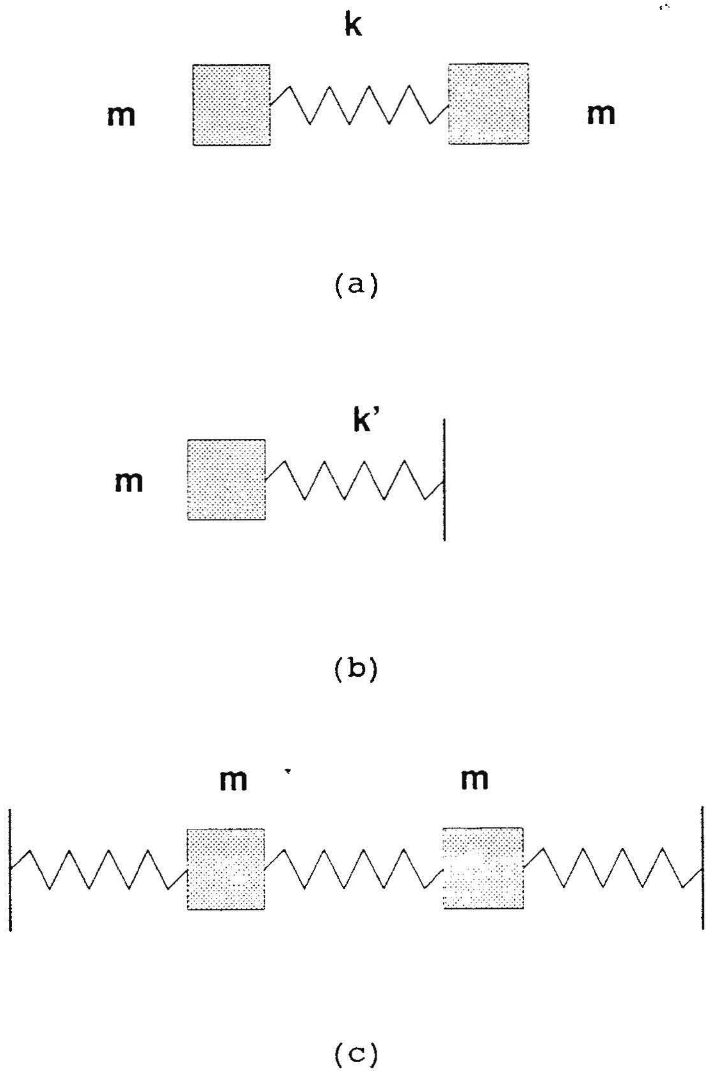

FIG. 15. Two mass-spring system (a), rigid wall-mass-spring system (b), and embedded mass-spring system (c) used to illustrate the coupling force constant and loss of degeneracy in the embedded ring system.

ring, the coupling force constant must be approximately equal to twice the bond-stretching force constant:

$$k_2 \approx 2k_1$$

By imposing the condition $k_2 = 2k_1$, analysis of the 1580 cm^{-1} E_{2g} 6-membered ring mode determined the force constants to be $k_1 = 295$ N/m and $k_2 = 589$ N/m. Use of these force constants with the central force model constituted central force model two (CFM2), and mode frequencies for all five rings were calculated with this model. Note that a value of 295 N/m for the bond-stretching force constant is not unreasonable, being only 6% off from the value of 313 N/m reported by Al-Jishi and Dresselhaus.

Calculation of the 1580 cm^{-1} E_{2g} mode in graphite with the valence force model imposed an algebraic relationship between the three force constants. This algebraic relationship represented a boundary condition for the force constants, and was used to determine a set of values for the force constants consistent with a 1580 cm^{-1} E_{2g} mode for an embedded 6-membered ring. Use of any of the bond-angle-bending force constants in Table 3 yielded unrealistic and nonphysical values for either the bond-stretching force constant or coupling force constant. A force constant value was considered unrealistic if it exceeded 1000 N/m or was negative. Establishing a bond-stretching force constant of 363 N/m narrowed the allowable range of the bond-angle-bending force constant to 80-110 N/m. By further setting the coupling force constant at 726 N/m (that is, twice the bond-stretching force constant), a bond-angle-bending force constant of 80 N/m was determined.

Note that a value of 80 N/m for the bond-angle-bending force constant lies intermediate in the range of values reported in Table 3. That the valence force model yielded a realistic value for the bond-angle-bending force constant as a first result was promising.

As a consequence of the 1580 cm^{-1} E_{2g} mode analysis, the force constants for the valence force model (VFM) were determined to be

$$f_a = 80 \text{ N/m}$$

$$f_b = 363 \text{ N/m}$$

$$f_c = 726 \text{ N/m}$$

where f_a is the bond-angle-bending force constant, f_b is the bond-stretching force constant, and f_c is the coupling force constant.

Central Force Model Results

Table 4 presents the results of CFM1. All five sizes of rings displayed a low frequency mode at 667 cm^{-1}, corresponding to rigid ring translation (or translation of the ring's center of mass) within the hole. The rigid ring

TABLE 4. Results of central force model one. Force constants were $k_1 = 363$ N/m, $k_2 = 315$ N/m. Frequencies are given in cm^{-1} and modes are in parentheses.

Ring Size (n)	Frequency				
	A Modes	B Modes	E_1 Modes	E_2 Modes	E_3 Modes
4	1213 (A_{1g})	1213 (B_{1g}, B_{2g})	1580 (E_{1u})		
5	1074 (A_1')			1517 (E_2')	
6	979 (A_{1g})	1408 (B_{1u}, B_{2u})		1580 (E_{2g})	
7	912 (A_1')		1303 (E_1')	1548 (E_2')	
8	863 (A_{1g})	1482 (B_{1g}, B_{2g})	1213 (E_{1u})		1580 (E_{3u})

translation frequency was omitted from Table 4 since it was not a fundamental vibrational species.

The remaining results of CFM1, Table 4, represent frequencies for fundamental vibrational species/modes of the five ring sizes. Degeneracy in frequency between different modes occurs for the 4-membered ring (A_{1g}, B_{1g}, and B_{2g} modes), 6-membered ring (B_{1u} and B_{2u} modes), and 8-membered ring (B_{1g} and B_{2g} modes). The E_{1u} mode of the 4-membered ring, E_{2g} mode of the 6-membered ring, and E_{3u} mode of the 8-membered ring display accidental degeneracy at 1580 cm^{-1}. Modes that are absent in the analysis are the E_1' mode for the 5-membered ring, the E_{1u} mode for the 6-membered ring, the E_3' mode for the 7-membered ring, and the E_{2g} mode for the 8-membered ring. Their absence was not intentional since the secular determinants were not factored by vibrational species, and their absence can be attributed to either degeneracy with other E-type modes or to the coarseness of the potential approximation used.

Table 5 presents the calculated frequencies for CFM2. All five rings displayed a low frequency mode at 912 cm^{-1}, again corresponding to rigid ring translation (and therefore not included in Table 5). The calculated frequencies for CFM2 display the same degeneracies and absent modes as those for CFM1. Note that the change in force constants results in higher frequencies for the modes in CFM2 (as compared to CFM1), except for the E_{2g} mode of the 6-membered ring and the

TABLE 5. Results of central force model two. Force constants were k_1 = 295 N/m, k_2 = 589 N/m. Frequencies are given in cm^{-1} and modes are in parentheses.

Ring Size (n)	Frequency				
	A Modes	B Modes	E_1 Modes	E_2 Modes	E_3 Modes
4	1291 (A_{1g})	1291 (B_{1g}, B_{2g})	1581 (E_{1u})		
5	1187 (A_1')			1530 (E_2')	
6	1118 (A_{1g})	1443 (B_{1u}, B_{2u})		1581 (E_{2g})	
7	1071 (A_1')		1361 (E_1')	1555 (E_2')	
8	1038 (A_{1g})	1502 (B_{1g}, B_{2g})	1291 (E_{1u})		1581 (E_{3u})

accidentally degenerate modes for the 4- and 8-membered rings. The difference in frequency for each mode between the two central force models is more pronounced for low frequency modes. Higher frequency modes display less variation with the change in force constants.

Valence Force Model Results

In contrast to the central force model, the valence force model produces neither accidental degeneracies nor degeneracy between modes for a given ring. This loss of degeneracy can be attributed to an improved potential approximation for the VFM. In fact, implementation of the VFM to the embedded ring system removes degeneracies that would normally be present for the vibrational species. The normally singly degenerate species A_{1g}, B_{1g}, and B_{2g} are represented by 2 x 2 secular determinants which yield a single, degenerate eigenfrequency. The doubly degenerate E-type modes are represented by 4 x 4 secular determinants, and normally yield two degenerate eigenfrequencies.

The A and B-type modes in the VFM resulted in secular determinants with two nondegenerate roots. The E-type modes had secular determinants with four nondegenerate roots. The task remained to explain and accommodate this loss of degeneracy.

The loss of degeneracy for each of the vibrational modes can be attributed to the embedding of an isolated ring into a network (or, alternatively, the effect of coupling an isolated ring to the wall of a rigid hole). Again, we can use the two mass-spring system as an analogy to explain this loss of degeneracy. An isolated two mass-spring system, Figure 15(a), oscillates with a single frequency; its 2 x 2 secular determinant is singly degenerate. The two mass-spring system can be embedded by placing it between two rigid walls, and by attaching each mass to a wall with a spring having a force constant different from that of the spring holding the two masses together. The resulting mass-spring-wall system, Figure 15(c), gives rise to two modes of oscillation, with each mode having a distinct frequency. In analytical terms, the 2 x 2 secular determinant for the system is no longer degenerate, and its solution presents two distinct roots from which the eigenfrequencies derive.

In exactly the same fashion, the vibrational modes of an embedded ring lose their degeneracy due to the coupling of the ring with the network. Since the loss of degeneracy can be explained on a physical basis, the nondegenerate eigenfrequencies may also have a physical basis. The vibrational dynamics of polycyclic aromatic hydrocarbons support this contention. The coupling of 6-membered carbon rings to benzene increases the number of vibrational modes and frequencies for the molecule. Such an effect can be observed with triphenylene, which exhibits an inordinately large number of E-type mode frequencies in comparison to benzene.[71]

Although the increase in mode frequencies can be attributed to an increase in the number of atoms in the molecule, the underlying symmetry of both the molecule and the particular vibrational species limits the number of possible vibrational species. In some cases, the loss of degeneracy in a vibrational mode reflects the appearance of new vibrational modes due to a lowering of symmetry or an increase of the atomic basis for the molecule.

If the embedded ring was part of a crystal lattice, such as a 6-membered ring in graphite, it can be argued that translational symmetry within the lattice would remove some of the nondegenerate frequencies and restore degeneracy to the vibrational modes. An amorphous material, however, lacks the translational symmetry necessary to restore degeneracy. We would then expect the nondegenerate mode frequencies to be present in the random network and to contribute to the vibrational density of states. This provides a possible explanation for the increase in the number of contributing frequencies in the VDOS for amorphous materials. (From a crystallographic viewpoint, an amorphous material can be said to have a unit cell of infinite dimensions, and therefore the atomic basis for the unit cell would also be infinite. From a molecular viewpoint, a covalently bonded amorphous material can be said to be a single molecule of infinite size. From either view, such a structure intuitively would give rise to a continuum of vibrational modes.)

Table 6 tabulates the frequencies calculated with the VFM for selected vibrational modes of the five embedded rings. All of the secular determinants for the vibrational modes were nondegenerate. However, not all of the nondegenerate frequencies are given in Table 6 for each mode. The frequencies not presented were either very low (< 13 cm^{-1}) or imaginary (negative root in the polynomial solution for the secular determinant). All of the E-type modes had two nondegenerate frequencies which were close to 0 cm^{-1}, indicating that the secular determinants were nearly singly degenerate. The remaining two nondegenerate frequencies are presented for each E-type mode.

Comparison of Force Model Results

Results from CFM1 and CFM2 were cursorily compared in a previous section of this chapter. As was noted, high frequency modes were more insensitive to the change in force constants than the low frequency modes. Except for the B_{1g}, B_{2g} modes for the 8-membered ring and B_{1u}, B_{2u} modes for the 6-membered ring, the high frequency modes are generally E-type modes.

Table 7 compares selected mode frequencies for CFM1, CFM2, and the VFM. Frequencies displayed for the VFM are the highest nondegenerate frequency for each given mode. Two observations can be extracted from Table 7. First, in

TABLE 6. Results of valence force model. Frequencies are given in cm^{-1}. Force constants used were f_a = 80 N/m, f_b = 363 N/m, and f_c = 726 N/m. Modes are in parentheses.

Ring Size (n)	Frequency				
	(A_{1g})	(B_{1g},B_{2g})	(E_{1u},E_1')	(E_{2g},E_2')	(E_{3u},E_3')
4	717 1241 (A_{1g})	1390 (B_{1g}) 1068 (B_{2g})	702 1550 (E_{1u})		
5			696 1475 (E_1')	1040 1555 (E_2')	
6	1241 (A_{1g})			950 1581 (E_{2g})	
7			666 1304 (E_1')	883 1529 (E_2')	1250 1598 (E_3')
8		1546 (B_{1g}) 1368 (B_{2g})	648 1243 (E_{1u})	835 1457 (E_{2g})	1163 1601 (E_{3u})

TABLE 7. Comparison of selected modes for central force model one (CFM1), central force model two (CFM2), and the valence force model (VFM). Frequencies given in cm^{-1}.

Ring Size (n) and Mode	CFM1	CFM2	VFM
4-n A_{1g}	1213	1291	1241
4-n B_{1g}	1213	1291	1390
4-n B_{2g}	1213	1291	1068
4-n E_{1u}	1580	1581	1550
5-n E_2'	1517	1530	1555
6-n A_{1g}	979	1118	1241
7-n E_1'	1303	1361	1304
7-n E_2'	1548	1555	1529
8-n B_{1g}	1482	1502	1546
8-n B_{2g}	1482	1502	1368
8-n E_{1u}	1213	1291	1243
8-n E_{3u}	1580	1581	1601

general, all of the frequencies show fair agreement between the different force models for each mode, indicating that the central force model approximation is fairly good when compared to the valence force model. Second, mode frequencies for the E-type modes tend to be more consistent between models than mode frequencies for A- and B-type modes.

The second result may be due to the generally higher frequencies of the E-type modes. However, the frequencies of the A- and B-type modes for the 4- and 8-membered rings are higher than the frequency of the 8-membered ring E_{1u} mode, contradicting this assessment. A more likely explanation is that the E-type modes are more accurately represented with a coupling force constant having a value between the bond-stretching force constant and twice the bond-stretching force constant ($k_1 \leq k_2 \leq 2k_1$, or $f_b \leq f_c \leq 2f_b$).

A cursory examination of ring mode motions with respect to network atom motions concludes that A_{1g} and B_{1g} modes are more accurately modeled with the above value range for the coupling force constant than the B_{2g} mode. Comparison between the different force models for the A_{1g}, B_{1g}, and B_{2g} modes of the 4-membered ring and the B_{1g} and B_{2g} modes of the 8-membered ring support this conclusion.

CHAPTER IV

DISCUSSION

Application to Amorphous Carbon

The two-dimensional and covalent aspects of sp_2 bonding in graphite and graphitic amorphous carbon have led researchers to postulate and look for the existence of 2D continuous random networks in a-C. The presence of a small percentage of sp_3 bonds in a-C (0-10%) would result only in warping and distorting the 2D layers. Establishing the presence of 5- and 7-membered rings (and possibly 4- and 8-membered rings as well) at significant levels (>10%) in the structure of a-C would evidence an absence of local, graphitelike hexagonal structure. Researchers have attempted this with various modeling approaches [40,43,67] and experiments,[41,42,44] and with particular emphasis on vibrational spectra of a-C.

Amorphous carbon was chosen as an initial application to test the accuracy of the embedded ring approach because of amorphous carbon's postulated CRN structure and local 2D characteristics. Additionally, the problem of the atomic structure of a-C has yet to be definitively resolved. Success of the embedded ring approach would provide additional evidence in support of a CRN model for a-C.

Success of any dynamical model for a material is measured by its ability to predict spectral features in the

VDOS, Raman, or infrared spectra of the material. For a-C, the Raman spectrum is more accessible than the VDOS or infrared spectra because it is most easily acquired (as compared to, for example, inelastic neutron scattering). The Raman spectrum also provides distinguishing spectral features not found in the infrared spectrum. The results of the embedded ring approach were therefore compared to a Raman spectrum of a-C. The comparisons favor a CRN model for a-C by indicating the presence of 5- and 7-membered ring mode frequencies in the Raman spectrum, with the 5- and 7-membered rings comprising a large portion of the ring statistics in comparison to 6-membered rings. The presence of a large percentage of 4- and 8-membered rings in the CRN can be excluded, however, as a result of the comparisons.

Discrete Line Spectra

The mode frequencies calculated for a-C using the three force models (CFM1, CFM2, and VFM) fall within the region consistent with internal mode frequencies for crystalline and amorphous solids (0-2000 cm^{-1}). Figure 16 displays discrete line spectra of the mode frequencies calculated with CFM1 (Figure 16[a]), CFM2 (Figure 16[b]), and the VFM (Figure 16[c]) which are tabulated in Tables 4, 5, and 6. Note the predominance of E-type mode frequencies in the 1000-1600 cm^{-1} region, a region coincident with the dominant spectral feature in Raman spectra of a-C (see Figure 9[c]). Since the

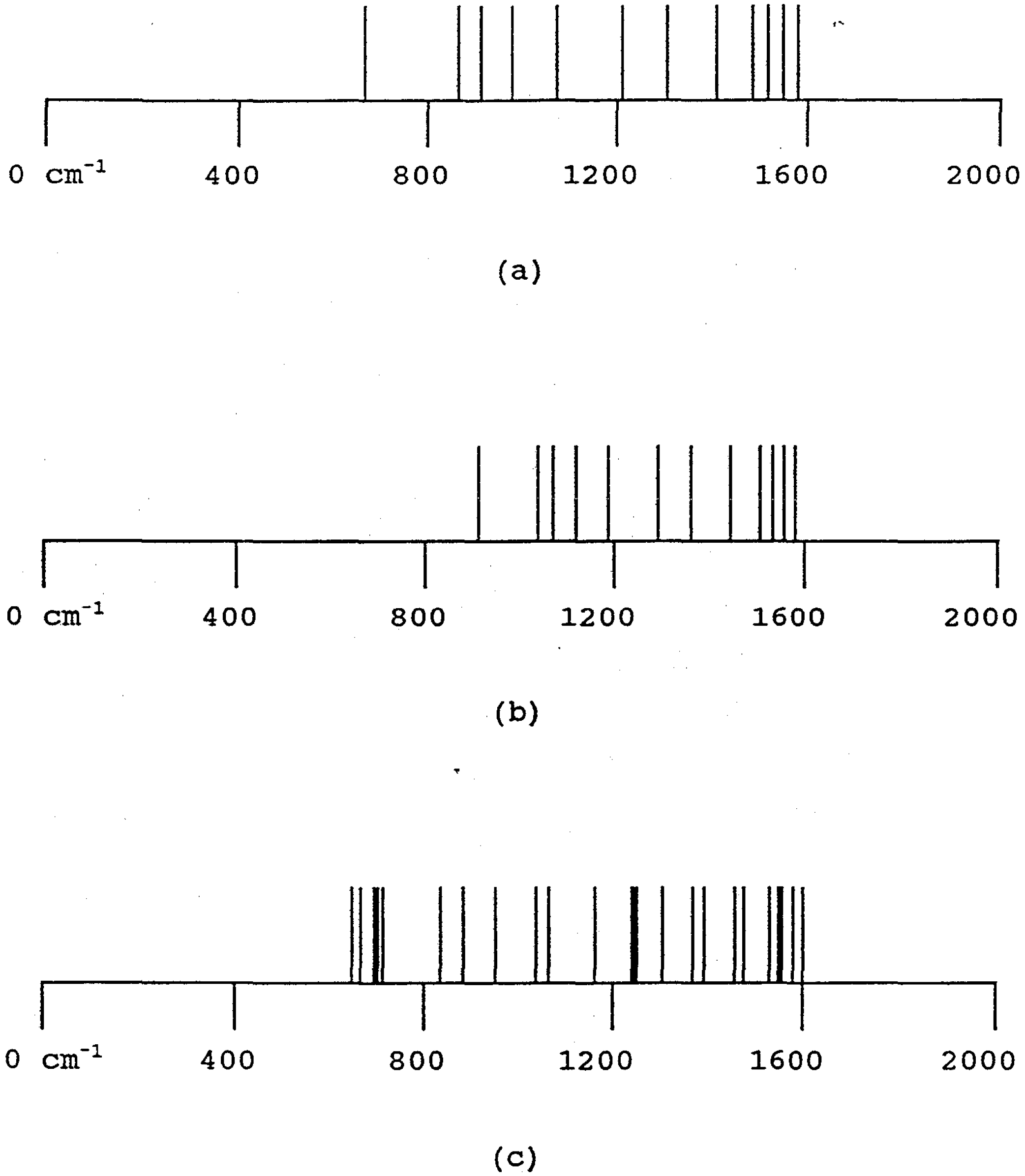

FIG. 16. Discrete line spectra of embedded ring frequencies for (a) central force model one (CFM1), (b) central force model two (CFM2), and (c) the valence force model (VFM).

VFM uses an improved approximation to the potential in comparison to the central force models, mode frequencies calculated with the VFM were singled out for comparison studies with actual spectra. Only the highest, nondegenerate frequency for each mode was used because of their correspondence to CFM-generated frequencies, and because the highest frequencies resided in the 1000-1600 cm^{-1} region.

Because of the selection of the coupling force constant, E-type mode frequencies were taken as having the most accurate values, and were therefore used for comparison with the Raman spectrum of a-C. As previously discussed in Chapter V, the E-type mode frequencies are more consistent between the three force models used than the A- and B-type mode frequencies. This consistency is attributed to assigning values to the coupling force constant which most accurately represent network motions congruent to E-type ring mode motions. Note that the 6-membered ring A_{1g} mode frequency calculated with the VFM (1241 cm^{-1}) deviates 10% from the measured value (1360 cm^{-1}). Calculations of the A_{1g} mode frequency with CFM1 and CFM2 show even greater deviation. Finally, analysis of network atom-ring atom motions for the B_{2g} mode disagree with the selected value for the coupling force constant; network-ring motions for a B_{2g} mode for a 4- or 8-membered ring would yield a coupling force constant with a value significantly less than that of the bond-stretching force constant.

Theoretical Spectra with Gaussian Peak Profiles

The Raman spectrum of amorphous carbon (Figure 9[c]) displays few maxima, and most closely resembles a single broad, asymmetrical peak. However, the asymmetry of the a-C peak is incongruous with the Lorentzian and gaussian profiles typically exhibited by Raman lines. A method for analyzing the Raman spectrum of a-C is suggested from Raman spectral studies of water- and fluorine-bearing silica glasses.[72] Raman spectra of the silica glasses displayed broad, asymmetrical spectral features. The spectral features were deconvoluted into groups of overlapping Lorentzian or gaussian peaks. The fit of deconvoluted spectra with experimental spectra were compared with a chi-squared error analysis and a plot of the residuals. The error analysis determined that the experimental spectra were modeled best with gaussian peak profiles.

Although suggestive of a continuum from 1000 to 1600 cm^{-1} with clustering of E-type modes near the maximum of the a-C peak, the discrete line spectrum of VFM mode frequencies cannot be used solely to explain the Raman spectrum of a-C. Rather, in a vein similar to deconvolution of amorphous silica spectra, the calculated VFM mode frequencies were broadened with gaussian peaks and convoluted into theoretical spectra. The theoretical spectra were then compared with the experimental Raman spectrum of a-C.

Theoretical spectra were obtained from the VFM mode frequencies with the use of MathCAD©, a numerical analysis program.[73] Gaussian peak profiles were selected for convolution based on the research with amorphous silica spectra.[72] Note that, as an analogy, gaussian profiles typically reflect inhomogeneous broadening in stimulated emissions from laser materials (also thermal broadening in gas lasers), whereas Lorentzian profiles are associated with homogeneous broadening (such as intrinsic lifetime broadening due to a metastable state). Structural disorder in a laser material, such as in a Nd-glass laser, results in a laser emission with a gaussian spectral shape.

Integrated peak intensities were assumed to be directly proportional to the ring statistics. That is, the integrated peak intensity for each n-membered ring mode frequency corresponded to the percentage of n-membered rings in the CRN. Integrated peak intensity was chosen instead of peak height to be proportional to the ring statistics since a single gaussian peak represents a pseudo density-of-states for a single vibrational mode. (The peak can be said to comprise a distribution of frequencies about the mode's center frequency.)

Model ring statistics were taken from two a-C models by Beeman et al.[40] The two Beeman models were graphitic in nature, having no sp_3 bonded atoms in one model and 9.1% sp_3 bonded atoms in the other. Both random network models contained significant percentages of 5- and 7-membered rings, but no 4- and 8-membered rings.

The gaussian peak positions were fixed in the numerical analysis to the VFM mode frequencies. The variables were the number and type of modes used, the standard deviation (σ) of the gaussian peak widths (noting that the full width at half maximum FWHM = $2\sigma[2\ln 2]^{\frac{1}{2}}$), and the ring statistics. A chi-squared statistical analysis provided quantitative comparison between the different fits. To perform the chi-squared analysis, Raman data from the experimental a-C spectrum (Figure 9[c]) were tabulated and entered into the convolution program. A slightly sloping, linear background, most likely arising from a weak fluorescence in the sample, was subtracted from the Raman data. The theoretical spectrum was scaled to the experimental spectrum with the use of either the total integrated peak intensities or the peak maxima.

In accord with the approach of Beeman et al., vibrational modes for 5-, 6-, and 7-membered rings were emphasized in the spectral fits due to the expected predominance of these rings in the structure of a-C. Also, following a previous argument presented in this section, the spectral fits were modeled with E-type modes because of their presence in the 1000-1600 cm^{-1} region. The Raman active E_2' and E_{2g} modes were additionally included in every spectral fit since the fits were modeling the Raman spectrum of a-C.

Peak widths were selected and varied to provide the best fit for the given ring statistics and mode frequencies for each spectral fit. The peak widths were initially expected to exceed those found in Raman spectra of water- and fluorine-bearing silica glasses (σ=20-50 cm^{-1}), and were given in most fits an initial width of σ=100 cm^{-1}. Varying the ring statistics and type of vibrational modes present, both before and after adjusting the peak widths, provided an iterative approach to achieving the best spectral fits.

The A_{1g} mode for the 6-membered ring was included in some of the spectral fits on the basis of its occurrence in Raman spectra of nanocrystalline graphite. The 5-membered ring E_1' mode and 7-membered ring E_1' and E_3' modes were also used in the spectral fits. Inclusion of these modes into the theoretical spectra is justified on the grounds that structural disorder in amorphous carbon results in a breakdown of the Raman selection rules.[10,38,51-54] The frequency for the 6-membered ring A_{1g} mode was not taken from the embedded ring calculations, however, for two reasons. First, the coupling force constant in the VFM was chosen to model E-type ring mode motions, and the results of Table 7 support this contention. Second, the actual frequency for the A_{1g} mode (1360 cm^{-1}) is readily obtained from the experimental Raman spectrum of nanocrystalline graphite. To forego use of this experimentally determined frequency would reflect a disregard for a realistic model of the Raman spectrum of a-C.

Table 8 lists a representative sample of the spectral fits performed. The spectral fits are listed in descending order with respect to their chi-squared error, indicating an ascending order for the quality of the fit (a lower chi-squared error corresponds to a better fit to the experimental spectrum). Four of the spectral fits incorporated Beeman's ring statistical models C1120 (spectral fits two and four) and C340 (spectral fits one and three), and were modeled with only E-type modes from 5-, 6-, and 7-membered rings. These fits yielded large chi-squared values ($\chi^2>350$).

Two of the spectral fits (seven and eight) deviate substantially from a physically realistic model by incorporating only 5- and 7-membered rings into the ring statistics. They were included in Table 8 to show that spectral fits with χ^2 values greater than 116 may not represent physically meaningful results. Four spectral fits in Table 8 (nine to twelve) produced chi-squared errors of $\chi^2\leq100$. Note that the best spectral fits (ten, eleven, and twelve) incorporate the 6-membered ring A_{1g} mode, and give chi-squared errors of $\chi^2\leq77$.

Figures 17, 18, and 19 are theoretical spectra from spectral fits nine, ten, and twelve, respectively. The theoretical spectrum in Figure 17(a) incorporates only E-type modes for 5-, 6-, and 7-membered rings (5- and 7-membered ring E_1' and E_2' modes and 6-membered ring E_{2g} mode). Peak widths which yielded the best fit ($\chi^2=100$) for this five-mode

TABLE 8. Representative spectral fits to the experimental Raman spectrum of amorphous carbon, listed in descending chi-squared error (χ^2) order.

Spectral Fit No.	Ring Statistics in % No. of n-size Rings (4-n,5-n,6-n,7-n,8-n)	Modes and σ Peak Widths in cm^{-1}	Chi-Squared Error (χ^2)
1	(0, 11, 65, 24, 0)	5-n E_2'; σ=100 6-n E_{2g}; σ=100 7-n E_2'; σ=100	1031
2	(0, 21, 59, 20, 0)	5-n E_1'; σ= 90 5-n E_2'; σ= 90 6-n E_{2g}; σ= 90 7-n E_1'; σ= 90 7-n E_2'; σ= 90 7-n E_3'; σ= 90	433
3	(0, 11, 65, 24, 0)	5-n E_1'; σ=100 5-n E_2'; σ=100 6-n E_{2g}; σ=100 7-n E_1'; σ=100 7-n E_2'; σ=100 7-n E_3'; σ=100	411
4	(0, 21, 59, 20, 0)	5-n E_1'; σ=100 5-n E_2'; σ=100 6-n E_{2g}; σ=100 7-n E_1'; σ=100 7-n E_2'; σ=100 7-n E_3'; σ=100	391
5	(0, 25, 50, 25, 0)	5-n E_1'; σ=100 5-n E_2'; σ=100 6-n E_{2g}; σ=100 7-n E_1'; σ=100 7-n E_2'; σ=100 7-n E_3'; σ=100	313
6	(0, 33, 33, 33, 0)	5-n E_1'; σ=100 5-n E_2'; σ=100 6-n E_{2g}; σ=100 7-n E_1'; σ=100 7-n E_2'; σ=100 7-n E_3'; σ=100	222

TABLE 8. Continued.

Spectral Fit No.	Ring Statistics in % No. of n-size Rings (4-n,5-n,6-n,7-n,8-n)	Modes and σ Peak Widths in cm^{-1}	Chi-Squared Error (χ^2)
7	(0, 50, 0, 50, 0)	5-n E_1' ; $\sigma=100$ 5-n E_2' ; $\sigma=100$ 7-n E_1' ; $\sigma=100$ 7-n E_2' ; $\sigma=100$ 7-n E_3' ; $\sigma=100$	136
8	(0, 30, 0, 70, 0)	5-n E_1' ; $\sigma=100$ 5-n E_2' ; $\sigma=100$ 7-n E_1' ; $\sigma=100$ 7-n E_2' ; $\sigma=100$ 7-n E_3' ; $\sigma=100$	116
9	(0, 33, 33, 33, 0)	5-n E_1' ; $\sigma=130$ 5-n E_2' ; $\sigma=130$ 6-n E_{2g}; $\sigma=65$ 7-n E_1' ; $\sigma=130$ 7-n E_2' ; $\sigma=130$	100
10	(0, 0, 100, 0, 0)	6-n A_{1g}; $\sigma=175$ 6-n E_{2g}; $\sigma=75$	77
11	(10, 20, 40, 20, 10)	4-n E_{1u}; $\sigma=90$ 5-n E_2' ; $\sigma=90$ 6-n A_{1g}; $\sigma=170$ 6-n E_{2g}; $\sigma=95$ 7-n E_2' ; $\sigma=90$ 8-n E_{2g}; $\sigma=90$	36
12	(0, 25, 50, 25, 0)	5-n E_2' ; $\sigma=90$ 6-n A_{1g}; $\sigma=170$ 6-n E_{2g}; $\sigma=95$ 7-n E_2' ; $\sigma=90$	35

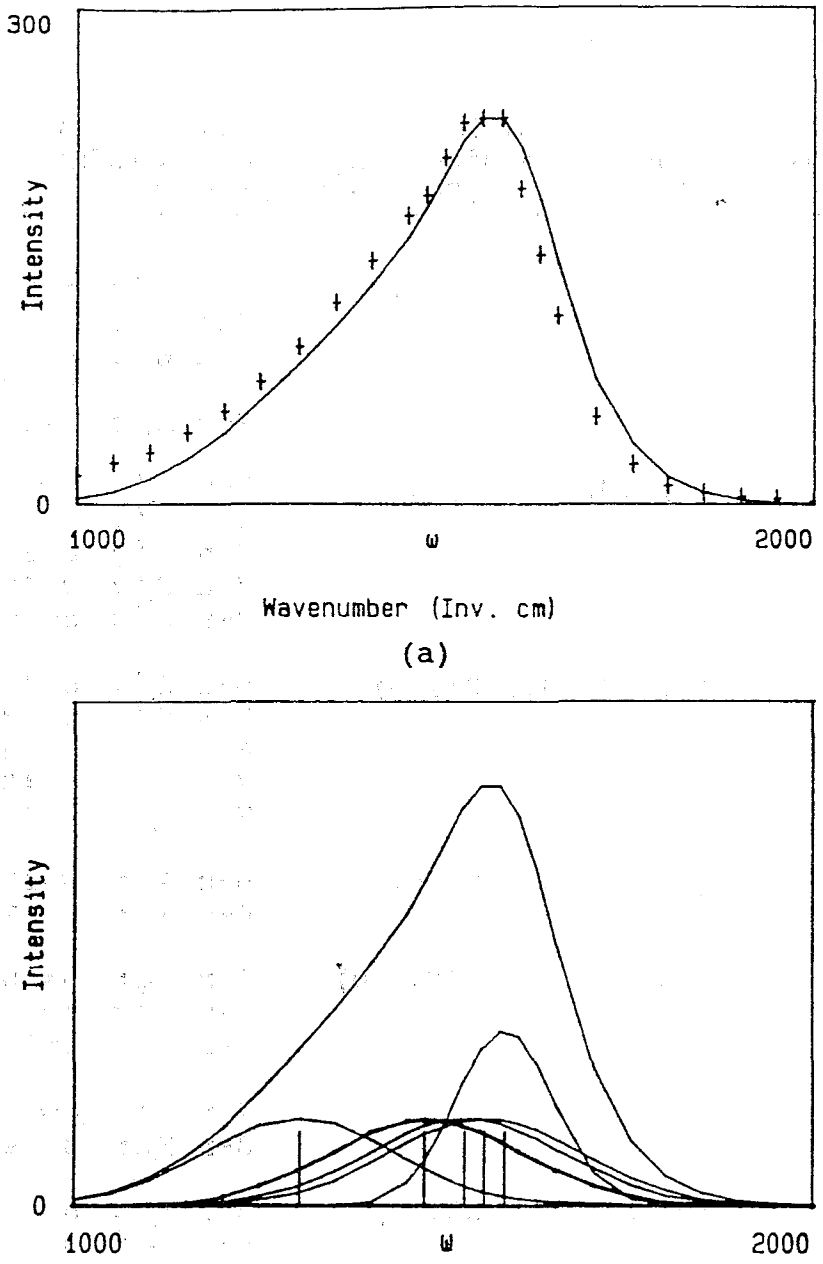

(a)

(b)

FIG. 17. Theoretical spectrum (a) and deconvoluted peaks (b) for E-type mode frequencies of 5-, 6-, and 7-membered rings. Theoretical spectrum (solid line) overlays experimental spectrum (†). Model was based on an equal distribution of ring sizes.

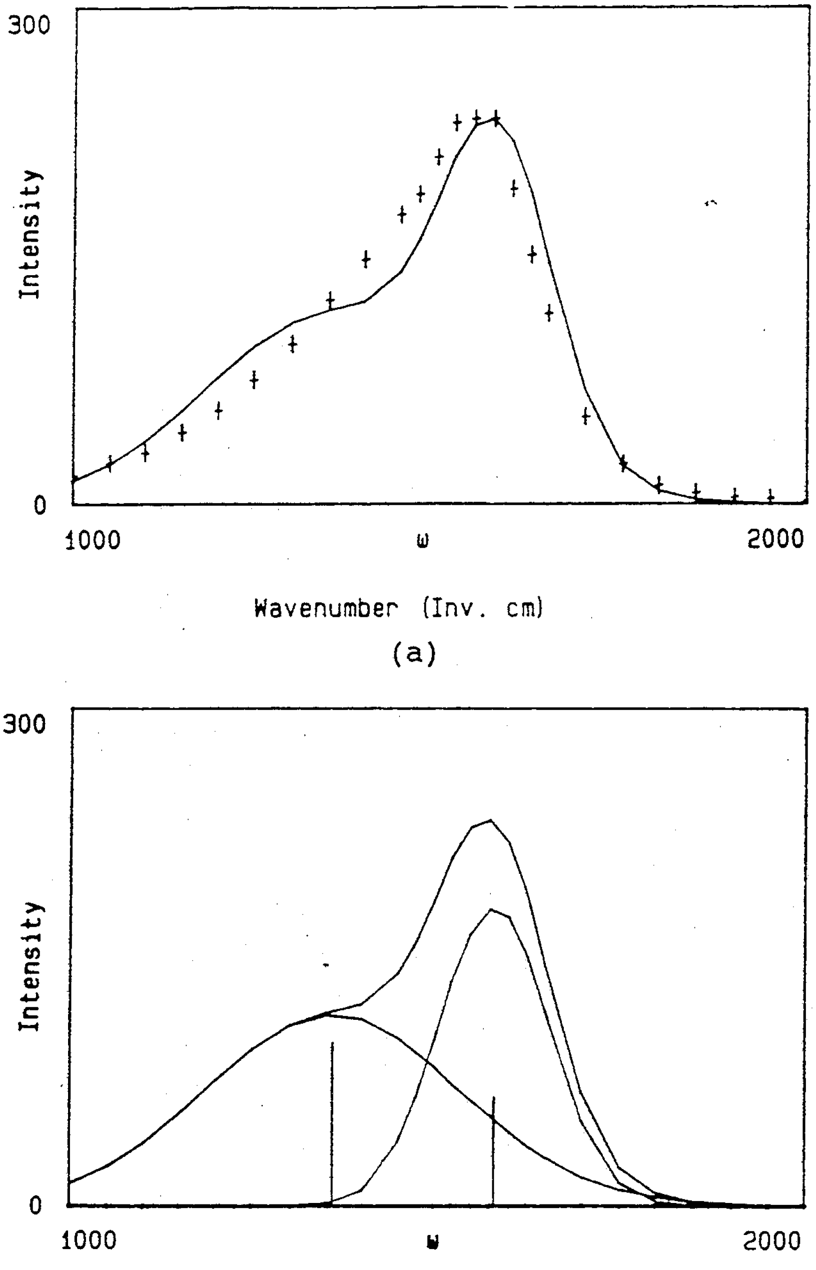

(a)

(b)

FIG. 18. Theoretical spectrum (a) and deconvoluted peaks (b) for 6-membered ring A_{1g} and E_{2g} mode frequencies. Theoretical spectrum (solid line) overlays experimental spectrum (†).

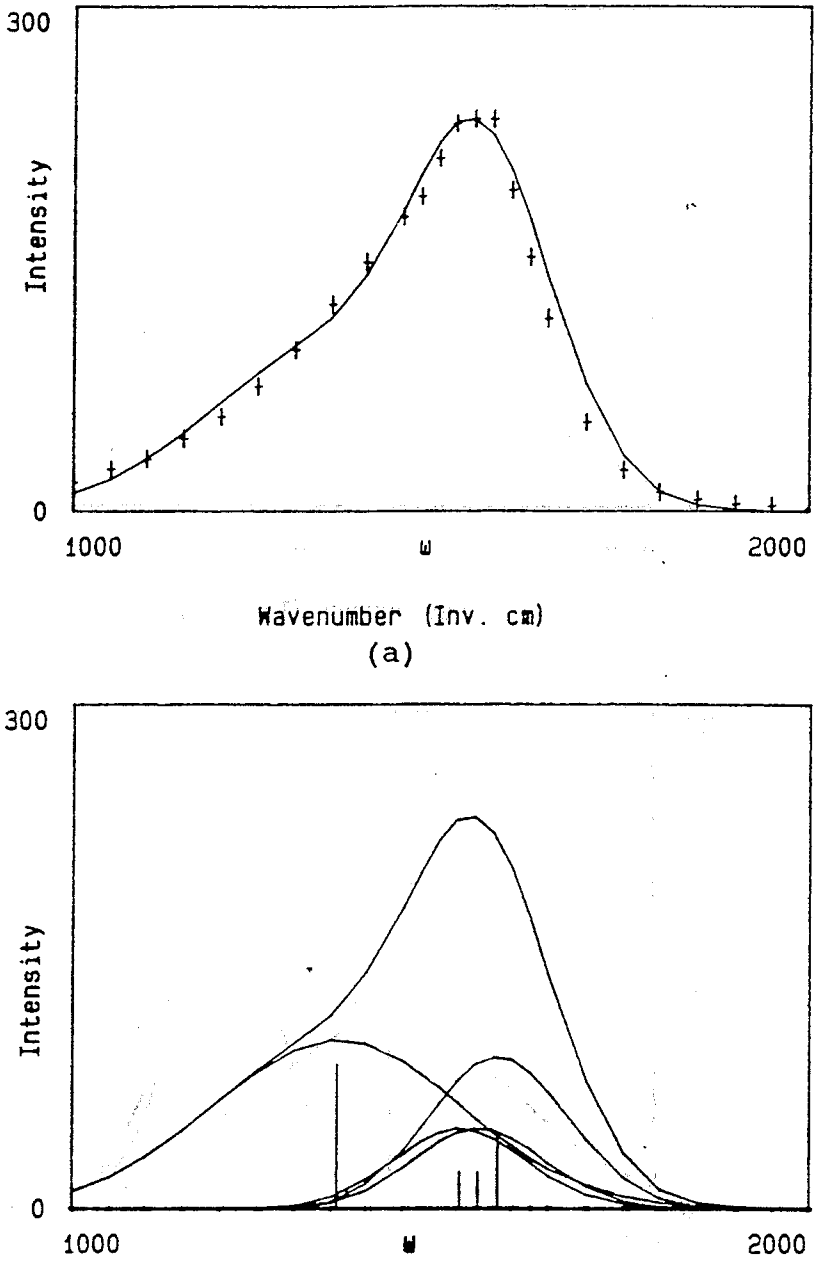

(a)

(b)

FIG. 19. Theoretical spectrum (a) and deconvoluted peaks (b) for E_2' modes of 5- and 7-membered rings, and A_{1g} and E_{2g} modes of 6-membered ring. Ring statistics were 0.25, 0.50, and 0.25 for 5-, 6-, and 7-membered rings, respectively.

spectrum were σ=130 cm^{-1} for the 5- and 7-membered ring modes and σ=65 cm^{-1} for the 6-membered ring E_{2g} mode. The ring statistics for this five-mode model have equal numbers (33⅓% each) of 5-, 6-, and 7-membered rings. Figure 17(b) displays the deconvoluted peaks for the theoretical spectrum.

Figure 18 presents a theoretical spectrum (a) and its deconvoluted constituent peaks (b) for a model with only one ring size in its distribution--the 6-membered ring--and with only two modes--the A_{1g} mode and E_{2g} mode. The peak widths were σ = 175 cm^{-1} for the A_{1g} mode (1360 cm^{-1}) and σ = 75 cm^{-1} for the E_{2g} mode (1581 cm^{-1}). The integrated peak intensity for the A_{1g} mode was set at twice that of the E_{2g} mode, and can be justified by referring to spectra of nanocrystalline graphite where the broader A_{1g} peak is equal to or greater in height than the E_{2g} peak.[10,51-53] The above intensities and peak widths resulted in a fit with an error of only χ^2 = 77.

Visual inspection of the theoretical spectrum in Figure 18 reveals two major discrepancies with the experimental spectrum of amorphous carbon:

1. A shoulder near 1360 cm^{-1} in the theoretical spectrum is absent in the experimental spectrum. Consequently, the theoretical spectrum is more intense than the experimental spectrum at frequencies below 1360 cm^{-1} and less intense at frequencies above 1360 cm^{-1}.

2. The maximum of the theoretical spectrum is 10-20 cm^{-1} higher in frequency than the maximum for the experimental spectrum. Consequently, the theoretical spectrum is more intense than the experimental spectrum at frequencies above 1575 cm^{-1} and less intense at frequencies below 1575 cm^{-1}.

Varying the integrated peak intensities and peak widths of the A_{1g} and E_{2g} 6-membered ring modes cannot remove these discrepancies. Only inclusion of mode frequencies between 1360 cm^{-1} and 1580 cm^{-1} can eliminate the low-frequency shoulder and shift the maximum to lower frequencies.

A natural place to look for these mid-frequency modes (between 1360 cm^{-1} and 1580 cm^{-1}) would be other 6-membered ring modes. Remember, however, that the embedded ring approach assumes that a 6-membered ring embedded into a graphite hexagonal lattice should yield the same mode frequencies as found in graphite. No normal mode frequencies between 1360 cm^{-1} and 1580 cm^{-1} are observed in graphite, including both in-plane and out-of-plane modes.[3] The mode closest to the A_{1g} and E_{2g} mode frequencies--the infrared active, in-plane E_{1u} mode--has a frequency of 1587 cm^{-1}, slightly higher than the E_{2g} mode. We are therefore forced to resort to smaller (4- and 5-membered) and/or larger (7- and 8-membered) sized rings to obtain mid-frequency modes.

Figure 19(a) and 19(b) show the theoretical spectrum of a model incorporating the Raman-active E_2' modes of the 5-

and 7-membered embedded rings along with the A_{1g} and E_{2g} modes of the 6-membered ring. Frequencies for the E_2' modes were calculated with the valence force model. The ring statistics were 25% 5-membered rings, 50% 6-membered rings, and 25% 7-membered rings, and provided the best fit for the spectrum. The 6-membered ring A_{1g} mode was again taken to have twice the integrated peak intensity of the 6-membered ring E_{2g} mode. Peak widths which provided the best fit were $\sigma_1 = 90$ cm^{-1} (E_2' modes of 5- and 7-membered rings), $\sigma_2 = 170$ cm^{-1} (A_{1g} mode of 6-membered ring), and $\sigma_3 = 95$ cm^{-1} (E_{2g} mode of 6-membered ring).

The theoretical spectrum in Figure 19, with an error of only $\chi^2 = 35$, gives the best fit out of all of the models ran on the convolution program. Compared with the theoretical spectrum in Figure 18, the inclusion of the E_2' modes from 5- and 7-membered rings along with the 6-membered ring A_{1g} and E_{2g} modes reduces the chi-squared error by a factor of 2.2, and eliminates the discrepancies arising from the 1360 cm^{-1} shoulder and the frequency shift of the maximum. Note that the peak widths for the 5- and 7-membered ring E_2' modes (90 cm^{-1}) are close to the peak width of the 6-membered ring E_{2g} mode (95 cm^{-1}), and that the peak widths for all three modes are less than twice the maximum peak widths (50 cm^{-1}) reported for silica glasses.[72]

The ring statistics for the theoretical spectrum in Figure 19 are also physically reasonable. As a comparison, Beeman's C1120 model for a-C with no sp_3 bonding contained 21% 5-membered rings, 59% 6-membered rings, and 20% 7-membered rings. Note that approximately equal proportions of 5- and 7-membered rings are required for a 2D-CRN to prevent excessive warpage or curvature in the network, or to prevent the structure from curling into a large spheroidal molecule. Finally, the most probable 5- and 7-membered ring modes to appear in the Raman spectrum of a-C would be the Raman active E_2' modes.

It can be concluded from the improvement in the fitting of the theoretical spectrum to the experimental spectrum (Table 8, spectral fit twelve) that a-C contains a substantial number of both 5- and 7-membered rings. The fitting results indicate that only about half of the rings in a-C are 6-membered. Only a CRN could accommodate such a large percentage of 5- and 7-membered rings. Since five-fold and seven-fold symmetries are incompatible with 2D periodicity (as demonstrated with 2D tilings of polygons) a continuous network comprising a large proportion of 5- and 7-membered rings is necessarily aperiodic and thus structurally random.[28]

Figure 20 displays a triangle raft model (a) and ring statistics (b) for a structural model of a-C corresponding to Figure 19 (spectral fit twelve), and is the structural model

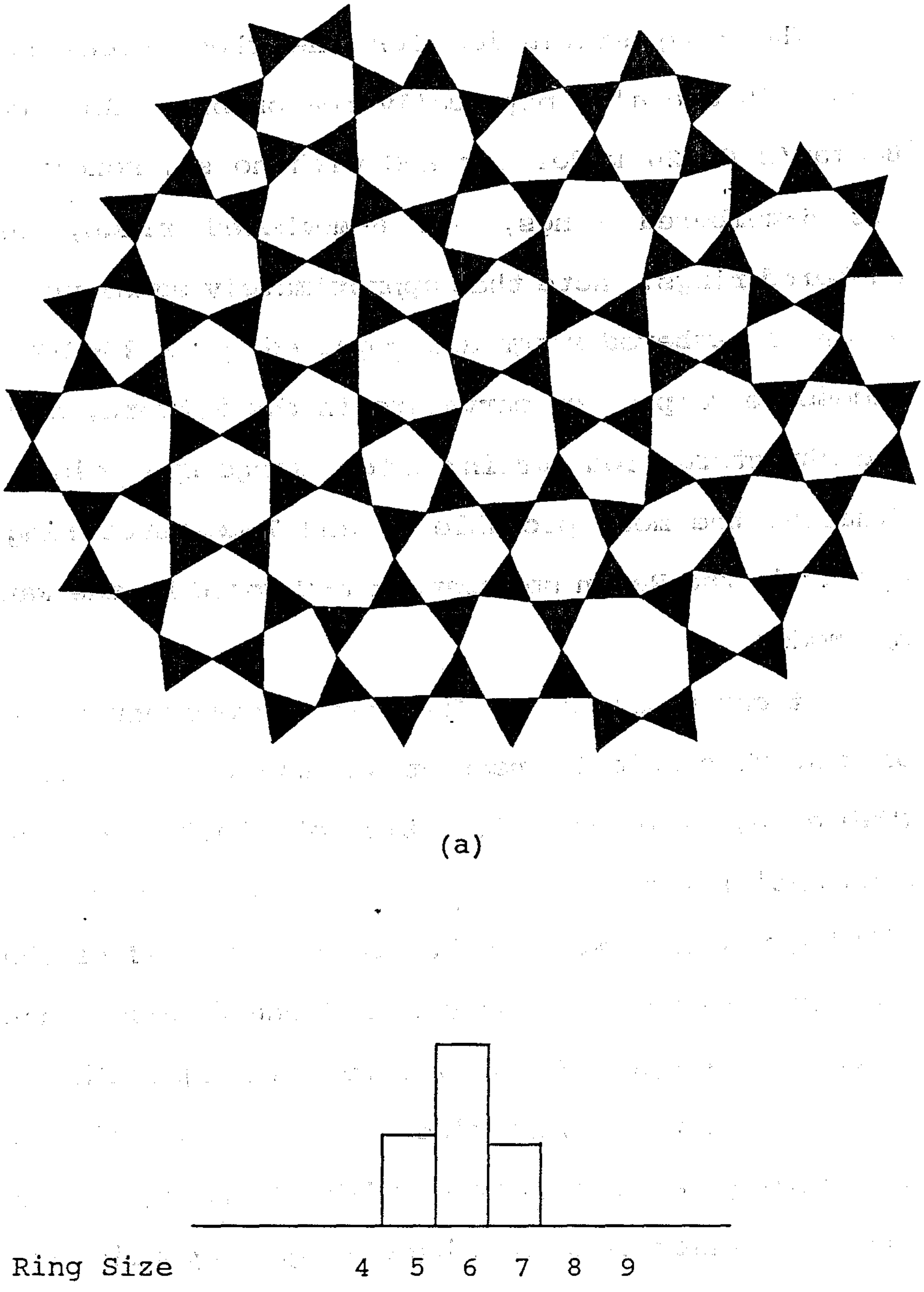

(a)

(b)

FIG. 20. Triangle raft model (a) and ring statistics (b) for the structure of amorphous carbon predicted by the embedded ring approach.

for graphitic a-C predicted by the embedded ring approach. Note that the network's structure is aperiodic, and represents a 2D-CRN with only 5-, 6-, and 7-membered rings.

The 4-membered ring E_{1u} mode and 8-membered ring E_{2g} mode were incorporated into the theoretical spectrum of Figure 19 to assess the effect of these ring modes on the spectral fit. The lack of improvement in the spectral fit (Table 8, spectral fit eleven) can be taken to reflect an absence of 4- and 8-membered ring modes in the Raman spectrum of a-C. It can therefore be concluded that 4- and 8-membered rings do not significantly contribute to the structure of a-C. This is a physically realistic result since 4- and 8-membered rings are not expected in large concentration in a-C due to the increased bond-angle energy required to form these rings. Additionally, Beeman <u>et al</u>.[40] did not include 4- and 8-membered rings into their model ring statistics, again due to the increased bond-angle energy for these rings.

Bond Angle Distribution and Peak Widths

Because of the inability to tile a 2D lattice with perfect pentagons, hexagons, and septagons (except by curling the 2D lattice into a third dimension, as is found for 5- and 6-membered rings in the fullerenes [24-26]), many of the rings will deviate from their ideal polygonal shape. These deviations will create a distribution of bond angles (as opposed to a single, ideal bond angle) for each class (size

n) of rings. Bond-angle fluctuations in amorphous silicon and germanium induce broadening of bands in their Raman spectra, and the bandwidths provide a means to measure the bond-angle distribution.[74] The effect of this bond-angle distribution on the vibrational modes could be analyzed with the VFM.

The g-matrix elements are a function of bond angle. Replacing the idealized, single-valued bond angles in the g-matrix elements with a distribution of bond angles would result in a distribution of eigenfrequencies calculated from the secular determinant. Each vibrational species would then exhibit a distribution of mode frequencies instead of an ideal, single-valued, delta-function mode frequency. The distribution would most likely be gaussian due to the inhomogeneous nature of the bond-angle disorder. The average or mean for the bond-angle distribution would most likely lie near the values for the idealized bond angles. Therefore, the gaussian frequency distribution would be centered at or near the idealized mode frequency.

From the foregoing argument, the rather large peak widths of the gaussian peaks used to produce the theoretical spectrum in Figure 19 can now be explained by the extreme distortion of 5-, 6-, and 7-membered rings in a 2D-CRN. The narrower peak widths exhibited by silica can be attributed to either ring-network decoupling of the oxygen breathing modes, or to a narrower distribution of bond angles due to the presence of medium-range order.[14,75]

A third explanation is that since silica glasses are 3D networks, n-membered rings are accommodated into the network with less bond-angle distortion than they would have in a 2D network. The extra third dimension provides an added degree of freedom for the configuration of silica tetrahedra and the rings they form. The decrease in bond-angle distortion results in a narrower distribution of bond angles, and consequently narrower Raman peaks for the 3D silica networks as compared to the 2D a-C networks.

Although a bond-length distribution also introduces band broadening, only a narrow bond-length distribution is observed in a-C for nearest neighbor atoms. (The variations in bond length fit a gaussian distribution, and were measured with the use of radial distribution functions obtained from neutron diffraction.[44])

The improved theoretical spectrum fit in Figure 19 provides evidence supporting both the validity of the embedded ring approach and a CRN structural model for a-C. The ring statistics favor the presence of 5- and 7-membered rings at significant levels in a-C. Convolutions incorporating 4- and 8-membered ring modes failed to produce theoretical spectra with chi-squared errors less than those reported. The large widths of the gaussian peaks for the 5-, 6-, and 7-membered rings most likely arise from an inhomogeneous distribution of bond angles within the rings.

The source of the peak broadening is directly traceable in the embedded ring approach, suggesting a method both quantitative and analytical for determining bond-angle disorder in an amorphous solid with the use of vibrational spectra.

CHAPTER VII

SUMMARY AND CONCLUSIONS

Several analytical and numerical methods are used to determine the vibrational dynamics of amorphous materials. However, there exists no generalized analytical method which can calculate the vibrational density of states for an amorphous material. Although not a generalized method, the embedded ring approach has been developed to address this deficiency. The embedded ring approach models the vibrational dynamics for amorphous 2D materials, making it applicable to a wide range of materials with scientific and technological interest.

Inherent in the use of the embedded ring approach is the selection of an appropriate structural model for amorphous 2D materials. Covalent amorphous materials form disordered structures known as continuous random networks (CRN's). Two-dimensional CRN's are modeled with the use of Zachariasen schematics and triangle rafts. Triangle raft models are appealing for their ease of construction and the ability to obtain the ring statistics from the modeled structure. The emphasis on ring structures in triangle raft models make them especially useful in the application of the embedded ring approach. By assuming the vibrational mode intensities for various sized rings in a CRN are proportional to the distribution of ring sizes, the embedded ring approach can produce theoretical spectra which can be used to determine the ring statistics for a given material.

Amorphous carbon (a-C) was used as a test case for the embedded ring approach. The planar, three-fold coordination of sp_2 bonds in a-C is thought to be conducive to the formation of 2D-CRN structures. Evidence exists to support this model, but the problems of graphitelike, hexagonal ordering on a fine scale (~ 10 Å) and the effect of four-fold, tetrahedrally-coordinated sp_3 bonds on the structure is still an open question.

A preface to the embedded ring approach was the examination of the vibrational dynamics of polycyclic aromatic hydrocarbons (PAH's). The vibrational modes of an isolated molecular ring structure, such as benzene, are modified by the addition of other rings in PAH molecules. The changes in the vibrational modes for a specific ring can be attributed to coupling of the ring motions to the motions of the surrounding structure. The effects of coupling were examined in a systematic fashion by analyzing the shift in a specific mode frequency for successively larger PAH molecules. A conclusion of this work was that the coupling between an individual ring and the surrounding molecular structure changes little for molecules comprised of more than three rings. Thus, complete ring-network coupling is achieved with relatively small ring assemblages.

The embedded ring approach is similar to other analytical methods because of its emphasis on the local structure in amorphous materials. The local structural units for the embedded ring approach are planar 4-, 5-, 6-, 7-, and 8-membered rings. The rings are treated as molecules embedded into a rigid hole in a 2D network. Methods for the study of molecular dynamics are then employed to determine the vibrational modes. Each ring atom was coupled to the wall of the hole with a bond (spring) having an effective force constant differing from the normal bond-stretching force constant. This effective coupling force constant models the effect of the embracive network on the ring's vibrational modes. The vibrational modes for the ring were then determined with the small oscillation approximation. The potentials were approximated with either a central force model (bond-stretching and coupling force constants only) or the valence force model (bond-stretching, bond-angle-bending, and coupling force constants).

Central force model calculations were performed with the method of small oscillations. The valence force model, however, also required the use of group theory to solve for the vibrational mode frequencies. By configuring the equilibrium positions of the rings into the shapes of regular (ideal) polygons, the in-plane vibrational modes for the rings were solved with the use of their symmetry point groups and the normal coordinate treatment.

Results for two central force models and the valence force model were compared. In comparison to the valence force model, the central force models were good approximations, but produced too many degenerate mode frequencies. On the other hand, loss of degeneracy was a problem for the valence force model. The loss of degeneracy arises from the coupling of the isolated ring modes to the network (i.e., the coupling of the embedded ring to the wall of the rigid hole).

The Raman spectrum of a-C provided experimental data for testing the validity of the embedded ring approach and the CRN model for a-C. Calculated mode frequencies were compared to the a-C spectrum by constructing theoretical spectra. The vibrational modes were assumed to have gaussian profiles with integrated peak intensities directly proportional to the ring statistics. Convolution of the modes produced the theoretical spectra. The number of modes, peak widths, and ring statistics were varied to produce the best fit to the data.

The theoretical spectrum providing the best fit to the Raman spectrum of a-C included only the 5- and 7-membered ring E_2' mode frequencies and the 6-membered ring A_{1g} and E_{2g} mode frequencies. The E_{2g} and A_{1g} mode frequencies were obtained from published Raman spectra of graphite and nanocrystalline graphite. Frequencies for the 5- and 7-membered ring E_2' modes were analytically calculated with the use of the embedded ring approach and the valence force model. Although the Raman spectrum of a-C can be approximated with solely the 6-membered ring E_{2g} and A_{1g} modes, the incorporation of the 5- and 7-membered ring E_2' modes into the theoretical spectrum substantially improved the fitting.

The ring statistics corresponding to the best fit are realistic, with 25% 5-membered rings, 50% 6-membered rings, and 25% 7-membered rings. The results suggest that a-C has a CRN structure, with 5- and 7-membered rings comprising a significant percentage of the total number of rings.

The embedded ring approach uses simple, first-principle, classical theory to model the vibrational dynamics of 2D amorphous materials. The initial success of the embedded ring approach in its application to a-C demonstrates the viability of the approach. Further work, however, is required to develop and establish the embedded ring approach as a powerful theoretical method.

The application of the embedded ring approach to a-C can be expanded to include modeled fits of theoretical spectra to infrared spectra, which display different selection rules, and to inelastic neutron spectra, which provide the VDOS due to a complete absence of selection rules. The embedded ring approach could also be applied to the vibrational dynamics of the buckminsterfullerenes [76,77] or large PAH molecules, such as hexabenzocoronene. More research should be conducted on the asymptotic trend of vibrational mode frequencies to graphite mode frequencies for increasingly larger PAH molecules.

The embedded ring approach could also be extended to covalent 3D amorphous materials by examining the vibrational dynamics of polyhedra-forming atomic clusters in the 3D network.[14] The polyhedra would be 3D analogs of 2D planar rings, and modified vibrational modes for isolated polyhedra embedded into an embracive network would be determined by the same methods as outlined in this work. Such an "embedded polyhedron approach" would have wider application and utility than the embedded ring approach, but more in-depth research on the embedded ring approach is required before the technique is extended to 3D amorphous solids.

Areas that need to be studied with greater detail in the embedded ring approach are:

1. the loss of degeneracy in the VFM, and whether it has any physical significance;
2. the assumptions and criteria for selection of coupling force constants;
3. the significance of the A_{1g} mode in a-C and PAH molecules;
4. and the effective mass approach, and whether it is is equivalent to or has advantages over the coupling force constant approach.

Finally, other materials need to be examined with the embedded ring approach. A few suggested materials are:

1. planar rings in SiO_2- and B_2O_3-based glasses, and the phenomenon of ring-network decoupling for

certain vibrational modes;

2. amorphous As_2Se_3, As_2S_3, and As_2O_3;
3. 2D, in-plane vibrational modes of the CuO_2 layers in high temperature superconductors;
4. and 3D amorphous materials, such as diamondlike a-C, amorphous silicon, and amorphous germanium.

The approach taken in this thesis pioneers a new method for determining the ring statistics of an amorphous material from its vibrational spectrum. Additionally, the approach may also provide a method for measuring bond angle distributions in amorphous materials. The peak widths of the vibrational modes in the theoretical spectrum should be directly traceable to the bond angles in the g-matrix elements of the secular determinants. If so, a new method for the analytical modeling and characterization of amorphous materials may be developed with the embedded ring approach.

The embedded ring approach can be judged a modest success at modeling the Raman spectrum of amorphous carbon. Further research with new materials and improved methods will provide the final verdict as to whether the embedded ring approach is an ephemeral idea or a lasting contribution to science.

REFERENCES

1. N. W. Ashcroft and N. D. Mermin, Solid State Physics (W. B. Saunders, Philadephia, 1976), pp. 421-468, 780-783.

2. S. R. Elliott, Physics of Amorphous Materials, 2nd ed. (John Wiley & Sons, New York, 1990), pp. 185-205.

3. S. Nakashima, M. Hangyo, and A. Mitsuishi, in Vibrational Spectra and Structure, edited by J. R. Durig (Elsevier, New York, 1985), Vol. 14, pp. 305-431.

4. P. N. Ghosh, in Vibrational Spectra and Structure, edited by J. R. Durig (Elsevier, New York, 1986), Vol. 15, pp. 157-250.

5. C. A. Sorrell, Rocks and Minerals (Western Publishing, Racine, Wisconsin, 1973), pp. 186-201.

6. C. P. Poole, Jr., T. Datta, and H. A. Farach, Copper Oxide Superconductors (John Wiley & Sons, New York, 1988).

7. High Temperature Superconductivity, edited by J. W. Lynn (Springer-Verlag, New York, 1990).

8. R. Zallen, The Physics of Amorphous Solids (John Wiley & Sons, New York, 1983).

9. J. S. Blakemore, Solid State Physics, 2nd ed. (Cambridge University Press, Cambridge, Great Britain, 1985), p. 118.

10. R. J. Nemanich and S. A. Solin, Phys. Rev. B **20** (2), 392-401 (1979).

11. K. Kesavasamy and N. Krishnamurthy, Indian Journal of Pure and Applied Physics **17**, 73-79 (1979).

12. R. J. Bell, A. Carnevale, C. R. Kurkjian, and G. E. Peterson, J. Non-Cryst. Solids **35 & 36**, 1185-1190 (1980).

13. S. K. Sharma, J. F. Mammone, and M. F. Nicol, Nature **292**, 140-141 (1981).

14. S. R. Elliott, Nature **354**, 445-452 (1991).

15. F. L. Galeener, J. Non-Cryst. Solids **49**, 53-62 (1982).

16. F. L. Galeener, Solid State Commun. **44** (7), 1037-1040 (1982).

17. F. L. Galeener, R. A. Barrio, E. Martinez, and R. J. Elliott, Phys. Rev. Lett. **53** (25), 2429-2432 (1984).

18. S. K. Sharma and B. Simons, American Mineralogist **66**, 118-126 (1981).

19. W. H. Zachariasen, J. Am. Chem. Soc. **54**, 3841-3851 (1932).

20. J. F. Shackelford, J. Non-Cryst. Solids **49**, 19-28 (1982).

21. W. Eitel, <u>Silicate Science, Vol. 1: Silicate Structures</u> (Academic Press, New York, 1964), pp. 19, 106, 119.

22. <u>Introduction to Quasicrystals</u>, edited by M. V. Jaric (Academic Press, San Diego, 1988).

23. P. J. Steinhardt, American Scientist **74** (6), 586-597 (1986).

24. H. Kroto, Science **242**, 1139-1145 (1988).

25. R. F. Curl and R. E. Smalley, Scientific American **265** (4), 54-63 (1991).

26. Q. M. Zhang, J. Y. Yi, and J. Bernholc, Phys. Rev. Lett. **66** (20), 2633-2636 (1991).

27. P. E. Ross, Scientific American **265** (6), 24 (1991).

28. J. Kappraff, <u>Connections</u> (McGraw-Hill, New York, 1991).

29. W. Kratschmer, L. D. Lamb, K. Fostiropoulos, and D. R. Huffman, Nature **347**, 354-358 (1990).

30. D. R. Huffman, Physics Today **44** (11), 22-29 (1991).

31. F. Diederich, R. Ettl, Y. Rubin, R. L. Whetten, R. Beck, M. Alvarez, S. Anz, D. Sensharma, F. Wudl, K. C. Khemani, and A. Koch, Science **252**, 548-551 (1991).

32. A. F. Hebard, M. J. Rosseinsky, R. C. Haddon, D. W. Murphy, S. H. Glarum, T. T. M. Palstra, A. P. Ramirez, and A. R. Kortan, Nature **350**, 600-601 (1991).

33. M. J. Rosseinsky, A. P. Ramirez, S. H. Glarum, D. W. Murphy, R. C. Haddon, A. F. Hebard, T. T. M. Palstra, A. R. Kortan, S. M. Zahurak, and A. V. Makhija, Phys. Rev. Lett. **66** (21) 2830-2832 (1991).

34. R. S. Ruoff and A. L. Ruoff, Nature **350**, 663-664 (1991).

35. S. Iijima, Nature **354**, 56-58 (1991).

36. D. Vanderbilt and J. Tersoff, Phys. Rev. Lett. **68** (4), 511 (1992).

37. J. Robertson, Adv. Phys. **35** (4), 317-374 (1986).

38. R. O. Dillon, J. A. Woollam, and V. Katkanant, Phys. Rev. B **29** (6), 3482-3489 (1984).

39. A. B. Harker, Research and Development Magazine 84-92 (March 1990).

40. D. Beeman, J. Silverman, R. Lynds, and M. R. Anderson, Phys. Rev. B **30** (2), 870-875 (1984).

41. A. L. Ritter, J. R. Dennison, and R. Jones, Phys. Rev. Lett. **53** (21), 2054-2057 (1984).

42. C. Gao, Y. Y. Wang, A. L. Ritter, and J. R. Dennison, Phys. Rev. Lett. **62** (8), 945-948 (1989).

43. G. Galli, R. M. Martin, R. Car, and M. Parrinello, Phys. Rev. Lett. **62** (5), 555-558 (1989).

44. F. Li and J. S. Lannin, Phys. Rev. Lett. **65** (15), 1905-1908 (1990).

45. J. G. Grasselli, M. K. Snavely, and B. J. Bulkin, <u>Chemical Applications of Raman Spectroscopy</u> (John Wiley & Sons, New York, 1981), pp. 1 and 118.

46. V. G. Keramidas and W. B. White, J. Phys. Chem. Solids **34** (11), 1873-1878 (1973).

47. B. E. Scheetz and W. B. White, American Mineralogist **62**, 36-50 (1977).

48. W. B. White, in <u>Infrared and Raman Spectroscopy of Lunar and Terrestial Minerals</u>, edited by C. Karr, Jr. (Academic Press, New York, 1975), pp. 325-358.

49. J. R. Dennison, Ph.D. Thesis, Virginia Polytechnic Institute and State University, Blacksburg, VA, 1985.

50. Data for amorphous carbon taken by J. Wragg, University of Missouri-Columbia, 1990. Amorphous carbon samples purchased from Arizona Carbon Foil Company. Details of preparation given in J. O. Stoner, Jr., J. Appl. Phys. **40**, 707 (1969).

51. F. Tuinstra and J. L. Koenig, J. Chem. Phys. **53** (3), 1126-1130 (1970).

52. M. I. Nathan, J. E. Smith, Jr., and K. N. Tu, J. Appl. Phys. **45** (5), 2370 (1974).

53. R. Vidano and D. B. Fischbach, J. Am. Ceram. Soc. **61** (1-2), 13-17 (1978).

54. K. Sinha and J. Menendez, Phys. Rev. B **41** (15), 10845-10847 (1990).

55. M. Yoshikawa, G. Katagiri, H. Ishida, and A. Ishitani, J. Appl. Phys. **64** (11), 6464-6468 (1988).

56. G. Varsanyi, <u>Vibrational Spectra of Benzene Derivatives</u> (Academic Press, New York, 1969).

57. K. Ohno, Journal of Molecular Spectroscopy **77** (3) 329-348 (1979).

58. B. L. Crawford, Jr. and F. A. Miller, J. Chem. Phys. **17** (3), 249-256 (1949).

59. H. Goldstein, <u>Classical Mechanics</u>, 2nd ed. (Addison-Wesley, Reading, MA, 1980), pp. 243-274.

60. E. B. Wilson, Jr., J. C. Decius, and P. C. Cross, <u>Molecular Vibrations</u> (Dover, New York, 1955).

61. <u>Derive© Version 2</u> (Soft Warehouse, Inc., Honolulu, Hawaii, 1990).

62. B. E. Douglas and C. A. Hollingsworth, <u>Symmetry in Bonding and Spectra</u> (Academic Press, Orlando, Florida, 1985).

63. D. C. Harris and M. D. Bertolucci, <u>Symmetry and Spectroscopy</u> (Oxford University Press, New York, 1978).

64. J. R. Ferraro and J. S. Ziomek, <u>Introductory Group Theory</u> (Plenum Press, New York, 1969).

65. E. B. Wilson, Jr., Phys. Rev. **45**, 706-714 (1934).

66. L. A. Woodward, Introduction to the Theory of Molecular Vibrations and Vibrational Spectroscopy (Oxford University Press, London, 1972).

67. J. Tersoff, Phys. Rev. Lett. **61** (25), 2879-2882 (1988).

68. R. Al-Jishi and G. Dresselhaus, Phys. Rev. B **26** (8), 4514-4522 (1982).

69. J. A. Young and J. V. Koppel, J. Chem. Phys. **42** (1), 357-364 (1965).

70. R. Nicklow, N. Wakabayashi, and H. G. Smith, Phys. Rev. B **5** (12), 4951-4962 (1972).

71. V. Schettino, Journal of Molecular Spectroscopy **34**, 78-96 (1970).

72. B. O. Mysen and D. Virgo, in Advances in Materials Research II, edited by R. L. Snyder, R. A. Condrate, Sr., and P. F. Johnson (Plenum Press, New York, 1985), pp. 43-55.

73. MathCAD© Version 2.0 (Addison-Wesley/MathSoft, Inc., Reading, MA, 1988).

74. J. S. Lannin, Phys. Today **41** (7), 28-35 (July 1988).

75. P. H. Gaskell, M. C. Eckersley, A. C. Barnes, and P. Chieux, Nature **350**, 675-677 (1991).

76. W. G. Harter and D. E. Weeks, J. Chem. Phys. **90** (9), 4727-4743 (1989).

77. D. E. Weeks and W. G. Harter, J. Chem. Phys. **90** (9), 4744-4771 (1989).

APPENDIX A

TABLES AND MATRICES FOR VALENCE FORCE MODEL CALCULATIONS

Presented are the symmetry coordinates, g-matrix elements, and G matrices used for the valence force model calculations. The 4-, 5-, 6-, 7-, and 8-membered rings are represented by the D_{4h}, D_{5h}, D_{6h}, D_{7h}, and D_{8h} symmetry groups, respectively. Character tables for these symmetry groups can be found in most treatises on elementary group theory and molecular dynamics. As described in Chapter III, the symmetry coordinates are instrumental in deriving the U matrix for each vibrational species. The U matrix is then used to transform the f and g matrices to F and G matrices for each vibrational species. The resulting F matrices remain diagonal, but the G matrices retain off-diagonal terms, with each G-matrix element comprising a linear combination of g-matrix elements. The F and G matrix of each vibrational species are then multiplied together to form the secular determinant (see Chapter III), and solution of the determinant yields the frequencies of vibration.

TABLE A1. Symmetry coordinates for selected fundamental modes of the five embedded rings.

4-Membered Ring

A_{1g} mode:

$$\frac{1}{2}(t_1+t_2+t_3+t_4)$$

$$\frac{1}{2}(s_1+s_2+s_3+s_4)$$

$$\frac{1}{2}(\alpha_1+\alpha_2+\alpha_3+\alpha_4)$$

B_{1g} mode:

$$\frac{1}{2}(s_1-s_2+s_3-s_4)$$

$$\frac{1}{2}(\alpha_1-\alpha_2+\alpha_3-\alpha_4)$$

B_{2g} mode:

$$\frac{1}{2}(t_1-t_2+t_3-t_4)$$

$$\frac{1}{2}(\beta_1-\beta_2+\beta_3-\beta_4)$$

E_{1u} mode:

$$\frac{1}{2}(t_1-t_2-t_3+t_4)$$

$$\sqrt{\frac{1}{2}}(s_1-s_3)$$

$$\sqrt{\frac{1}{2}}(\alpha_1-\alpha_3) \qquad \sqrt{\frac{1}{2}}(\beta_2-\beta_4)$$

TABLE A1 (Continued)

5-Membered Ring

E_1' mode:

$$\frac{-1}{2cos144°\sqrt{10}}[2t_1(1+cos72°)-t_2+4t_3cos144°-t_4+2t_5(1+cos72°)]$$

$$\sqrt{\frac{2}{5}}[s_1+s_2cos72°+s_3\cos144°+s_4cos144°+s_5cos72°]$$

$$\sqrt{\frac{2}{5}}[\alpha_1+\alpha_2cos72°+\alpha_3cos144°+\alpha_4cos144°+\alpha_5cos72°]$$

$$\frac{1}{2sin72°\sqrt{2}}[-2\beta_2cos144°+\beta_3-\beta_4+2\beta_5cos144°]$$

E_2' mode:

$$\frac{1}{2cos72°\sqrt{10}}[2t_1(1+cos144°)-t_2+4t_3cos72°-t_4+2t_5(1+cos144°)]$$

$$\sqrt{\frac{2}{5}}[s_1+s_2cos144°+s_3cos72°+s_4cos72°+s_5cos144°]$$

$$\sqrt{\frac{2}{5}}[\alpha_1+\alpha_2cos144°+\alpha_3cos72°+\alpha_4cos72°+\alpha_5cos144°]$$

$$\frac{1}{2sin144°\sqrt{2}}[2\beta_2cos72°-\beta_3+\beta_4-2\beta_5cos72°]$$

TABLE A1 (Continued)

6-Membered Ring

E_{2g} mode:

$$\sqrt{\frac{1}{12}}\,[t_1-2t_2+t_3+t_4-2t_5+t_6]$$

$$\sqrt{\frac{1}{12}}\,[2s_1-s_2-s_3+2s_4-s_5-s_6]$$

$$\sqrt{\frac{1}{12}}\,[2\alpha_1-\alpha_2-\alpha_3+2\alpha_4-\alpha_5-\alpha_6]$$

$$\frac{1}{2}\,[\beta_2-\beta_3+\beta_5-\beta_6]$$

8-Membered Ring

B_{1g} mode:

$$\sqrt{\frac{1}{8}}\,[s_1-s_2+s_3-s_4+s_5-s_6+s_7-s_8]$$

$$\sqrt{\frac{1}{8}}\,[\alpha_1-\alpha_2+\alpha_3-\alpha_4+\alpha_5-\alpha_6+\alpha_7-\alpha_8]$$

B_{2g} mode:

$$\sqrt{\frac{1}{8}}\,[t_1-t_2+t_3-t_4+t_5-t_6+t_7-t_8]$$

$$\sqrt{\frac{1}{8}}\,[\beta_1-\beta_2+\beta_3-\beta_4+\beta_5-\beta_6+\beta_7-\beta_8]$$

TABLE A1 (Continued)

7-Membered Ring

E-type modes:

$$\frac{1}{\cos\theta_3\sqrt{14}}[(t_1+t_7)(1+\cos\theta_1)+(t_2+t_6)(\cos\theta_1+\cos\theta_2)+(t_3+t_5)(\cos\theta_2+\cos\theta_3)+2t_4\cos\theta_3]$$

$$\sqrt{\frac{2}{7}}[s_1+s_2\cos\theta_1+s_3\cos\theta_2+s_4\cos\theta_3+s_5\cos\theta_3+s_6\cos\theta_2+s_7\cos\theta_1]$$

$$\sqrt{\frac{2}{7}}[\alpha_1+\alpha_2\cos\theta_1+\alpha_3\cos\theta_2+\alpha_4\cos\theta_3+\alpha_5\cos\theta_3+\alpha_6\cos\theta_2+\alpha_7\cos\theta_1]$$

$$\frac{1}{\sin\theta_1\sqrt{14}}[(\beta_2-\beta_7)(1-\cos\theta_2)+(\beta_3-\beta_6)(\cos\theta_1-\cos\theta_3)+(\beta_4-\beta_5)(\cos\theta_2-\cos\theta_3)]$$

Angle Mode	θ_1	θ_2	θ_3
E_1'	$2\pi/7$	$4\pi/7$	$6\pi/7$
E_2'	$4\pi/7$	$6\pi/7$	$2\pi/7$
E_3'	$6\pi/7$	$2\pi/7$	$4\pi/7$

TABLE A1 (Continued)

8-Membered Ring

E_{2g} mode:

$$\sqrt{\frac{1}{8}}\,[t_1-t_2-t_3+t_4+t_5-t_6-t_7+t_8]$$

$$\frac{1}{2}\,[s_1-s_3+s_5-s_7]$$

$$\frac{1}{2}\,[\alpha_1-\alpha_3+\alpha_5-\alpha_7]$$

$$\frac{1}{2}\,[\beta_2-\beta_4+\beta_6-\beta_8]$$

E_{1u} mode:

$$\sqrt{\frac{1}{[8(2+\sqrt{2})]}}\,[(t_1-t_4-t_5+t_8)(1+\sqrt{2})+t_2-t_3-t_6+t_7]$$

$$\sqrt{\frac{1}{8}}\,[\sqrt{2}s_1+s_2-s_4-\sqrt{2}s_5-s_6+s_8]$$

$$\sqrt{\frac{1}{8}}\,[\sqrt{2}\alpha_1+\alpha_2-\alpha_4-\sqrt{2}\alpha_5-\alpha_6+\alpha_8]$$

$$\sqrt{\frac{1}{8}}\,[\beta_2+\sqrt{2}\beta_3+\beta_4-\beta_6-\sqrt{2}\beta_7-\beta_8]$$

TABLE A2. Generalized g-matrix elements for embedded ring ring approach with the use of internal coordinates. In the expressions μ is the reciprocal mass of the ring atom, τ is the reciprocal atom-atom bond length, σ is the reciprocal atom-rigid wall distance, θ_1 is the ring's inner bond angle, and θ_2 is the angle between the coupling bond and atom-atom bond.

$$g_{ss}^{2}=\mu$$

$$g_{tt}^{2}=2\mu$$

$$g_{tt}^{1}=\mu\cos\theta_1$$

$$g_{st}^{1}=\mu\cos\theta_2$$

$$g_{t\alpha}^{2}=-\tau\mu\sin\theta_1$$

$$g_{t\alpha}^{1}\binom{1}{2}=\tau\mu\sin\theta_1$$

$$g_{s\alpha}^{1}\binom{1}{1}=-2\tau\mu\cos\theta_2\left[\frac{1-\cos\theta_1}{\sin\theta_1}\right]$$

$$g_{s\alpha}^{1}\binom{1}{2}=-\tau\mu\sin\theta_2$$

$$g_{s\beta}^{1}\binom{1}{2}=\frac{1}{2}\tau\mu\sin\frac{\theta_1}{2}$$

TABLE A2 (Continued)

$$g^{1}_{t\beta}\binom{1}{1}=\mu\,[\sigma\sin\frac{\theta_1}{2}+\frac{1}{2}\tau\sin\theta_1]$$

$$g^{1}_{t\beta}\binom{1}{2}=-\frac{1}{2}\tau\mu\sin\theta_1$$

$$g^{3}_{\alpha\alpha}=2\tau^2\mu\,[2-\cos\theta_1]$$

$$g^{2}_{\alpha\alpha}\binom{1}{0}=-2\tau^2\mu\,[1-\cos\theta_1]$$

$$g^{1}_{\alpha\alpha}\binom{2}{2}=-\tau^2\mu\cos\theta_1$$

$$g^{3}_{\beta\beta}=\mu\,[\sigma^2+2\sigma\tau\cos\frac{\theta_1}{2}+\tau^2(\frac{1}{2}+\cos^2\frac{\theta_1}{2})]$$

$$g^{2}_{\beta\beta}\binom{1}{0}=\tau\mu\cos\frac{\theta_1}{2}\,[\sigma+\tau\cos\frac{\theta_1}{2}]$$

$$g^{1}_{\beta\beta}\binom{2}{2}=\frac{1}{4}\tau^2\mu\cos\theta_1$$

$$g^{1}_{\alpha\beta}\binom{2}{2}=\frac{1}{2}\tau^2\mu\cos\theta_1$$

$$g^{1}_{\alpha\beta}\binom{2}{1}=\tau\mu\,[\tau+\sigma\cos\frac{\theta_1}{2}]$$

TABLE A3. G-matrices for 4-membered ring: A_{1g}, B_{1g}, B_{2g}, and E_{1u} modes. Asterisks (*) indicate redundant elements in the symmetric matrix.

$$\begin{bmatrix} g_{ss}^{2} & g_{st}^{1} \\ * & g_{tt}^{2}+2g_{tt}^{1} \end{bmatrix}$$

A_{1g} mode

$$\begin{bmatrix} g_{ss}^{2} & g_{s\alpha}^{1}\binom{1}{1}-2g_{s\alpha}^{1}\binom{1}{1} \\ * & g_{\alpha\alpha}^{3}-2g_{\alpha\alpha}^{2}\binom{1}{0}+g_{\alpha\alpha}^{1}\binom{2}{2} \end{bmatrix}$$

B_{1g} mode

$$\begin{bmatrix} g_{tt}^{2}-2g_{tt}^{1} & 2\left[g_{t\beta}^{1}\binom{1}{1}+g_{t\beta}^{1}\binom{1}{2}\right] \\ * & g_{\beta\beta}^{3}-2g_{\beta\beta}^{2}\binom{1}{0}+g_{\beta\beta}^{1}\binom{2}{2} \end{bmatrix}$$

B_{2g} mode

$$\begin{bmatrix} g_{ss}^{2} & \sqrt{2}g_{st}^{1} & g_{s\alpha}^{1}\binom{1}{1} & 2g_{s\beta}^{1}\binom{1}{2} \\ * & g_{tt}^{2} & \sqrt{2}\left[g_{t\alpha}^{2}-g_{t\alpha}^{1}\binom{1}{2}\right] & \sqrt{2}\left[g_{t\beta}^{1}\binom{1}{2}-g_{t\beta}^{1}\binom{1}{1}\right] \\ * & * & g_{\alpha\alpha}^{3}-g_{\alpha\alpha}^{1}\binom{2}{2} & 2g_{\alpha\beta}^{1}\binom{2}{1} \\ * & * & * & g_{\beta\beta}^{3}-g_{\beta\beta}^{1}\binom{2}{2} \end{bmatrix}$$

E_{1u} mode

TABLE A4. G-matrices for 5-membered ring: E_1' and E_2' modes. $C_1 = 2 \cos 72°$, $C_2 = 2 \cos 144°$, $S_1 = 2 \sin 72°$, and $S_2 = 2 \sin 144°$.

$$\begin{bmatrix} g_{ss}^{2} & -C_2 g_{st}^{1} & g_{s\alpha}^{1}\binom{1}{1}+C_1 g_{s\alpha}^{1}\binom{1}{2} & S_1 g_{s\beta}^{1}\binom{1}{2} \\ * & g_{tt}^{2}+C_1 g_{tt}^{1} & -C_2 g_{t\alpha}^{2}-C_1 g_{t\alpha}^{1}\binom{1}{2} & -S_2 g_{t\beta}^{1}\binom{1}{1}+S_1 g_{t\beta}^{1}\binom{1}{2} \\ * & * & g_{\alpha\alpha}^{3}+C_1 g_{\alpha\alpha}^{2}\binom{1}{0}+C_2 g_{\alpha\alpha}^{1}\binom{2}{2} & S_2 g_{\alpha\beta}^{1}\binom{2}{2}+S_1 g_{\alpha\beta}^{1}\binom{2}{1} \\ * & * & * & g_{\beta\beta}^{3}+C_1 g_{\beta\beta}^{2}\binom{1}{0}+C_2 g_{\beta\beta}^{1}\binom{2}{2} \end{bmatrix}$$

E_1' mode

$$\begin{bmatrix} g_{ss}^{2} & C_1 g_{st}^{1} & g_{s\alpha}^{1}\binom{1}{1}+C_2 g_{s\alpha}^{1}\binom{1}{2} & S_2 g_{s\beta}^{1}\binom{1}{2} \\ * & g_{tt}^{2}+C_2 g_{tt}^{1} & C_1 g_{t\alpha}^{2}+C_2 g_{t\alpha}^{1}\binom{1}{2} & -S_1 g_{t\beta}^{1}\binom{1}{1}-S_2 g_{t\beta}^{1}\binom{1}{2} \\ * & * & g_{\alpha\alpha}^{3}+C_2 g_{\alpha\alpha}^{2}\binom{1}{0}+C_1 g_{\alpha\alpha}^{1}\binom{2}{2} & -S_1 g_{\alpha\beta}^{1}\binom{2}{2}+S_2 g_{\alpha\beta}^{1}\binom{2}{1} \\ * & * & * & g_{\beta\beta}^{3}+C_2 g_{\beta\beta}^{2}\binom{1}{0}+C_1 g_{\beta\beta}^{1}\binom{2}{2} \end{bmatrix}$$

E_2' mode

TABLE A5. G-Matrix for 6-membered ring E_{2g} mode. Asterisks (*) indicate redundant elements in the symmetric matrix.

$$\begin{bmatrix} g_{ss}^{2} & g_{st}^{1} & g_{s\alpha}^{1}\binom{1}{1}-g_{s\alpha}^{1}\binom{1}{2} & \sqrt{3}\, g_{s\beta}^{1}\binom{1}{2} \\ * & g_{tt}^{2}-g_{tt}^{1} & g_{t\alpha}^{2}-2 g_{t\alpha}^{1}\binom{1}{2} & -\sqrt{3}\, g_{t\beta}^{1}\binom{1}{1} \\ * & * & g_{\alpha\alpha}^{3}-g_{\alpha\alpha}^{2}\binom{1}{0}-g_{\alpha\alpha}^{1}\binom{2}{2} & \sqrt{3}\,[g_{\alpha\beta}^{1}\binom{2}{1}-g_{\alpha\beta}^{1}\binom{2}{2}] \\ * & * & * & g_{\beta\beta}^{3}-g_{\beta\beta}^{2}\binom{1}{0}-g_{\beta\beta}^{1}\binom{2}{2} \end{bmatrix}$$

TABLE A6. G-matrices for 7-membered ring: E_1', E_2', and E_3' modes. Asterisks are redundant elements.

$$\begin{bmatrix} g_{ss}^2 & -C_3 g_{st}^1 & g_{s\alpha}^1\binom{1}{1}+C_1 g_{s\alpha}^1\binom{1}{2} & S_1 g_{s\beta}^1\binom{1}{2} \\ * & g_{tt}^2+C_1 g_{tt}^1 & -C_3 g_{t\alpha}^2-C_2 g_{t\alpha}^1\binom{1}{2} & -S_3 g_{t\beta}^1\binom{1}{1}+S_2 g_{t\beta}^1\binom{1}{2} \\ * & * & g_{\alpha\alpha}^3+C_1 g_{\alpha\alpha}^2\binom{1}{0}+C_2 g_{\alpha\alpha}^1\binom{2}{2} & S_2 g_{\alpha\beta}^1\binom{2}{2}+S_1 g_{\alpha\beta}^1\binom{2}{1} \\ * & * & * & g_{\beta\beta}^3+C_1 g_{\beta\beta}^2\binom{1}{0}+C_2 g_{\beta\beta}^1\binom{2}{2} \end{bmatrix}$$

E_1' mode

$$\begin{bmatrix} g_{ss}^2 & C_1 g_{st}^1 & g_{s\alpha}^1\binom{1}{1}+C_2 g_{s\alpha}^1\binom{1}{2} & S_2 g_{s\beta}^1\binom{1}{2} \\ * & g_{tt}^2+C_2 g_{tt}^1 & C_1 g_{t\alpha}^2+C_3 g_{t\alpha}^1\binom{1}{2} & -S_1 g_{t\beta}^1\binom{1}{1}+S_3 g_{t\beta}^1\binom{1}{2} \\ * & * & g_{\alpha\alpha}^3+C_2 g_{\alpha\alpha}^2\binom{1}{0}+C_3 g_{\alpha\alpha}^1\binom{2}{2} & -S_3 g_{\alpha\beta}^1\binom{2}{2}+S_2 g_{\alpha\beta}^1\binom{2}{1} \\ * & * & * & g_{\beta\beta}^3+C_2 g_{\beta\beta}^2\binom{1}{0}+C_3 g_{\beta\beta}^1\binom{2}{2} \end{bmatrix}$$

E_2' mode

$$\begin{bmatrix} g_{ss}^2 & -C_2 g_{st}^1 & g_{s\alpha}^1\binom{1}{1}+C_3 g_{s\alpha}^1\binom{1}{2} & S_3 g_{s\beta}^1\binom{1}{2} \\ * & g_{tt}^2+C_3 g_{tt}^1 & -C_2 g_{t\alpha}^2-C_1 g_{t\alpha}^1\binom{1}{2} & -S_2 g_{t\beta}^1\binom{1}{1}-S_1 g_{t\beta}^1\binom{1}{2} \\ * & * & g_{\alpha\alpha}^3+C_3 g_{\alpha\alpha}^2\binom{1}{0}+C_1 g_{\alpha\alpha}^1\binom{2}{2} & -S_1 g_{\alpha\beta}^1\binom{2}{2}+S_3 g_{\alpha\beta}^1\binom{2}{1} \\ * & * & * & g_{\beta\beta}^3+C_3 g_{\beta\beta}^2\binom{1}{0}+C_1 g_{\beta\beta}^1\binom{2}{2} \end{bmatrix}$$

E_3' mode

$C_1=2\cos(\frac{2\pi}{7})$ $S_1=2\sin(\frac{2\pi}{7})$

$C_2=2\cos(\frac{4\pi}{7})$ $S_2=2\sin(\frac{4\pi}{7})$

$C_3=2\cos(\frac{6\pi}{7})$ $S_3=2\sin(\frac{6\pi}{7})$

TABLE A7. G-matrices for 8-membered ring: B_{1g} and B_{2g} modes. Asterisks (*) indicate redundant matrix elements in the symmetric matrix.

$$\begin{bmatrix} g_{ss}^{2} & g_{s\alpha}^{1}\binom{1}{1}-2g_{s\alpha}^{1}\binom{1}{2} \\ * & g_{\alpha\alpha}^{3}-2g_{\alpha\alpha}^{2}\binom{1}{0}-2g_{\alpha\alpha}^{1}\binom{2}{2} \end{bmatrix}$$

B_{1g} mode

$$\begin{bmatrix} g_{tt}^{2}-2g_{tt}^{1} & 2\,[g_{t\beta}^{1}\binom{1}{1}+g_{t\beta}^{1}\binom{1}{2}] \\ * & g_{\beta\beta}^{3}-2g_{\beta\beta}^{2}\binom{1}{0}-2g_{\beta\beta}^{1}\binom{2}{2} \end{bmatrix}$$

B_{2g} mode

TABLE A8. G-matrices for 8-membered ring: E_{2g}, E_{1u}, and E_{3u} modes. Asterisks (*) indicate redundant matrix elements in the symmetric matrix.

$$\begin{bmatrix} g_{ss}^2 & \sqrt{2}g_{st}^1 & g_{s\alpha}^1\binom{1}{1} & 2g_{s\beta}^1\binom{1}{2} \\ * & g_{tt}^2 & \sqrt{2}\,[g_{t\alpha}^2 - g_{t\alpha}^1\binom{1}{2}] & \sqrt{2}\,[g_{t\beta}^1\binom{1}{2} - g_{t\beta}^1\binom{1}{1}] \\ * & * & g_{\alpha\alpha}^3 - 2g_{\alpha\alpha}^1\binom{2}{2} & 2g_{\alpha\beta}^1\binom{2}{1} \\ * & * & * & g_{\beta\beta}^3 - 2g_{\beta\beta}^1\binom{2}{2} \end{bmatrix}$$

E_{2g} mode

$$\begin{bmatrix} g_{ss}^2 & \sqrt{2+\sqrt{2}}\,g_{st}^1 & g_{s\alpha}^1\binom{1}{1} + \sqrt{2}g_{s\alpha}^1\binom{1}{2} & \sqrt{2}g_{s\beta}^1\binom{1}{2} \\ * & g_{tt}^2 + \sqrt{2}g_{tt}^1 & \sqrt{2+\sqrt{2}}\,g_{t\alpha}^2 + \sqrt{2-\sqrt{2}}\,g_{t\alpha}^1\binom{1}{2} & \sqrt{2+\sqrt{2}}\,g_{t\beta}^1\binom{1}{2} - \sqrt{2-\sqrt{2}}\,g_{t\beta}^1\binom{1}{1} \\ * & * & g_{\alpha\alpha}^3 + \sqrt{2}g_{\alpha\alpha}^2\binom{1}{0} & 2g_{\alpha\beta}^1\binom{2}{2} + \sqrt{2}g_{\alpha\beta}^1\binom{2}{1} \\ * & * & * & g_{\beta\beta}^3 + \sqrt{2}g_{\beta\beta}^2\binom{1}{0} \end{bmatrix}$$

E_{1u} mode

$$\begin{bmatrix} g_{ss}^2 & \sqrt{2-\sqrt{2}}\,g_{st}^1 & g_{s\alpha}^1\binom{1}{1} - \sqrt{2}g_{s\alpha}^1\binom{1}{2} & \sqrt{2}g_{s\beta}^1\binom{1}{2} \\ * & g_{tt}^2 - \sqrt{2}g_{tt}^1 & \sqrt{2-\sqrt{2}}\,g_{t\alpha}^2 - \sqrt{2+\sqrt{2}}\,g_{t\alpha}^1\binom{1}{2} & -\sqrt{2-\sqrt{2}}\,g_{t\beta}^1\binom{1}{2} - \sqrt{2+\sqrt{2}}\,g_{t\beta}^1\binom{1}{1} \\ * & * & g_{\alpha\alpha}^3 - \sqrt{2}g_{\alpha\alpha}^2\binom{1}{0} & -2g_{\alpha\beta}^1\binom{2}{2} + \sqrt{2}g_{\alpha\beta}^1\binom{2}{1} \\ * & * & * & g_{\beta\beta}^3 - \sqrt{2}g_{\beta\beta}^2\binom{1}{0} \end{bmatrix}$$

E_{3u} mode

TABLE A9. F-matrices for A_{1g}, B_{1g}, B_{2g}, and E-type modes, where f_c is the coupling force constant, f_b is the bond-stretching force constant, and f_a is the bond-angle-bending force constant.

$$\begin{bmatrix} f_c & 0 \\ 0 & f_b \end{bmatrix}$$

A_{1g} mode

$$\begin{bmatrix} f_c & 0 \\ 0 & f_a \end{bmatrix}$$

B_{1g} mode

$$\begin{bmatrix} f_b & 0 \\ 0 & f_a \end{bmatrix}$$

B_{2g} mode

$$\begin{bmatrix} f_c & 0 & 0 & 0 \\ 0 & f_b & 0 & 0 \\ 0 & 0 & f_a & 0 \\ 0 & 0 & 0 & f_a \end{bmatrix}$$

E-type modes

APPENDIX B

RING MOTIONS FOR SELECTED VIBRATIONAL SPECIES

Presented are ring motions for selected vibrational species of the 4-, 5-, 6-, 7-, and 8-membered rings. In most cases, two or more different sets of ring motion are possible for an E-type vibrational mode. This appendix is not intended to be an exhaustive reference on ring motions, but to provide illustrative examples of possible ring motions for some vibrational species of each ring. Therefore, some of the E-type ring motions have been excluded. The reader should note the similarity between ring motions for different-sized rings, particularly the A_{1g} and A_1' breathing modes, and the E_{2g} and E_2' ring stretching modes.

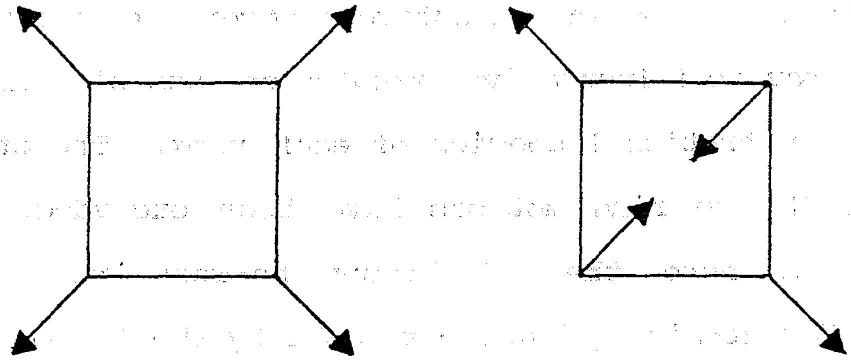

A_{1g} mode

B_{1g} mode

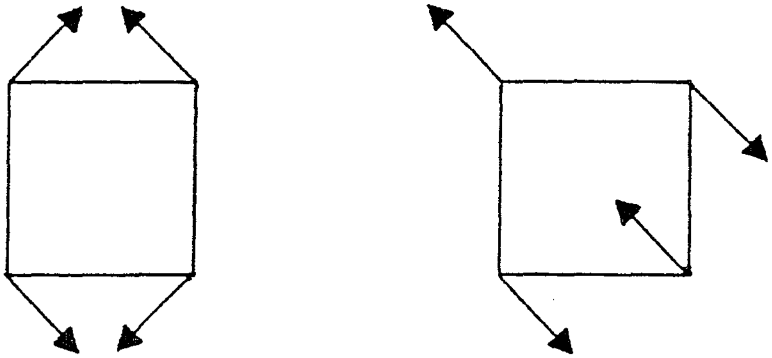

B_{2g} mode

E_{1u} mode

FIG. B1. Modes of oscillation for the 4-membered ring.

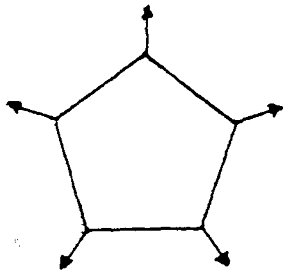

A_1' mode

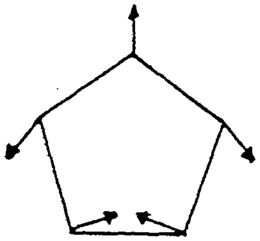

E_1' mode

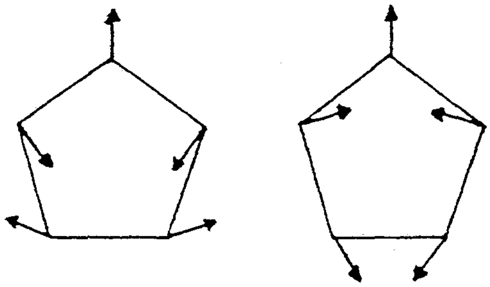

E_2' mode

FIG. B2. Modes of oscillation for the 5-membered ring.

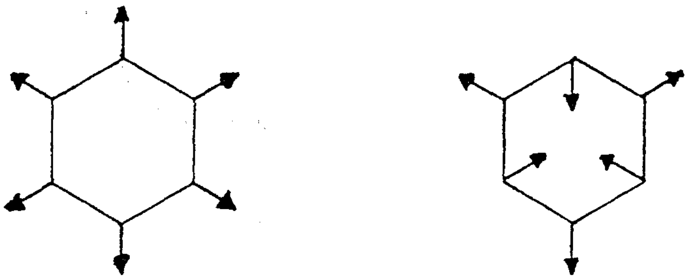

A_{1g} mode

B_{1u} mode

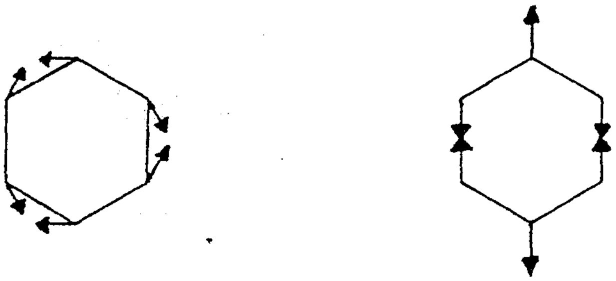

B_{2u} mode

E_{2g} mode

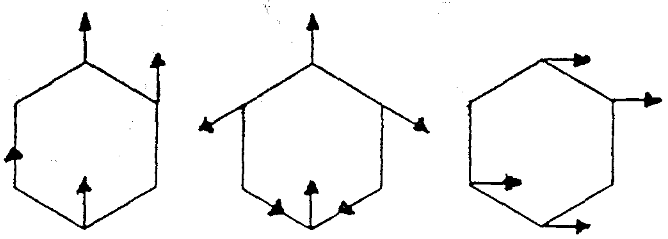

E_{1u} mode

FIG. B3. Modes of oscillation for the 6-membered ring.

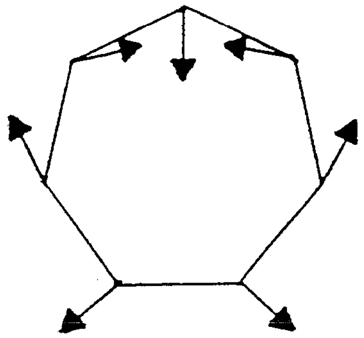

E_1' mode

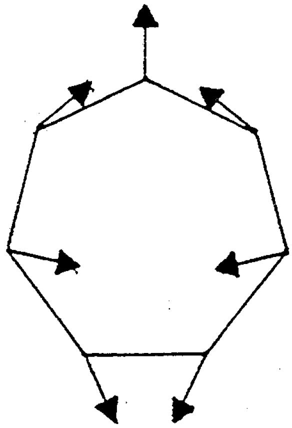

E_2' mode

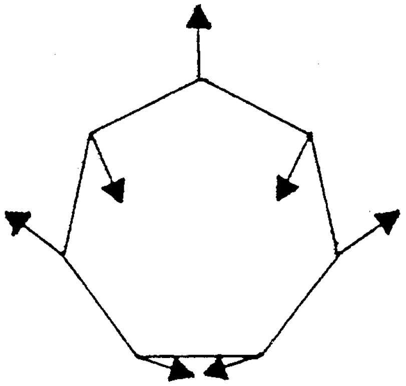

E_3' mode

FIG. B4. Modes of oscillation for the 7-membered ring.

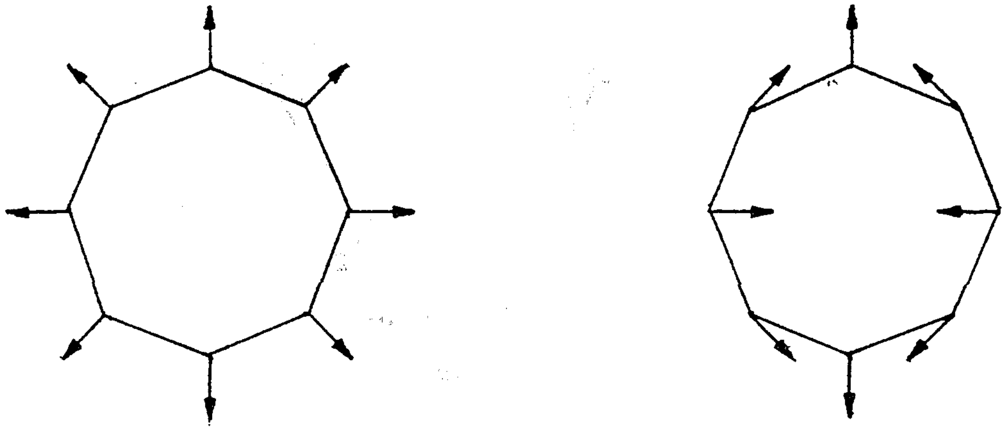

A_{1g} mode

E_{2g} mode

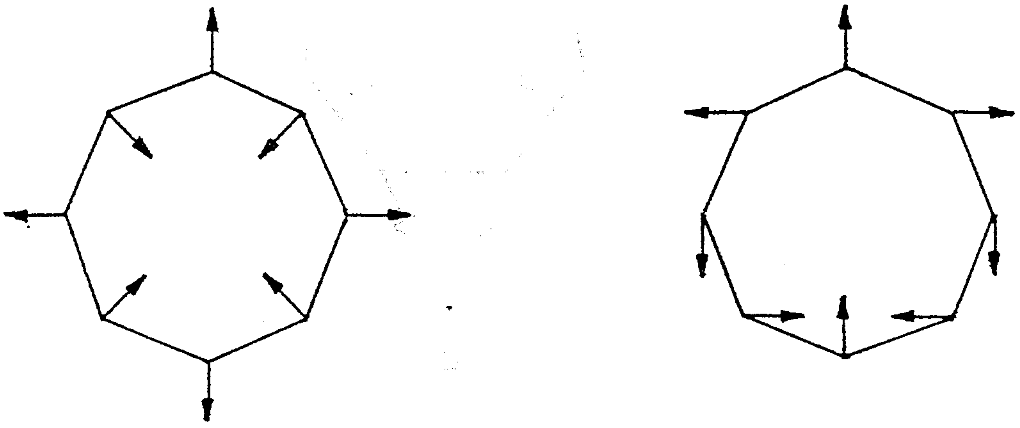

B_{1g} mode

E_{1u} mode

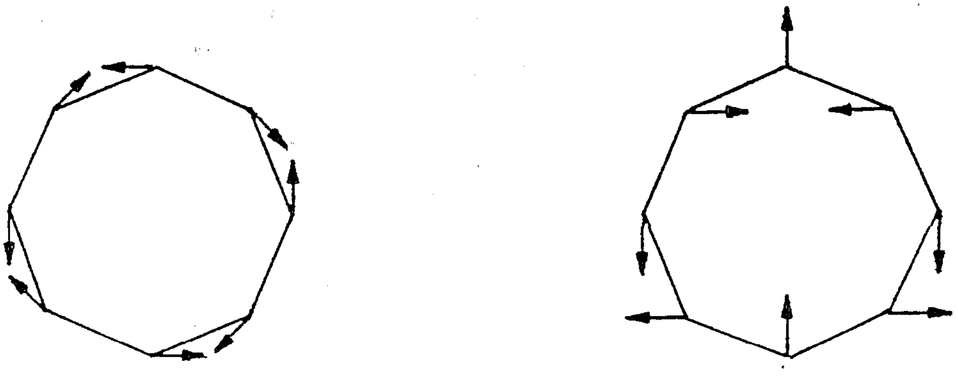

B_{2g} mode

E_{3u} mode

FIG. B5. Modes of oscillation for the 8-membered ring.